Phase Matched Coupling for Ladar Systems Incorporating Single Mode Optical Fiber Receivers

Thesis

Submitted To

Graduate Engineering & Research

School of Engineering

UNIVERSITY OF DAYTON

In Partial Fulfillment of the Requirements for

The Degree

Master of Science in Electro-Optics

by

Christopher David Brewer

UNIVERSITY OF DAYTON

Dayton, Ohio

December 1997

UNIVERSITY OF DAYTON ROESCH LIBRARY

Phase Matched Coupling for Ladar Systems Incorporating Single Mode Optical Fiber Receivers

APPROVED BY:

Bradley D. Duncan, Ph.D.
Associate Professor of Electro-Optics
Committee Chairman

Edward A. Watson, Ph.D.
Chief Engineer Electro-Optics Branch
Wright Laboratory, Wright-Patterson AFB
Committee Member

Kenneth J. Barnard, Ph.D.
Research Scientist
University of Dayton,
Center for Electro-Optics
Committee Member

Donald T. Miller, Ph.D.
NRC Research Associate
Wright Laboratory, Wright-Patterson AFB
Committee Member

Donald L. Moon, Ph.D.
Associate Dean
Graduate Engineering Programs
and Research
School of Engineering

Blake Cherrington, Ph.D., P.E.
Dean, School of Engineering

ABSTRACT

Phase Matched Coupling for Ladar Systems Incorporating Single Mode Optical Fiber Receivers

Name: Brewer, Christopher David
University of Dayton

Advisor: Dr. Bradley D. Duncan

A rigorous method for modeling received power coupling efficiency ($\eta_{F/R}$) and transmitted power coupling efficiency ($\eta_{F/T}$) in a general target illumination Ladar system is presented. For our analysis, we concentrate on incorporating a single-mode optical fiber into the ladar return signal path. By developing expressions for both $\eta_{F/R}$ and $\eta_{F/T}$ for a simple, diffuse target, our model allows for varying range, beam size on target, target diameter, and coupling optics. Through numerical analysis, $\eta_{F/R}$ is shown to increase as the range to target increases and decrease as target diameter increases, while $\eta_{F/T}$ is shown to decrease with target range. A baseline signal-to-noise ratio analysis of the system is also provided for varying illumination schemes. Techniques for implementing a phase only matched filter at the receiver of a flood-illumination LADAR system incorporating single mode optical fiber receiver is then examined theoretically for various types of glint and diffuse targets. Experimental methods for using liquid crystal spatial light modulator technology to increase the coupling of spatially complex target returns are also presented.

ACKNOWEDGEMENTS

I would like to first of all thank my mom and dad for all of their support over the past few months. They constantly forced me to keep my eye on the bigger picture when I got frustrated with little things and were always there when I just needed to get away from Dayton for a while. I would also like to thank my advisor Dr. Bradley Duncan for all of his time and effort in guiding and editing this work. I'm sure he put in as much time as I did getting the finished product ready. Thanks also to Dr. Edward Watson, Dr. Kenneth Barnard, and Dr. Donald Miller for answering all of my "Do you have a minute?" questions even when they didn't. I truly appreciate it. Thanks again to Larry Barnes and Mike Salisbury for helping me find all of the equipment I needed that was squirreled away in the lab somewhere. Finally, I would like to thank the Wright Laboratory Electro-Optic Sensor Group, Technology/Scientific Services Inc., Dayton Ohio, and the University of Dayton Center for Electro-Optics for providing research facilities, funding, and opportunity for this work.

TABLE OF CONTENTS

APPROVAL PAGE....ii

ABSTRACT....iii

ACKNOWLEDGMENTS....iv

TABLE OF CONTENTS....v

LIST OF FIGURES....viii

LIST OF TABLES....xi

CHAPTER

I. INTRODUCTION....1

II. GEOMETRIC COUPLING EFFICIENCY ANALYSIS FOR DIRECT DETECTION LADAR SYSTEMS INCORPORATING SINGLE MODE AND MULTIMODE OPTICAL FIBER RECEIVERS....7

2.1 Geometric Coupling Model....8

2.1.1 Multimode Fiber Receivers....9

2.1.2 Single Mode Fiber Receivers....11

2.2 General Illumination Terminology....17

III. BASELINE COUPLING EFFICIENCY ANALYSIS FOR A DIRECT DETECTION LADAR SYSTEM INCORPORATING A SINGLE MODE OPTICAL FIBER....20

3.1 Field at the Fiber Endface....20

3.2 Single Mode Fiber F/R Coupling Efficiency....25

3.3 Comparison with Geometric Model....32

IV. SYSTEM EFFICIENCY ANALYSIS....41

4.1 Transmitted Power Coupling Efficiency....41

4.2 Signal to Noise Ratio Analysis....44

V. GLINT TARGET COUPLING ANALYSIS....48

5.1 Field Analysis for a Glint Target....48

VI. COUPLING EFFICIENCY ENHANCEMENT WITH PHASE ONLY FILTERING FOR SINGLEMODE GLINT AND DIFFUSE TARGETS....63

6.1 Gerchberg-Saxton Algorithm....65

6.2 Glint Target Coupling Efficiency Enhancement Analysis....68

6.3 Diffuse Target Coupling Efficiency Enhancement Analysis....77

VII. THEORETICAL AND EXPERIMENTAL ANALYSIS OF PHASE ONLY FILTERING MULTIMODE RETURNS FROM UNRESOLVED TARGETS....82

7.1 Imaging a Rectangular Target....83

7.2 Fraunhofer Diffraction from a Slit Target....85

7.3 1-D Beam Shaping Simulations....89

7.4 Experimental Phase Only Filtering of Multimode Returns....96

7.5 Further Observations....100

7.6 Ronchi Ruling Experiment....105

VII. CONCLUSIONS AND RECOMMENDATIONS....109

APPENDIX

A. F/R COUPLING EFFICIENCY FOR AN UNRESOLVED, GLINT TARGET WITH A MULTIMODERETURN....113

A.1 Coupled Signal Power....113

A.2 Total Received Power....115

B. F/R COUPLING EFFICIENCY FOR A RESOLVED, DIFFUSE TARGET WITH A SINGLEMODE RETURN....118

B.1 Field at the Fiber....118

B.2 Coupling Efficiency....120

C. *MATLAB* COMPUTER SIMULATIONS....127

C.1 Field Scaling....127

C.2 *Matlab* Simulation Routines....128

REFERENCES....135

LIST OF FIGURES

Figure 2.1: Imaging Lens System used for the geometric analysis.....8

Figure 2.2: Fiber diameter vs. target range for a direct detection ladar system incorporating a multimode fiber receiver.....10

Figure 2.3: Geometric received power coupling efficiency ($\eta_{F/R}$) vs. target range.....15

Figure 2.4: Target illumination/return illustrations for a.) unresolved target, multimode return, b.) unresolved target, singlemode return, c.) resolved target, multimode return, d.) resolved target, singlemode return.....17

Figure 3.1: General Illumination LADAR system demonstrating a multimode return from a unresolved target. In an actual LADAR system, the TX and RX would be colinearly aligned.....21

Figure 3.2: Circ function overlap.....29

Figure 3.3: Illustration of the geometry used for calculating the focal length for the negative lens l_2.....35

Figure 3.4: Received power coupling efficiency ($\eta_{F/R}$) vs. target range for a target diameter of 0.3 m.....37

Figure 3.5: Receiver to fiber power coupling efficiency $\eta_{F/R}$ for a flood illuminated target vs. the illuminated target diameter at a constant range of 20 km.....38

Figure 3.6: F/R coupling efficiency vs illuminated spot size on a 1 m target at a constant range of 20 km.....39

Figure 4.1: Transmitted power coupling efficiency ($\eta_{F/T}$) vs. target range for a resolved target with a nearly singlemode return.....44

Figure 4.2: SNR vs. target range for a resolved target with a nearly singlemode return....45

Figure 4.3: Signal-to-noise ratio (SNR) vs. target range for a multimode return, large resolved target. The beam diameter in the target plane has been set to 15 m....45

Figure 5.1: LP_{11} modal field in an optical fiber....59

Figure 5.2: Receiver/fiber coupling efficiency vs. the "a" parameter for a diffuse and a glint target in the near field, as well as a glint target in the far field. Each target is resolved and has a singlemode return. Range to the diffuse and glint targets in the near field is 20 km....61

Figure 6.1: Modified laser radar system with a liquid crystal spatial modulator (LCSLM) in the receiver....65

Figure 6.2: Flowchart depicting the steps involved in the Gerchberg-Saxton algorithm....66

Figure 6.3: Flowchart depicting the steps involved in calculating the F/R coupling efficiency via the *Matlab* computer simulations....69

Figure 6.4: Gerchberg-Saxton phasemask across the liquid crystal spatial light modulator for a resolved, glint target with a singlemode return....72

Figure 6.4: Discrete sampling example for the LP_{01} mode of the fiber as used in the computer simulations....75

Figure 6.5: Flowchart depicting the steps involved in calculating the F/R coupling efficiency for a diffuse target via the *Matlab* computer simulations....79

Figure 6.6: F/R coupling efficiency for a resolved, diffuse target with a singlemode return a.) without and b.) with the glint target phase mask across the liquid crystal device....80

Figure 7.1: Normalized, 1-D Fresnel field from a 20 m unresolved target with multimode return at the receiver aperture....84

Figure 7.2: Modified general illumination ladar receiver with an imaging and Fourier transform lens before the LCSLM....85

Figure 7.3: Imaged spot size vs. true target diameter.....87

Figure 7.4: Sinc pattern across the LCSLM.....88

Figure 7.5: Transform lens focal length f_4 required to produce a seven lobe pattern on SLM vs. true target diameter at 20 km.....75

Figure 7.6: Ideal phasemask for increasing the F/R coupling efficiency from a 150 mm rectangular, target image that has been Fourier transformed onto the LCSLM with a 750 mm lens.....91

Figure 7.7: Factor increase in coupling vs. target diameter resulting from phase only filtering the return from a glint target.....92

Figure 7.8: Experimental setup.....95

Figure 7.9: Experimental beam profiles in the plane of the fiber with and without the phasemask present.....99

Figure 7.10: Theoretical beam profiles in the plane of the fiber a.) without and b.) with the phasemask present.....99

Figure 7.11: Power coupled vs. back focal length of l_3 for a 150 μm slit.....101

Figure 7.12: Factor increase in coupling vs. back focal length of l_3.....101

Figure 7.13: Power coupled vs. varying front focal length with and without the phasemask across the device for a 150 μm slit.....103

Figure 7.14: Factor increase in coupling vs. front focal length of l_4.....103

Figure 7.15: Factor increase in coupling vs. target diameter resulting from 1-D phase only filtering the return from a diffuse target.....104

Figure 7.16: Ronchi ruling target.....106

Figure 7.17: Phasemask for Ronchi ruling target.....107

Figure B.1: F/R coupling efficiency vs. the "a" parameter for a resolved, circular target at 20 km with singlemode return.....126

LIST OF TABLES

Table 6.1: Glint target F/R coupling efficiency values from the numerical integration and *Matlab* computer simulations for a singlemode target.....73

Table 6.2: Diffuse target F/R coupling efficiency values from the numerical integration and *Matlab* computer simulations.....81

Table 7.1: Theoretical and experimental results for factor increase in coupling for a.) 100 mm slit, b.) 150 mm slit and c.) 200 mm slit.....97

Table 7.2: Theoretical and experimental results for factor increase in coupling for the Ronchi ruling target.....108

CHAPTER I

Introduction

For most LADAR (LAser Detection And Ranging, a.k.a. "Laser Radar"), applications, a primary goal is to collect and focus onto a photodetector as much light as possible reflected from a distant target. Therefore, all other things being equal, one will rightly conclude that by simply increasing the detector area, the chances of increasing the *average* return signal from a target are improved. However, simply increasing the average, or DC, return signal is often not the primary issue that must be addressed when designing a ladar system. For example, besides the ability to simply detecting and ranging targets, some state-of-the-art ladar systems are also designed to achieve a high resolution capability for target depth profiling. Recalling that light travels approximately one foot per nanosecond in air, to achieve a target resolution of something less than a meter, the response time of photodetectors used in high range resolution ladar systems must be on the order of a Gigahertz. This response time limitation can only be met currently by detectors whose diameters are on the order of tens of few microns.

Unfortunately, using a small area detector makes alignment rather difficult, and greatly diminishes the percentage of collected optical return energy that can be converted into a useful electrical signal. Our goal here, then, is to examine the issues of received power coupling efficiency (i.e., the percentage of *received* optical energy available for detection) and transmitted power coupling efficiency (i.e., the percentage of *transmitted* optical energy available for detection) when small area receivers are used. By examining these issues, we will in the process see which system parameters can be adjusted for optimum system performance and we will establish, for a few specific cases, baseline values for both coupling efficiencies.

We will specifically look at the case of coupling diffuse returns into single mode optical fiber receivers. We do this for two primary reasons. First, diffuse target statistics are well known and will provide "worse case" results. Second, very often high speed detectors are provided with single mode fiber pigtails. These pigtails in turn provide their own advantages, among them being the ease of incorporating in-line fiber optic amplifiers into the optical signal path. In certain applications this optical pre-amplification step provides clear advantages.[1] In addition, though we do not specifically address this issue herein, the use of single mode fiber mixers in heterodyne ladar systems (e.g., when target velocity measurements are required) provides for an efficient overall ladar system which is highly robust with respect to its internal optical alignment.[2] We also point out that by considering the coupling of ladar returns into single mode optical fibers we are also, in a manner of speaking, looking at the worst case coupling scenario. For example, to effectively couple light into a single mode optical fiber requires that the received light enter the fiber through its numerical aperture (NA) and be spatially matched to the LP_{01}

mode. However, coupling to a small area detector only requires matching the detector area to the focal spot size of the ladar receiving optics.

With low signal power returns, any improvement in detector coupling efficiency will enhance the performance of the ladar system. One simple method of optimizing the received power coupling efficiency $\eta_{F/R}$ has been shown by our colleagues Jacob *et al.*[2] They examined $\eta_{F/R}$ for the special case of a purely diffuse, *small-spot illuminated target*, positioned in the *far field* of a ladar system incorporating a single mode optical fiber (SMOF) receiver. It was shown that by correctly matching the numerical aperture (NA) of the receiver optics to that of the optical fiber, the signal power coupled from the target into the LP_{01} mode of optical fiber can be maximized.

It was also shown that this type of coupling is dependent on the size of the Gaussian beam transmitted by the source. Defining the transmit truncation ratio R as the ratio of the transmitter exit aperture diameter D_{trans} to the transmitted beam waist ω_o [i.e., $R=D_{trans}/\omega_o$], it was shown that for truncation ratios greater than the optimum ratio of four, the amount of light coupled into the fiber receiver drops dramatically due to increased beam divergence upon transmission. Furthermore, if the truncation ratio is less than four, the beam is apodized at the transmitter exit aperture. This induces a significant loss of energy upon transmission, as well as diffraction effects, which can not be ignored and which ultimately reduces both the received and transmitted power coupling efficiencies, $\eta_{F/R}$ and $\eta_{F/T}$. By NA matching the receiver coupling optics *and* by setting the truncation ratio to its optimum value of R=4, it was shown that one can expect to achieve a received power coupling efficiency of approximately $\eta_{F/R}$= 31% for a ladar system operating at a wavelength of 1 μm.

The model developed by Jacob *et al.* further assumed that the beam on target was much smaller than the target itself. Spot illuminating a target, however, requires that the ladar beam must be scanned across an object if full target data is to be collected. Unfortunately, this type of collection scheme is inherently slow and requires a fair amount of data processing. On the other hand, flood illumination of a target allows one to, in effect, rapidly take a single "snapshot" of the object while gathering a great deal of information about the whole target. Such 1-D interrogation schemes are currently under investigation for use in RF radar applications.[3] However, expanding the area of the transmitted beam decreases the energy density in the target plane. For smaller targets with a diameter of a meter or less, fewer photons will be reflected overall and both $\eta_{F/R}$ and $\eta_{F/T}$ will drop dramatically.

Counteracting this declining trend in coupling efficiency can be accomplished somewhat simply by altering the magnitude and phase of the collected beam profile at the fiber endface. If the modal field of the collected light passed through the receiver aperture resembles the LP_{01} mode more closely, the signal power coupled into the fiber will be greater, thereby increasing both the $\eta_{F/R}$ and the $\eta_{F/T}$ coupling efficiencies. Simple beam shaping abilities have already been demonstrated by Lee.[4] He has shown that it is possible to convert a typical, Gaussian beam profile into a more uniform distribution by phase filtering the incoming beam with a computer generated hologram (CGH). Applying this technique to a direct detection ladar system, we will proceed to investigate the effects of inserting a liquid crystal spatial light modulator or LCSLM into the path of the ladar receiver. This device is similar to the CGH but allows one to compensate for the inherent phase profile of the particular target as well as the phase

accumulated upon propagation from the target to the receiver in real time. We shall see that once this target specific phase profile is known, it can altered through phase-only filtering the collected return, enhancing both $\eta_{F/R}$ and $\eta_{F/T}$.

With this goal in mind, the coupling efficiency enhancement development within the text is as follows. For comparison, a simple geometric model of $\eta_{F/R}$ for ladar systems incorporating multimode and singlemode fiber receivers will first be presented in Chapter II as well as a set of definitions describing the nature of a target and its return in a general-illumination system. These working definitions will then be incorporated into expressions for the received field at the fiber endface and received power coupling efficiency $\eta_{F/R}$ in Chapter III. The development of this general illumination model will then follow along the same general lines as Jacob's development,[2] but will allow for varying transmission and receiver optics, target range, beam size in the target plane, and target diameter. However, as with Jacob's original analysis, this development will not account for the effects of atmospheric turbulence. Next, in Chapter IV, the transmitted power coupling efficiency and a baseline signal-to-noise ratio SNR analysis will be presented.

In Chapter V, we develop a theoretical model and calculate the F/R coupling efficiency for a glint target. This will then be the baseline of comparison for the coupling efficiency enhancement simulations found in Chapter VI for resolved, glint and diffuse targets with singlemode returns. We then turn our attention to improving the coupling efficiency of returns from larger, multimode targets within the context of a general illumination ladar system. Chapter VII presents a set of computer simulated and experimental results for improving the F/R coupling of multimode returns from various

unresolved glint targets. Finally, Chapter VIII contains a summary and proposals for future work in this area.

CHAPTER II

Geometric Coupling Efficiency Analysis for Direct Detection Ladar Systems Incorporating Multimode and Single Mode Optical Fiber Receivers

In general, a ladar receiver includes the detector and its associated coupling optics. Beam expansion optics are also typically included in this group since they merely increase the solid angle of the target, as seen by the detector. With this configuration in mind, a geometric model for received power coupling efficiency will first be developed for a simple, one lens imaging system equipped with a beam expanding telescope. This geometric analysis is primarily presented to serve as a basis of comparison for the more complete model we will develop later in Chapter III. Unfortunately, because it is simple enough to do, this geometric coupling analysis is often performed in lieu of the more rigorous approach. Though we will see that under some circumstances the geometric and the following rigorous analyses of Chapter III agree very well (they should not, of course, be fully inconsistent with one another), the limitations of the geometric approach for both single mode and multimode fiber receivers will become very apparent.

2.1 Geometric Coupling Model

The system we will be focusing on for the geometric analysis is illustrated in Figure 2.1 below,

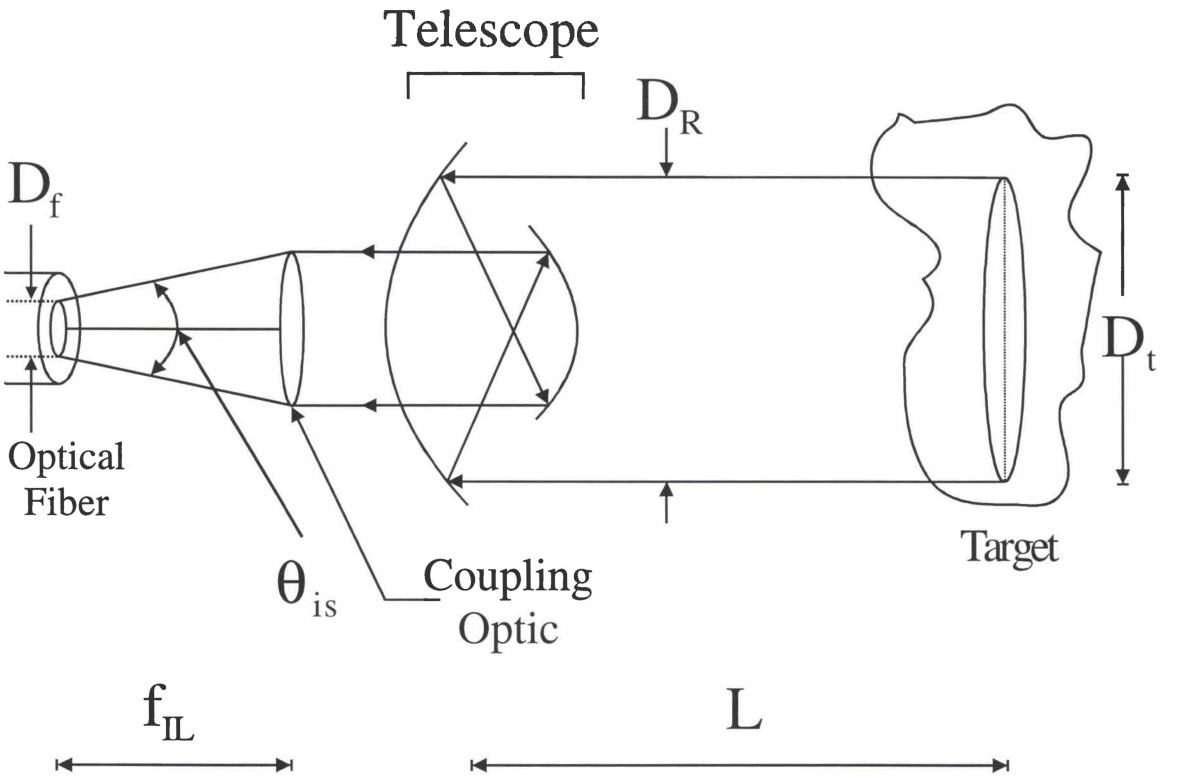

Figure 2.1: Imaging Lens System used for the geometric analysis.

where L is the distance from the receiver to the target, f_{IL} is the focal length of the imaging lens, and θ_{is} is the full field image space angle of the fiber. Furthermore, D_t is the target diameter, D_R is the receiver diameter, and D_f is the diameter of the fiber core. Note, here we have assumed that the fiber lies in the focal plane of the coupling optic in order to obtain the maximum coupling from targets at extended ranges.

2.1.1 Multimode Fiber Receivers

By far the easiest method of maximizing the coupling efficiency in ladar systems that incorporate optical fiber receivers is to increase the area of the fiber. As long as the area of the imaged spot is smaller than the diameter of the optical fiber core, a coupling efficiency of 100% can theoretically be obtained. Thus, multimode fiber receivers are ideally suited for the task of optimizing coupling. To determine the area of the target image in the plane of the fiber, a *uniformly illuminated*, diffuse target is assumed to be a large distance L away from the receiver aperture as shown in Figure 2.1. The full field angle of the illuminated portion of the target θ_{os} , as seen by the telescope, is then given for small angles by

$$\theta_{os} = \frac{D_t}{L} \quad , \tag{2-1}$$

where D_t is the illumination spot diameter in object space. To transform this angle to the full field image space angle θ_{is} of the fiber, θ_{os} is multiplied by the magnification M of the beam expanding telescope, yielding the following expression,

$$\theta_{is} = \frac{MD_t}{L} \quad . \tag{2-2}$$

Multiplying by the focal length of the imaging lens f_{IL}, the area of the imaged target A_t' at the fiber becomes,

$$\begin{aligned} A_t' &= \pi\left(\frac{\theta_{is} \times f_{IL}}{2}\right)^2 \\ &= \pi\left(\frac{MD_t f_{IL}}{2L}\right)^2 \\ &= \pi r_{eff}^2 \end{aligned} \quad , \tag{2-3}$$

where r_{eff} is the radius of the target image at the fiber endface.

If we now equate the area of the imaged target to the area of the multimode fiber $A_{f,mm}$, we find

$$\begin{aligned} A_{f,mm} &= A_t' \\ \frac{\pi D_{f,mm}^2}{4} &= \pi\left(\frac{MD_t f_{IL}}{2L}\right)^2 \\ D_{f,mm} &= \frac{MD_t f_{IL}}{L} \end{aligned} \quad , \qquad (2\text{-}4)$$

where $D_{f,mm}$ is the diameter of the multimode fiber. We can now determine the range at which 100% coupling is achieved for a given target size. For this analysis, we will assume a focal length, for reasons that will become apparent shortly, of f_{IL} = 3.85 cm for the coupling optic and a telescope magnification of 10X. With these values, a plot of fiber diameter vs. target range for several different target diameters can be generated. This family of curves is shown in Figure 2.2.

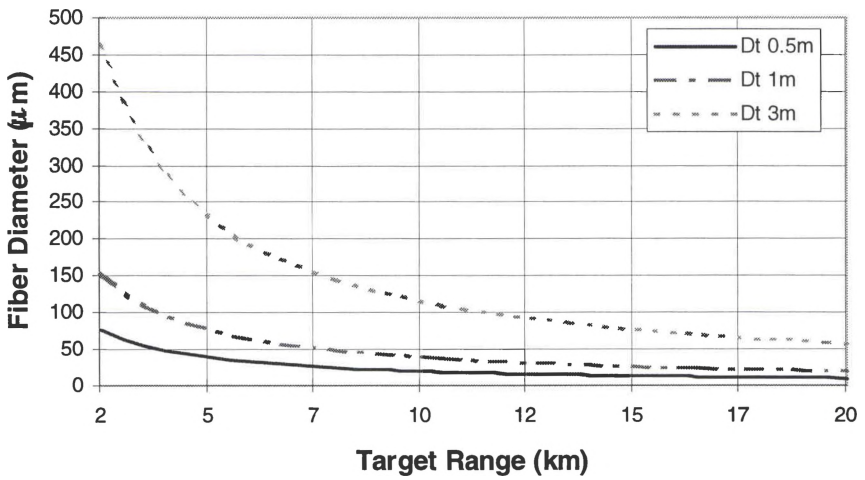

Figure 2.2: Fiber diameter vs. target range for 100% coupling efficiency in a direct detection ladar system incorporating a multimode fiber receiver.

From Figure 2.2, for a typical multimode fiber diameter of $D_{f,mm} = 100$ μm, we see that as the target diameter increases the range at which the maximum coupling occurs also increases. Furthermore, if the range to the target is kept constant, one must increase the size of the multimode fiber receiver in order to maintain a particular coupling efficiency when the target size increases. Unfortunately, simply increasing the area of the fiber to increase the coupling does not come without certain tradeoffs.

Increasing the coupling efficiency is not always the primary issue that must be addressed when designing a ladar system. As stated in Chapter I, to achieve a high range resolution for depth profiling, the response time of photodetectors used to amplify the detected signal must be on the order of a Gigahertz; which can only be met currently by detectors whose diameters are on the order of a tens of microns. Therefore, at the interface between multimode fiber/post-detection amplifier, a significant amount of collected light could be lost if the area of the fiber is much bigger than that of the smaller detector. This problem can be overcome by replacing the multimode fiber receiver with a single mode fiber receiver. So long as the received signal coupled into the fiber is above the inherent noise of the system, it can be amplified to useful levels. Thus, even though moving to a smaller diameter fiber would decrease the coupling efficiency for larger targets, it may increase the transverse resolution of the ladar system and give the operator the ability to distinguish between various types of targets. The next section will examine the geometric coupling efficiency for a single mode fiber receiver.

2.1.2 Single Mode Fiber Receivers

The received power coupling efficiency in a direct detection ladar system incorporating a single mode optical fiber receiver can be determined by taking the ratio of

the power coupled into the LP_{01} mode of the receiving fiber to that of the power $\tilde{P}_R$ in the target image at the fiber endface. For a circular target, the total received power $\tilde{P}_R$ is then the irradiance of the uniform image field $\tilde{\mathbf{U}}_f$ at the fiber endface multiplied by the area of the target image A_t'. That is,

$$\begin{aligned}\tilde{P}_R &= \iint_{A_t'} d\bar{\rho}_f \left|\tilde{\mathbf{U}}_f(\bar{\rho}_f)\right|^2 \\ &= \left|\tilde{\mathbf{U}}_f\right|^2 \times \pi\left(\frac{MD_t f_{II}}{2L}\right)^2\end{aligned} \quad , \tag{2-5}$$

where $\bar{\rho}_f$ is the spatial variable associated with the fiber plane and the remaining variables are defined as for Figure 2.1. For notational purposes throughout this thesis, a boldface quantity will represent a complex field, an overscore will denote a vector quantity, and a tilde will indicate a random field.

When the diameter of the focused spot on the fiber endface is larger than the fiber core, the power $\tilde{P}_{sig}$ coupled into the fundamental mode of the receiving fiber can then be approximated by an overlap integral between the field $\tilde{\mathbf{U}}_f(\bar{\rho}_f)$ and the complex conjugate of the LP_{01} modal field, $\mathbf{U}_{01}^*(\bar{\rho}_f)$.[5] This relationship is given by,

$$\tilde{P}_{sig} \approx \left|\iint d\bar{\rho}_f \, \tilde{\mathbf{U}}_f(\bar{\rho}_f)\, \mathbf{U}_{01}^*(\bar{\rho}_f)\right|^2 \quad . \tag{2-6}$$

However, assuming that the field variations over the area of the imaged spot due to the random nature of the diffuse target are small, $\tilde{\mathbf{U}}_f(\bar{\rho}_f)$ can be treated as a constant and pulled out of the double integral, provided the imaged target spot is larger than the fiber core. We make this assumption here because the field focused on the endface of the fiber can be shown to be spatially correlated near the fiber core.[6] This in essence arises in a

way similar to the one by which the correlation of a time domain signal increases by narrow-band filtering.[7] In our case, the signal of interest is the random backscatter from the diffuse target and our *spatial*, narrow-band low-pass filtering is performed by the finite NA of the receiver optics. Once the spot size becomes smaller than the area of the fiber core though, the overlap integral above is no longer valid. However, at this point we will be coupling 100% of the energy into the fiber, according to *this* model, and thus it is no longer necessary to calculate Eq. (2-6).

Continuing with the analysis of $\tilde{P}_{sig}$, for a singlemode fiber field, Marcuse[8] has shown that the LP_{01} field distribution, normalized to unit power, can be approximated as a Gaussian function defined as

$$\mathbf{U}_{01}\left(\overline{\rho}_f\right) \equiv \sqrt{\frac{2}{\pi\omega^2}} \exp\left(-\frac{\left|\overline{\rho}_f\right|^2}{\omega^2}\right) \quad , \tag{2-7}$$

where the approximate field distribution can be optimized if the ω parameter in Eq. (2-7) is found from the relationship[8]

$$\omega \equiv r_c\left(0.65 + \frac{1.619}{V^{3/2}} + \frac{2.879}{V^6}\right) \quad , \tag{2-8}$$

where r_c is the radius of the fiber core and V is the normalized frequency of the fiber given by[9]

$$V = \frac{2\pi r_c}{\lambda} NA \quad . \tag{2-9}$$

This approximation has been shown to have an accuracy of better than 1% in the region of $0.8 \le \lambda/\lambda_c \le 2$, where λ is the operating wavelength and λ_c is the cutoff wavelength of the LP_{11} mode.[8] Expressing the relationship in terms of the V number we find that the

approximation is valid so long as V falls in the range $1.2 \leq V \leq 3.0$. For this analysis, we will assume the use of Corning SMF-28 fiber which has a numerical aperture, NA, of approximately 0.13 at a wavelength of $\lambda = 1.5$ μm and has a core diameter of 8.3 μm. We then find the V number of the fiber at this wavelength to be V=2.26, thus validating the Gaussian approximation for the modal shape. With this established, substituting Eq. (2-7) back into Eq. (2-6) and assuming, from a geometric perspective, that the amount of guided energy coupled into the fiber cladding is negligible, we find that after integrating over the fiber core,

$$\tilde{P}_{sig} = \left|\tilde{U}_f\right|^2 \times 2\pi\omega^2 \left(1 - \exp\left(-\frac{r_c^2}{\omega^2}\right)\right)^2 \qquad (2\text{-}10)$$

Dividing Eq. (2-10) by Eq. (2-5), we obtain the following approximate expression for received power coupling efficiency $\eta_{F/R}$ in terms of target diameter, range, telescope magnification, focal length of the coupling optic, and fiber radius,

$$\eta_{F/R} = \frac{8(L\omega)^2}{\left(MD_t f_{IL}\right)^2}\left(1 - \exp\left(-\frac{r_c^2}{\omega^2}\right)\right)^2 \qquad (2\text{-}11)$$

Following along the lines of Jacob's previous work,[2] we will now calculate, for purposes of illustration, the maximum $\eta_{F/R}$ which occurs when the overall NA of the receiver optics matches that of the single mode fiber. This condition can also be related to the overall receiver f/# of the final coupling optic by,

$$f/\# = \frac{1}{2 \times NA} = \frac{M f_{IL}}{D_R} \qquad (2\text{-}12)$$

where D_R is the receiver diameter [i.e., the telescope entrance pupil diameter]. Assuming a telescope diameter of 10 cm and a telescope magnification of 10X, the focal length of

the coupling optic is readily found to be f_{IL} = 3.85 cm. Then assuming a uniformly illuminated target diameter of 0.3 m, a plot of $\eta_{F/R}$ vs. range L can be generated, as is shown in Figure 2.3. (Note the singlemode/multimode return boundary line appearing at 8.2 km. The significance of this boundary will be explained in greater detail in Section 2.2)

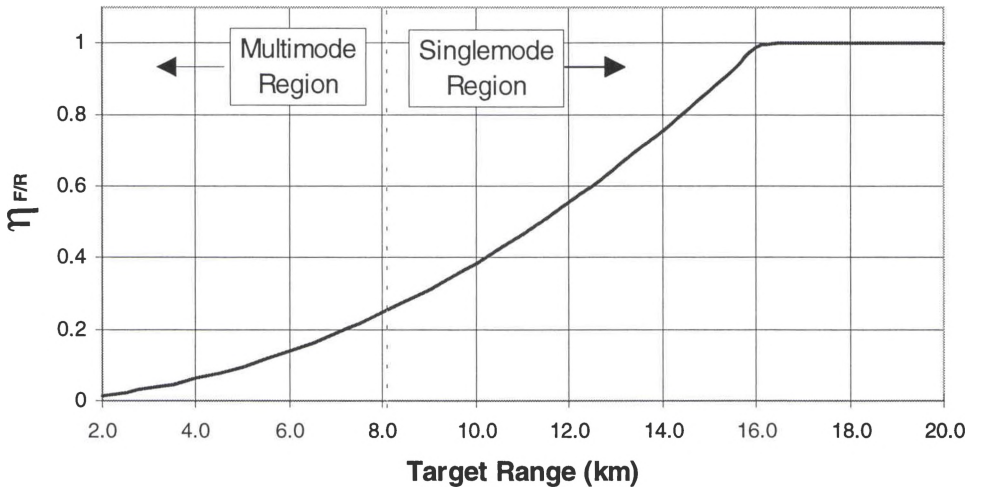

Figure 2.3: Geometric received power coupling efficiency ($\eta_{F/R}$) vs. target range.

Though we will see that this analysis is quite good at close ranges, the geometrical analysis admittedly does not fully stand up under scrutiny. Upon inspection of Figure 2.3, we see that when the target range increases beyond 16.2 km, coupling efficiency reaches 100%. However, once the target range exceeds 16.2 km, the geometric model mathematically allows the possibility of F/R coupling efficiencies greater than 100%. This is clearly impossible! Specifically, employing the Cauchy-Schwarz inequality one can show that,

$$\tilde{P}_{sig} \approx \left| \iint d\bar{\rho}_f \, \tilde{U}_f(\bar{\rho}_f) \, U_{01}^*(\bar{\rho}_f) \right|^2 \leq \iint d\bar{\rho}_f \left| \tilde{U}_f(\bar{\rho}_f) \right|^2 \iint d\bar{\rho}_f \left| U_{01}^*(\bar{\rho}_f) \right|^2 \quad . \quad (2\text{-}13)$$

Recalling that the LP_{01} modal distribution is normalized to unit power, we see that the second double integral equals unity. We are then left with the integral of $\tilde{U}_f(\bar{\rho}_f)$ over the area of the imaged spot. If we then assume $\tilde{U}_f(\bar{\rho}_f)$ is constant over the fiber core, we obtain

$$\tilde{P}_{sig} \leq \iint d\bar{\rho}_f \left| \tilde{U}_f(\bar{\rho}_f) \right|^2 = \left| \tilde{U}_f \right|^2 \times \int_0^{reff} \int_0^{2\pi} r \, dr d\theta = P_R \quad . \quad (2\text{-}14)$$

Thus, the F/R coupling efficiency $\eta_{F/R} = P_{sig}/P_R$ *must* have an upper limit of 100%.

Another crucial drawback to the geometric model is the assumption of uniform target illumination by the transmitted beam. This restriction might be crudely met by some sort of beam-shaping technique that generates a top-hat beam in the far field. Unfortunately, this process is at best a difficult requirement to design into a common laser radar system. Uniform illumination could also be accomplished by assuming the transmitted beam is a spatially broad Gaussian. Then, if the target diameter itself is not much wider than the peak of the beam, one could approximate the illumination as nearly uniform. For a real system, however, this is clearly very wasteful of the transmitted energy.

Furthermore, this geometric model also fails to account for any information resulting from the diffuse nature of the target. The assumption that the received field is constant over the plane of the fiber endface may not always be true, and thus provides a poor representation of the true spatial distribution of the target's return field throughout the singlemode region. Thus we see that the assumptions made for the geometric

development, although common, are clearly suspect. Therefore, the remainder of this article will focus on developing a more complete ladar system analysis, accounting for all field diffraction and target effects.

2.2 General Illumination Terminology

Before continuing, we will set forth a pair of working definitions that completely describe the nature of the target in terms of both the transmitter and receiver optics. Once again assuming a Gaussian transmit beam, we illuminate an object at some range L from the transmitter. If the target extent is smaller than the illumination "footprint" at the plane of the target, the target is said to be *unresolved* or *flood-illuminated.* Conversely, if the object is larger than the illumination footprint, the target is said to be *resolved.* These definitions are illustrated in Figure 2.4.

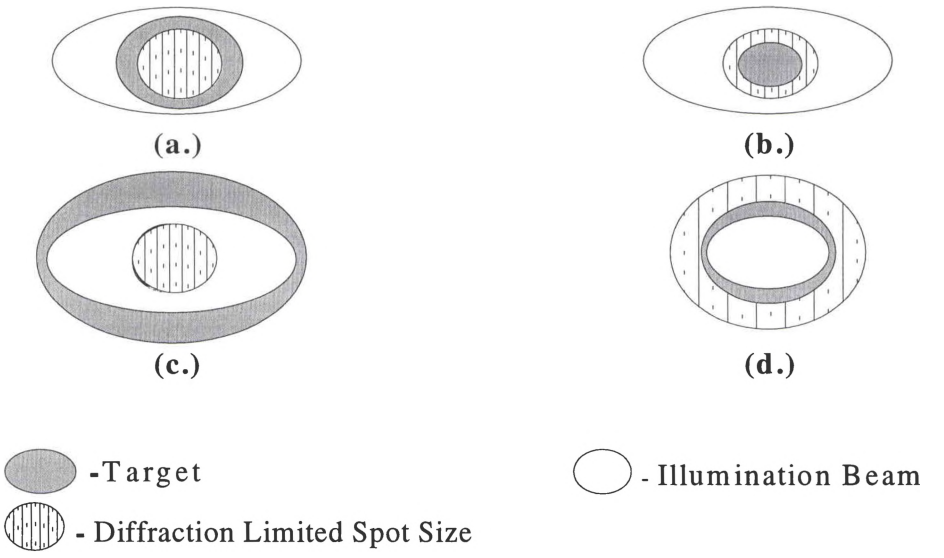

Figure 2.4: Target illumination/return illustrations for a.) unresolved target, multimode return, b.) unresolved target, singlemode return, c.) resolved target, multimode return, d.) resolved target, singlemode return.

It is important to note that by definition, the resolved or unresolved target quality is only a function of the ladar system transmitter. In order to fully describe the general nature of the target, we must examine the receiver leg as well.

We will *define* a target return to be *singlemode* if the target's illuminated portion lies fully within the diffraction limited spot size of the receiver entrance aperture, back propagated to the target plane. Recall, the diameter D_{DLS} of the diffraction limited spot can be determined from the following expression,[11]

$$D_{DLS} = \frac{2.44\lambda L}{D_R} \qquad (2\text{-}15)$$

where λ is the wavelength of the illumination beam and D_R is the diameter of the receiver aperture/pupil. Under the singlemode return condition, there is an approximate one-to-one geometric spatial matching of illuminated points on the target to points at or near the fiber core if the receiver is matched to the NA of the fiber. By restricting the signal coupling to an approximate one-to-one imaging relationship for a singlemode return, we are not at all restricting the possibility that a wide range of spatial frequencies may be excited by the target. For example, if the target is a small, diffuse cone falling within the diffraction limited spot size of the receiver aperture, the reflected light will have a high spatial frequency content, most of which will not be collected by the receiver optics. Yet the return signal will still be considered singlemode because for the light actually collected and focused onto the fiber core, we will still have a one-to-one spatial matching relationship to points on the target. Conversely, any target whose transverse, illuminated extent is greater than that of the diffraction limited spot size of the receiver will then defined as *multimode*.

Some comments regarding the above definitions, especially the singlemode versus multimode return definitions, are in order. Primarily, the above definitions are made only for conversational convenience. Though our definitions serve our purposes quite well, other just as suitable definitions could be proposed. Regardless, these definitions in no way influence the mathematical development which will follow. Furthermore, in the singlemode/multimode definitions, no attempt at all has been made to indicate that any system parameter or characteristic, including $\eta_{F/R}$ and $\eta_{F/T}$, has been optimized. For example, as we can see from Figure 2.3, and will also see later, the received power coupling efficiency generally tends to increase with target range. Our singlemode/multimode return definition simply allows us to conveniently and rationally designate a boundary beyond which coupling efficiency makes a clear transition from "poor" to "better/good". Specifically for Figure 2.3, using a wavelength of 1.5 μm, a target diameter of 30 cm, and a receiver aperture diameter of 10 cm, from Eq. (2-15), the distance L at which the resolution spot size equals the target diameter is readily found to be 8.2 km. It is then a simple matter to see that multimode returns result for target ranges less than 8.2 km, while singlemode returns result for target ranges greater than 8.2 km. Equipped with our definitions, we will now develop our general illumination models, incorporating whether the target is resolved or unresolved and whether or not its illumination characteristics produce singlemode or multimode returns.

CHAPTER III

Baseline Coupling Efficiency Analysis for a Direct Detection Ladar System Incorporating a Single Mode Optical Fiber

In Figure 2.3, we showed that the geometric coupling efficiency analysis of a direct detection ladar system predicted 100% coupling once the target moved past a range of about 16 km. We instinctively anticipate that this can not be the case. Therefore, in this chapter, we will analyze the direct detection ladar system more thoroughly and develop an expression for the receiver to fiber coupling efficiency $\eta_{F/R}$ that accounts for all beam diffraction effects, other than turbulence, occurring within the system. We will then compare this full analysis to the geometric analysis of Chapter II. For notational purposes, once again a boldface quantity will represent a complex field, an overscore will denote a vector quantity, and a tilde will indicate a random field.

3.1 Field at the Fiber Endface

Following the general analysis developed by Jacob *et al.* for a resolved target with a singlemode return, a comprehensive model capable of effectively predicting the $\eta_{F/R}$ for general target illumination [i.e., resolved or unresolved] in a bistatic system will be

developed. For this undertaking, as we will concentrate on the system shown in Figure 3.1 below.

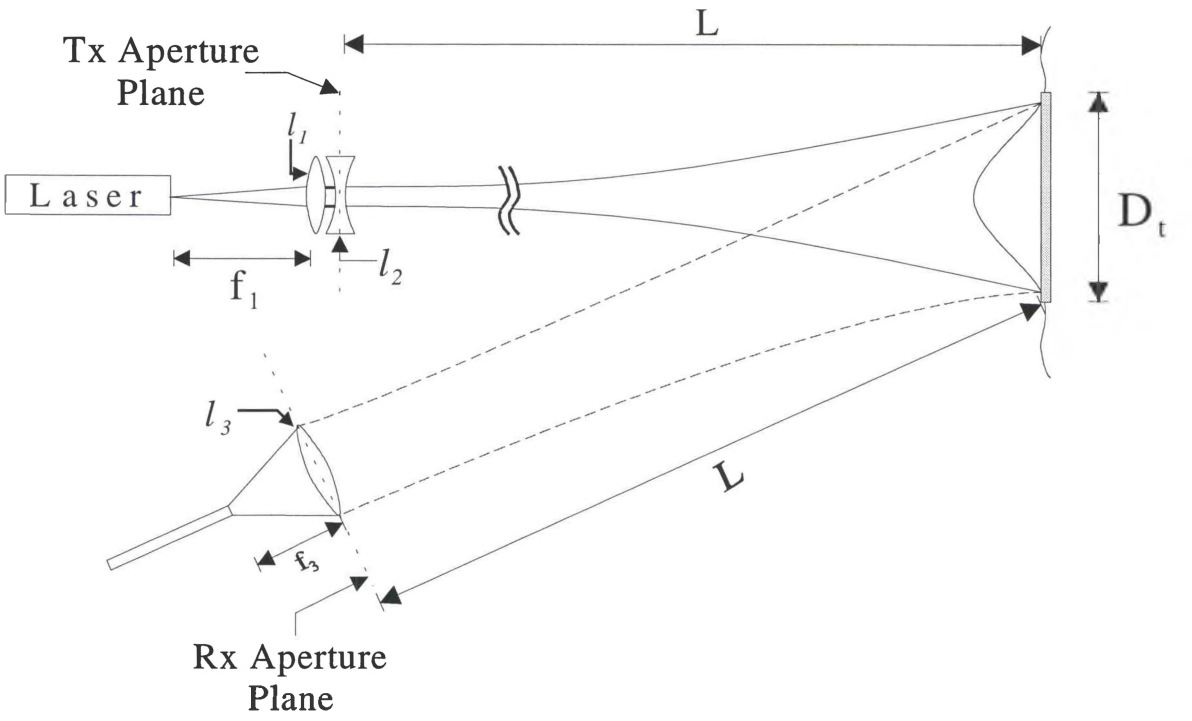

Figure 3.1: General Illumination LADAR system demonstrating a multimode return from a unresolved target. In an actual LADAR system, the TX and RX would be colinearly aligned.

Note, L is the distance to the target, D_t is the target diameter, f_1 is the focal length of the transmitter collimating optic l_1, and f_3 is the focal length of the receiver optic l_3. Here, we have also assumed for simplicity that all necessary transmitter beam expansion is accomplished by inserting a single negative lens l_2 immediately after the transmitter collimating optic l_1 placed one focal length away from the laser output. Thus, by adjusting the focal length of just this one lens, one can either spot or flood illuminate the target. This effect of varying the focal length of l_2 will be discussed in greater detail in Section 3.3. Furthermore, as stated earlier in Chapter I, the minimum loss of energy upon transmission occurs when the truncation ratio of the transmitter aperture diameter [i.e. the

diameter of l_1] to the transmitted beam waist is at an optimum of R=4. Therefore, both l_1 and l_2 are chosen to meet this stipulation. The telescope/coupling optic shown in Figure 2.1 will also be replaced by one large, fiber NA matched coupling lens l_3 for simplicity.

To proceed with the analysis, the nature of the received field at the fiber endface $\tilde{\mathbf{U}}_f(\bar{\rho}_f)$ must first be determined. This can be found by propagating the transmitted field $\mathbf{U}_{Trans}(\bar{\rho})$, where $\bar{\rho}$ is two dimensional spatial variable associated with the transmitter plane after l_1, to the target plane. This target plane field can be expressed via the integral product of the transmitted field, the phase curvature induced by the negative lens l_2, and the free space Green's function $h(\bar{\rho}_t - \bar{\rho})$ given as[12]

$$h(\bar{\rho}_t - \bar{\rho}) = \frac{e^{ikL}}{i\lambda L}\exp\left[\frac{ik}{2L}|\bar{\rho}_t - \bar{\rho}|^2\right] \quad , \tag{3-1}$$

where $\bar{\rho}_t$ is the spatial variable associated with the target plane, λ is the source wavelength, k is the free space wavenumber, and L is the distance to the target. The resulting field at the target $\mathbf{U}_t(\bar{\rho}_t)$ is then

$$\mathbf{U}_t(\bar{\rho}_t) = \iint_{A_{Trans}} d\bar{\rho}\mathbf{U}_{Trans}(\bar{\rho})\exp\left(\frac{ik}{2f_2}|\bar{\rho}|^2\right)h(\bar{\rho}_t - \bar{\rho}) \quad , \tag{3-2}$$

where A_{Trans} is the transmitter aperture and f_2 is the focal length of the negative transmitter lens l_2. We then multiply by the complex target reflectivity $\tilde{\mathbf{T}}(\bar{\rho}_t)$ and back propagate the reflected field to the receiver lens l_3 with another Green's function. The field before the receiver, $\tilde{\mathbf{U}}_R(\bar{\rho}_R)$, can thus be written as

$$\tilde{\mathbf{U}}_R(\bar{\rho}_R) = \iint_{A_t} d\bar{\rho}_t \, \tilde{\mathbf{T}}(\bar{\rho}_t)\mathbf{U}_t(\bar{\rho}_t)\, h(\bar{\rho}_R - \bar{\rho}_t) \quad , \tag{3-3}$$

where A_t is the target area and $\bar{\rho}_R$ is the spatial variable associated with the receiver plane. The field then passes through lens l_3 and is propagated to the fiber endface. Thus, the field at the fiber $\tilde{\mathbf{U}}_f(\bar{\rho}_f)$ is given by

$$\tilde{\mathbf{U}}_f(\bar{\rho}_f) = \iint_{A_R} d\bar{\rho}_R \tilde{\mathbf{U}}_R(\bar{\rho}_R) \exp\left(-\frac{ik}{2f_3}|\bar{\rho}_R|^2\right) h(\bar{\rho}_f - \bar{\rho}_R) \quad , \tag{3-4}$$

where A_R is the area of the receiver aperture and f_3 is the focal length of the receiver lens l_3. Now, by defining a receiver aperture function, $W_R(\bar{\rho}_R)$, the limits of integration on the $d\bar{\rho}_R$ integral in Eq. (3-4) can be extended to infinity. Combining Eqs. (3-2), (3-3), and (3-4), the field at the fiber endface can then be expressed according to the following nested integral relationship

$$\begin{aligned}
\tilde{\mathbf{U}}_f(\bar{\rho}_f) = {} & \frac{\exp(i2kL)\exp(ikf_3)}{(i\lambda f_3)(\lambda L)^2} \exp\left(\frac{ik}{2f_3}|\bar{\rho}_f|^2\right) \\
& \times \iint d\bar{\rho}_R \, W_R(\bar{\rho}_R) \exp\left(-\frac{ik}{f_3}\bar{\rho}_f \cdot \bar{\rho}_R\right) \\
& \times \iint_{A_t} d\bar{\rho}_t \, \tilde{\mathbf{T}}(\bar{\rho}_t) \exp\left(\frac{ik}{2L}\left(|\bar{\rho}_t|^2 + |\bar{\rho}_R|^2 - 2\bar{\rho}_t \cdot \bar{\rho}_R\right)\right) \\
& \times \iint_{A_{Trans}} d\bar{\rho} \, \mathbf{U}_{Trans}(\bar{\rho}) \exp\left(\frac{ik}{2f_2}|\bar{\rho}|^2\right) \exp\left(\frac{ik}{2L}\left(|\bar{\rho}|^2 + |\bar{\rho}_t|^2 - 2\bar{\rho} \cdot \bar{\rho}_t\right)\right)
\end{aligned} \quad . \tag{3-5}$$

Upon examination of this expression, several simplifying assumptions can be made. The quadratic phase term in $\bar{\rho}_f$ is negligible since realistically the diameter of the fiber core is on the order of a few microns while the focal length f_3 of the receiver optics is on the order of several centimeters. The quadratic phase term resulting from $\bar{\rho}$ can be

ignored as well. By incorporating the negative lens l_2 into the system shown in Figure 2.1, we can ensure that the target is always in the far field relative to the transmitter, making the $\bar{\rho}$ quadratic term over λL insignificant. This point will be fully illustrated in Section 3.3. This argument, however, does not apply to the receiver. Assuming a typical receiver aperture diameter of 10 cm and an operating wavelength of $\lambda = 1.5$ μm, for a 10 cm target to be in the far field with respect to the receiver [i.e. $A_{Target} << \lambda L$], it must be at a range of nearly 52 km. Therefore, since many targets of interest are much closer than this, the quadratic phase term associated with $\bar{\rho}_R$ can not be ignored.

After eliminating negligible terms, we find that Eq. (3-5) can be rearranged more compactly as

$$\begin{aligned}\tilde{\mathbf{U}}_f(\bar{\rho}_f) = \frac{\exp\left(ik\left(2L+f_3\right)\right)}{(i\lambda f_3)(\lambda L)^2}\iint_{A_t} d\bar{\rho}_t\, \tilde{\mathbf{T}}(\bar{\rho}_t)\exp\left(\frac{i2\pi}{\lambda L}|\bar{\rho}_t|^2\right) \\ \times \iint_{A_{Trans}} d\bar{\rho}\; \mathbf{U}'_{Trans}(\bar{\rho})\exp\left(-\frac{i2\pi}{\lambda L}\bar{\rho}\cdot\bar{\rho}_t\right) \\ \times \iint d\bar{\rho}_R\, W_R(\bar{\rho}_R)\exp\left(\frac{i\pi}{\lambda L}|\bar{\rho}_R|^2\right)\exp\left(-i2\pi\bar{\rho}_R\cdot\left(\frac{\bar{\rho}_t}{\lambda L}+\frac{\bar{\rho}_f}{\lambda f_3}\right)\right)\end{aligned} \quad , \tag{3-6}$$

where $\mathbf{U}'_{Trans}(\bar{\rho})$ incorporates the phase curvature introduced by lens l_2 and is defined as

$$\mathbf{U}'_{Trans}(\bar{\rho}) = \mathbf{U}_{Trans}(\bar{\rho})\exp\left(\frac{ik}{2f_2}|\bar{\rho}|^2\right) \quad . \tag{3-7}$$

Now, if we assume that the truncation of the transmitted beam is insignificant [i.e., R = 4], the limits of integration over the A_{Trans} integral can be extended out to infinity. Therefore, the $d\bar{\rho}$ integral in Eq. (3-6) simply becomes the Fourier transform $\mathcal{U}'_{trans}$ of Eq. (3-7), giving us the following expression for the field at the fiber endface

$$\tilde{U}_f(\bar{\rho}_f) = \frac{\exp\left(ik\left(2L + f_3\right)\right)}{(i\lambda f_3)(\lambda L)^2} \iint_{A_t} d\bar{\rho}_t \, \tilde{T}(\bar{\rho}_t) \exp\left(\frac{i2\pi}{\lambda L}\left|\bar{\rho}_t\right|^2\right) \mathcal{U}'_{Trans}\left(\frac{\bar{\rho}_t}{\lambda L}\right)$$
$$\times \iint d\bar{\rho}_R \, W_R(\bar{\rho}_R) \exp\left(\frac{i\pi}{\lambda L}\left|\bar{\rho}_R\right|^2\right) \exp\left(-i2\pi\bar{\rho}_R \cdot \left(\frac{\bar{\rho}_t}{\lambda L} + \frac{\bar{\rho}_f}{\lambda f_3}\right)\right) \quad . \quad (3\text{-}8)$$

Knowing the nature of the field at the fiber endface, we can now determine the amount of power coupled into the LP_{01} mode of the fiber.

3.2 Single-Mode Fiber F/R Coupling Efficiency

The power $\bar{P}_{sig}$ coupled into the fundamental mode of the receiving fiber can again be approximated by using the overlap integral given by Eq. (2-6). Yet, due to the random nature of the diffuse target, the expected signal power coupled into the LP_{01} mode of the fiber must now be found by taking the expected value of Eq. (3-8). Substituting Eq. (3-8) into Eq. (2-6) and rearranging terms we obtain the following expression for the expected signal power,

$$E\left[\tilde{P}_{sig}\right] \cong \frac{1}{(\lambda f_3)^2 (\lambda L)^4} \iint_{A_t} d\bar{\rho}_{t1} \, d\bar{\rho}_{t2} \, E\left[\tilde{T}(\bar{\rho}_{t1}) \tilde{T}^*(\bar{\rho}_{t2})\right] \exp\left(\frac{i2\pi}{\lambda L}\left|\bar{\rho}_{t1}\right|^2 - \left|\bar{\rho}_{t2}\right|^2\right)$$
$$\times \left|\mathcal{U}'_{Trans}\left(\frac{\bar{\rho}_t}{\lambda L}\right)\right|^2 \left| \iint d\bar{\rho}_f U_{01}^*(\bar{\rho}_f) \right. \quad , \quad (3\text{-}9)$$
$$\left. \times \iint d\bar{\rho}_R W_R(\bar{\rho}_R) \exp\left(\frac{i\pi}{\lambda L}\left|\bar{\rho}_R\right|^2\right) \exp\left[-i2\pi\bar{\rho}_R \cdot \left(\frac{\bar{\rho}_t}{\lambda L} + \frac{\bar{\rho}_f}{\lambda f_3}\right)\right] \right|^2$$

where $\bar{\rho}_{t1}$ and $\bar{\rho}_{t2}$ are dummy variables of integration associated with the target plane. Utilizing the following statistical relationships for a purely diffuse target,[13]

$$E\left[\tilde{T}(\bar{\rho}_{t1})\right] = 0$$
$$E\left[\tilde{T}(\bar{\rho}_{t1})\,\tilde{T}(\bar{\rho}_{t2})\right] = 0 \qquad , \qquad (3\text{-}10)$$
$$E\left[\tilde{T}(\bar{\rho}_{t1}), \tilde{T}^{*}(\bar{\rho}_{t2})\right] = \lambda^2 T_o(\bar{\rho}_{t1})\delta(\bar{\rho}_{t1} - \bar{\rho}_{t2})$$

where $T_o(\bar{\rho}_{t1}) = \tau(\bar{\rho}_{t1})/\pi$ is the diffuse, mean square reflection coefficient and $\tau(\bar{\rho}_{t1})$ is a unitless number associated with the target reflectivity ranging from 0 to 1, we can arrive at the following expression, after some rearrangement, for the expected value of the signal power coupled into the LP_{01} mode of the fiber,

$$E\left[\tilde{P}_{sig}\right] \cong \frac{1}{(\lambda f_3)^2(\lambda L)^4}\iint_{A_t} d\bar{\rho}_t\, T_o(\bar{\rho}_t)\left|\mathcal{U}'_{Trans}\left(\frac{\bar{\rho}_t}{\lambda L}\right)\right|^2$$
$$\times\left|\iint d\bar{\rho}_R W_R(\bar{\rho}_R)\exp\left(\frac{i\pi}{\lambda L}|\bar{\rho}_R|^2\right)\exp\left(-\frac{i2\pi}{\lambda L}\bar{\rho}_R\cdot\bar{\rho}_t\right)\right. \qquad . \qquad (3\text{-}11)$$
$$\left.\times\iint d\bar{\rho}_f U^{*}_{01}(\bar{\rho}_f)\exp\left(-\frac{i2\pi}{\lambda f_3}\bar{\rho}_R\cdot\bar{\rho}_f\right)\right|^2$$

However, since the target has already been assumed to be spatially stationary over A_t, if there are no variations in the reflectivity as a function of $\bar{\rho}_t$, T_o can be pulled out of the $d\bar{\rho}_t$ integral. One also notices that the $d\bar{\rho}_f$ integral is now simply the Fourier transform of the LP_{01} mode of the fiber. Now, expanding the magnitude squared around the $d\bar{\rho}_R$ and $d\bar{\rho}_f$ integrals we obtain

$$E\left[\tilde{P}_{sig}\right] \cong \frac{T_o}{f_3{}^2(\lambda L)^4}\iint_{A_t} d\bar{\rho}_t\left|\mathcal{U}'_{Trans}\left(\frac{\bar{\rho}_t}{\lambda L}\right)\right|^2$$
$$\times\iint d\bar{\rho}_R\,\mathcal{U}^{*}_{01}\left(\frac{\bar{\rho}_R}{\lambda f_3}\right)W_R(\bar{\rho}_R)\exp\left(\frac{i\pi}{\lambda L}|\bar{\rho}_R|^2\right)\exp\left(-\frac{i2\pi}{\lambda L}\bar{\rho}_R\cdot\bar{\rho}_t\right) \qquad , \qquad (3\text{-}12)$$
$$\times\iint d\bar{\rho}'_R\,\mathcal{U}_{01}\left(\frac{\bar{\rho}'_R}{\lambda f_3}\right)W^{*}{}_R(\bar{\rho}'_R)\exp\left(-\frac{i\pi}{\lambda L}|\bar{\rho}'_R|^2\right)\exp\left(\frac{i2\pi}{\lambda L}\bar{\rho}'_R\cdot\bar{\rho}_t\right)$$

where $\mathcal{U}_{01}$ is the Fourier transform of the fiber mode and $\bar{\rho}_R$ and $\bar{\rho}'_R$ are arbitrary receiver plane variables.

A Jacobian change of variables is now made to simplify the integration. By defining the following variables[14]

$$\bar{\rho}_o \equiv \frac{\bar{\rho}_R + \bar{\rho}'_R}{2} \text{ and } \Delta\bar{\rho} \equiv \bar{\rho}'_R - \bar{\rho}_R \quad \Rightarrow \iint d\bar{\rho}_R \iint d\bar{\rho}'_R = \iint d\bar{\rho}_0 \iint d\Delta\bar{\rho} \quad , \tag{3-13}$$

and making the appropriate substitution back into Eq. (3-12), we obtain

$$\begin{aligned} E\left[\tilde{P}_{sig}\right] \cong \frac{T_0}{f_3^{\,2}(\lambda L)^4} \iint d\Delta\bar{\rho} \iint d\bar{\rho}_t W_t(\bar{\rho}_t) \left| \mathcal{U}'_{Trans}\left(\frac{\bar{\rho}_t}{\lambda L}\right) \right|^2 \exp\left(-\frac{i2\pi}{\lambda L} \bar{\rho}_t \cdot \Delta\bar{\rho} \right) \\ \times \iint d\bar{\rho}_o \mathcal{U}^*_{01}\left(-\frac{\bar{\rho}_o}{\lambda f_3} + \frac{\Delta\bar{\rho}}{2\lambda f_3} \right) \mathcal{U}_{01}\left(-\frac{\bar{\rho}_o}{\lambda f_3} - \frac{\Delta\bar{\rho}}{2\lambda f_3} \right) \\ \times W_R(\bar{\rho}_0 - \tfrac{1}{2}\Delta\bar{\rho}) W^*{}_R(\bar{\rho}_0 + \tfrac{1}{2}\Delta\bar{\rho}) \exp\left(-\frac{i2\pi}{\lambda L} \bar{\rho}_o \cdot \Delta\bar{\rho} \right) \end{aligned} \quad . \tag{3-14}$$

In the above expression, we have also introduced a specific target function $W_t(\bar{\rho}_t)$, allowing us to extended the limits of integration over the target area out to infinity. This is now as far as we can proceed until some further information about the transmitted beam, the aperture functions W_t and W_R, and the modal field in the fiber are specified.

To continue with the analysis, we will define the untruncated, Gaussian field at lens l_1, $\mathbf{U}_{Trans}(\bar{\rho})$, normalized to the transmitted power P_{Trans}, to be

$$\mathbf{U}_{Trans}(\bar{\rho}) \equiv \sqrt{\frac{2P_{Trans}}{\pi\omega_o^2}} \exp\left(-\frac{|\bar{\rho}|^2}{\omega_o^2} \right) \quad . \tag{3-15}$$

Therefore, the field transmitted through the negative lens l_2 can be found by substituting Eq. (3-15) back into Eq. (3-7) yielding

$$\mathbf{U}'_{\text{Trans}}(\bar{\rho}) \equiv \sqrt{\frac{2P_{\text{Trans}}}{\pi\omega_o^2}} \exp\left(-\frac{|\bar{\rho}|^2}{\omega_o^2}\right) \exp\left(\frac{ik}{2f_2}|\bar{\rho}|^2\right) \quad . \tag{3-16}$$

Evaluating the Fourier transform of Eq. (3-16), for inclusion in Eq. (3-14) yields

$$\begin{aligned} \mathcal{F}\{\mathbf{U}'_{\text{Trans}}(\bar{\rho})\} &= \sqrt{\frac{2P_{\text{Trans}}}{\pi\omega_o^2}}\, \mathcal{F}\left\{\exp\left[\left(\frac{-1}{\omega_o^2}+\frac{ik}{2f_2}\right)|\bar{\rho}|^2\right]\Big|_{\bar{\rho}=\frac{\bar{\rho}_t}{\lambda L}}\right\} \\ &= \sqrt{\frac{2P_{\text{Trans}}}{\pi\omega_o^2}}\,\frac{\pi}{a'}\exp\left[-\frac{\pi^2}{a'(\lambda L)^2}|\bar{\rho}_t|^2\right] \end{aligned} \quad , \tag{3-17}$$

where a' equals

$$a' \equiv \frac{1}{\omega_o^2} - \frac{ik}{2f_2} \quad . \tag{3-18}$$

Rationalizing the denominators of the two terms not under the square root gives us the following expression,

$$\frac{\pi}{a'}\exp\left[\frac{-\pi^2}{a'(\lambda L)^2}|\bar{\rho}_t|^2\right] = \frac{2\pi f_2\omega_o^2\left(2f_2+ik\omega_o^2\right)}{\left(2f_2\right)^2+\left(k\omega_o^2\right)^2}\exp\left[-\frac{2\pi^2 f_2\omega_o^2}{(\lambda L)^2}\frac{\left(2f_2+ik\omega_o^2\right)}{\left(2f_2\right)^2+\left(k\omega_o^2\right)^2}|\bar{\rho}_t|^2\right]. \tag{3-19}$$

Thus, substituting Eq. (3-19) into Eq. (3-17) and taking the magnitude squared of the resulting expression gives us the following for the Fourier transform of the transmitted field

$$\left|\mathcal{U}'_{\text{Trans}}\left(\frac{\bar{\rho}_t}{\lambda L}\right)\right|^2 = \frac{8\pi P_{\text{Trans}} f_2^2\omega_o^2}{4f_2^2+\left(k\omega_o^2\right)^2}\exp\left[-\frac{8\pi^2 f_2^2\omega_o^2}{(\lambda L)^2\left(4f_2^2+\left(k\omega_o^2\right)^2\right)}|\bar{\rho}_t|^2\right] \quad . \tag{3-20}$$

The $d\bar{\rho}_t$ integral in Eq. (3-14) is now an integral over a Gaussian with a complicated waist multiplied by a phase factor over the target area $W_t(\bar{\rho}_t)$. To evaluate

the integral, we will assume for this analysis that the target area is circular in shape, with a diameter D_t, and is given by the expression below

$$W_t(\bar{\rho}_t) = \mathrm{circ}\left(\frac{\bar{\rho}_t}{D_t}\right) \equiv \begin{cases} 1, & |\bar{\rho}_t| \le \dfrac{D_t}{2} \\ 0, & |\bar{\rho}_t| > \dfrac{D_t}{2} \end{cases} \quad . \tag{3-21}$$

Similarly, our receiver aperture function $W_R(\bar{\rho})$ will be defined as a circular disk of diameter D_R given by

$$W_R(\bar{\rho}) = \mathrm{circ}\left(\frac{\bar{\rho}}{D_R}\right) \equiv \begin{cases} 1, & |\bar{\rho}| \le \dfrac{D_R}{2} \\ 0, & |\bar{\rho}| > \dfrac{D_R}{2} \end{cases} \quad . \tag{3-22}$$

In addition, we will let the field distribution of the fiber mode again be given by Eq. (2-7). Substituting Eqs. (2-7), (3-20), (3-21), and (3-22) back into Eq. (3-14) and scaling the $d\bar{\rho}_t$ and former $d\bar{\rho}_R$ variables of integration by D_t and D_R respectively, we obtain the following expression

$$\begin{aligned} E\left[\tilde{P}_{sig}\right] \cong & \frac{4NT_0P_{Trans}D_R^2D_t^2a^2}{L^2}\iint d\Delta\bar{\rho}\exp\left[-a^2|\Delta\bar{\rho}|^2\right] \\ & \times\iint d\bar{\rho}_t \mathrm{circ}(\bar{\rho}_t)\exp\left(-N\pi^2D_t^2|\bar{\rho}_t|^2\right)\exp\left(\frac{-i2\pi D_R D_t}{\lambda L}\bar{\rho}_t\cdot\Delta\bar{\rho}\right) \\ & \times\iint d\bar{\rho}_o \mathrm{circ}(\bar{\rho}_0-\tfrac{1}{2}\Delta\bar{\rho})\mathrm{circ}(\bar{\rho}_0+\tfrac{1}{2}\Delta\bar{\rho})\exp\left(-4a^2|\bar{\rho}_0|^2\right) \\ & \times\exp\left(\frac{-i2\pi D_R}{\lambda L}\bar{\rho}_0\cdot\Delta\bar{\rho}\right) \end{aligned} \quad , \tag{3-23}$$

where N and *a* are collections of constants associated with the transmitter and receiver respectively, defined as follows

$$N \equiv \frac{8f_2^2\omega_o^2}{(\lambda L)^2\left(4f_2^2 + \left(k\omega_o^2\right)^2\right)} \quad , \tag{3-24}$$

and

$$a^2 \equiv \frac{1}{2}\left(\frac{\pi\omega D_R}{\lambda f_3}\right)^2 = 2\left(\frac{\pi\omega NA_{optics}}{\lambda}\right)^2 \quad . \tag{3-25}$$

In Section 3.3, the significance of the focal length f_2 within the N parameter will be discussed in greater detail.

Recognizing that the two circ functions in the receiver plane are now unit diameter functions centered at $\pm\Delta\bar{\rho}/2$, the $d\bar{\rho}_o$ integral is merely the area of overlap between the two functions. This observation is depicted in Figure 3.2.

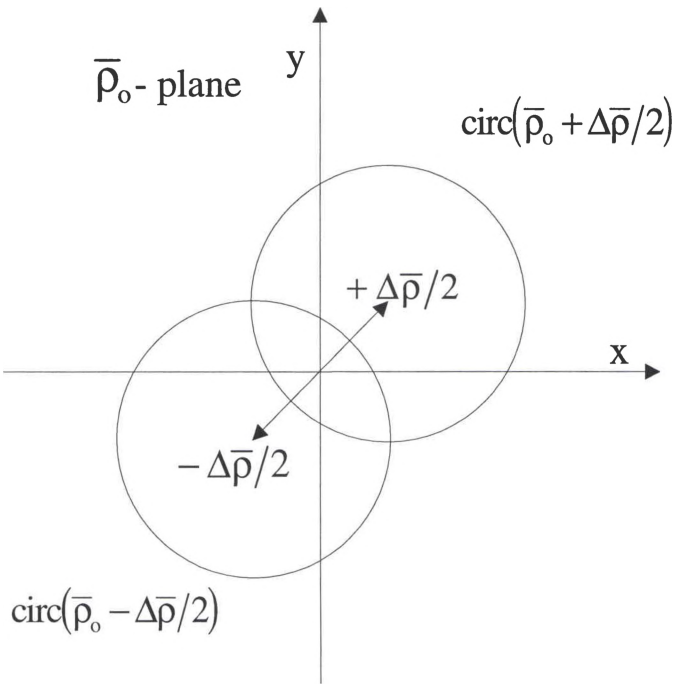

Figure 3.2: Circ function overlap.

Upon inspection of the figure, we see that if the separation between the two centers of the circ functions is greater than one [i.e., $|\Delta\bar{\rho}| > 1$], there will be no overlap between the two functions. One also notices from Eq. (3-23) that the circ functions in both the target and receiver planes are weighted by a complex exponential term. If we then employ Euler's relationship, this exponential can be expanded into sine and cosine terms. Both the $d\bar{\rho}_t$ and $d\bar{\rho}_o$ integrals now contain even functions multiplied by an even cosine function and an odd sine function. With the limits on the integral extended to infinity, the area resulting from the sine term will be equal to zero due to the odd nature of the function. As a result, Eq. (3-23) then becomes

$$\begin{aligned} E\left[\tilde{P}_{sig}\right] \cong & \frac{4NT_0P_{Trans}D_R^2D_t^2a^2}{L^2}\iint d\Delta\bar{\rho}\exp\left[-a^2|\Delta\bar{\rho}|^2\right] \\ & \times\iint d\bar{\rho}_t \mathrm{circ}(\bar{\rho}_t)\exp\left(-N\pi^2D_t^2|\bar{\rho}_t|^2\right)\cos\left(\frac{2\pi D_R D_t}{\lambda L}\bar{\rho}_t\cdot\Delta\bar{\rho}\right) \\ & \times\iint d\bar{\rho}_o \mathrm{circ}(\bar{\rho}_0-\tfrac{1}{2}\Delta\bar{\rho})\mathrm{circ}(\bar{\rho}_0+\tfrac{1}{2}\Delta\bar{\rho})\exp\left(-4a^2|\bar{\rho}_0|^2\right) \\ & \times\cos\left(\frac{2\pi D_R}{\lambda L}\bar{\rho}_0\cdot\Delta\bar{\rho}\right) \end{aligned} \quad . \quad (3\text{-}26)$$

If we then make the following vector substitutions

$$\Delta\bar{\rho} \equiv r\cos\theta\hat{x} + r\sin\theta\hat{y}, \quad \bar{\rho}_t \equiv x_t\hat{x} + y_t\hat{y}, \quad \text{and} \quad \bar{\rho}_o \equiv x\hat{x} + y\hat{y} \quad , \quad (3\text{-}27)$$

the dot products inside the cosine terms become

$$\bar{\rho}_t\cdot\Delta\bar{\rho} = rx_t\cos\theta + ry_t\sin\theta \quad \text{and} \quad \bar{\rho}_o\cdot\Delta\bar{\rho} = rx\cos\theta + ry\sin\theta \quad . \quad (3\text{-}28)$$

Yet, recognizing that all three integrals in Eq. (3-26) are circularly symmetric, the $d\bar{\rho}_o$, $d\bar{\rho}_t$, and $d\Delta\bar{\rho}_o$ integrals are independent of the angle associated with the $\Delta\bar{\rho}$ shift. This makes it possible to choose a convenient direction for $\Delta\bar{\rho}$ in which to calculate the area of overlap between the two circ functions. For this analysis, we will consider a shift

occurring along the y axis, [i.e., $\theta = 90^\circ$]. Expressing the $d\Delta\bar{\rho}$ integral in polar coordinates and using the circ functions to define the bounds of the target area and receiver area, the expected value of the coupled signal power becomes,

$$E\left[\tilde{P}_{sig}\right] \cong \frac{128\pi N T_0 P_{Trans} D_R^2 D_t^2 a^2}{L^2} \int_0^1 dr\, r \exp\left[-a^2 r^2\right]$$
$$\times \int_0^{\frac{1}{2}} dx_t \exp\left(-N\pi^2 D_t^2 x_t^{\,2}\right) \int_0^{\sqrt{\frac{1}{4}-x_t^2}} dy_t \exp\left(-N\pi^2 D_t^2 y_t^{\,2}\right) \cos\left(\frac{2\pi D_R D_t r y_t}{\lambda L}\right) \quad (3\text{-}29)$$
$$\times \int_0^{\frac{1}{2}\sqrt{1-r^2}} dx \exp\left(-4a^2 x^2\right) \int_0^{\sqrt{\frac{1}{4}-x^2}-\frac{r}{2}} dy \exp\left(-4a^2 y^2\right) \cos\left(\frac{2\pi D_R{}^2 r y}{\lambda L}\right)$$

Note, the bounds over the former $d\bar{\rho}_t$ and $d\bar{\rho}_o$ integrals show the area of only one quadrant of the unit circle and the integrals have been multiplied by a factor of four to obtain the entire area of the circle.

To compute the received power coupling efficiency $\eta_{F/R}$, we take the ratio of the expected power coupled into the fiber mode to the expected power collected by the receiver aperture [i.e. $\eta_{F/R} = E(P_{sig})/E(P_R)$]. Therefore, we must now determine the nature of the field at the receiver and determine how much energy is actually collected. From Eqs. (3-1), (3-2), and (3-3), we can show that the field at the receiver plane is given by

$$\tilde{U}_R(\bar{\rho}_R) = \frac{\exp(i2kL)}{(\lambda L)^2} \iint_{A_t} d\bar{\rho}_t \tilde{T}(\bar{\rho}_t) \exp\left(\frac{ik}{2L}\left(|\bar{\rho}_t|^2 + |\bar{\rho}_R|^2 - 2\bar{\rho}_t \cdot \bar{\rho}_R\right)\right)$$
$$\times \iint_{A_{Trans}} d\bar{\rho} U_{Trans}(\bar{\rho}) \exp\left(\frac{ik}{2f_2}|\bar{\rho}|^2\right) \exp\left(\frac{ik}{2L}\left(|\bar{\rho}_t|^2 - 2\bar{\rho}.\bar{\rho}_t\right)\right), \quad (3\text{-}30)$$

providing the assumption $A_{Trans} << \lambda L$ is made. The irradiance I_R at the receiver plane is then simply the magnitude squared of $\tilde{U}_R$. Given that the transmit beam is untruncated, this irradiance can be written as

$$\tilde{I}_R = \frac{1}{(\lambda L)^4}\iint_{A_t} d\bar{\rho}_t \tilde{T}(\bar{\rho}_t)\exp\left(\frac{ik}{L}|\bar{\rho}_t|^2\right)\exp\left(-\frac{ik}{L}\bar{\rho}_R\cdot\bar{\rho}_t\right)\mathcal{U}'_{Trans}\left(\frac{\bar{\rho}_t}{\lambda L}\right)$$
$$\times\iint_{A_t} d\bar{\rho}'_t \tilde{T}^*(\bar{\rho}'_t)\exp\left(-\frac{ik}{L}|\bar{\rho}'_t|^2\right)\exp\left(\frac{ik}{L}\bar{\rho}_R\cdot\bar{\rho}'_t\right)\mathcal{U}'^*_{Trans}\left(\frac{\bar{\rho}'_t}{\lambda L}\right), \quad (3\text{-}31)$$

where $\mathcal{U}'_{Trans}$ is the Fourier transform given by Eq. (3-17). Now, by applying the target statistics of Eq. (3-10) and making use of Eq. (3-20), the expected value of the total irradiance at the receiver plane reduces to

$$E\left[\tilde{I}_R\right] = \frac{NT_o\pi P_{Trans}}{L^2}\iint d\bar{\rho}_t \mathrm{circ}\left(\frac{\bar{\rho}_t}{D_t}\right)\exp\left(-N\pi^2|\bar{\rho}_t|^2\right), \quad (3\text{-}32)$$

where we have extended the limits on the $d\bar{\rho}_t$ to infinity by incorporating the target function in Eq. (3-21). Expressing the $d\bar{\rho}_t$ integral in polar coordinates and using the circ function to set bounds on the limits of integration, we obtain after integrating,

$$E\left[\tilde{I}_R\right] = \frac{T_o P_{Trans}}{L^2}\left[1-\exp\left(-\frac{ND_t^2\pi^2}{4}\right)\right]. \quad (3\text{-}33)$$

The above expression is then the expected value of the irradiance at the receiver plane. However, the power received will be limited by the extent of the receiver aperture and thus, can be found by multiplying Eq. (3-31) by the area of the receiver to yield,

$$E\left[\tilde{P}_R\right] = \frac{T_o P_{Trans}\pi D_R^2}{4L^2}\left[1-\exp\left(-\frac{ND_t^2\pi^2}{4}\right)\right]. \quad (3\text{-}34)$$

Finally, dividing Eq. (3-29) by Eq. (3-34), we obtain the final expression for $\eta_{F/R}$ for a general illumination ladar system incorporating a single mode optical fiber receiver. This equation is,

$$\eta_{F/R} = \frac{E\left[\tilde{P}_{sig}\right]}{E\left[\tilde{P}_R\right]} \cong \frac{512Na^2D_t^{\,2}}{1-\exp\left(-\frac{ND_t^2\pi^2}{4}\right)} \int_0^1 dr\, r \exp\left[-a^2r^2\right]$$

$$\times \int_0^{\frac{1}{2}} dx_t \exp\left(-N\pi^2D_t^2x_t^{\,2}\right) \int_0^{\sqrt{\frac{1}{4}-x_t^2}} dy_t \exp\left(-N\pi^2D_t^2y_t^{\,2}\right) \cos\left(\frac{2\pi D_R D_t r y_t}{\lambda L}\right) \quad (3\text{-}35)$$

$$\times \int_0^{\frac{1}{2}\sqrt{1-r^2}} dx \exp\left(-4a^2x^2\right) \int_0^{\sqrt{\frac{1}{4}-x^2}-\frac{r}{2}} dy \exp\left(-4a^2y^2\right) \cos\left(\frac{2\pi D_R{}^2 r y}{\lambda L}\right)$$

In contrast to Eq. (2-11), this model allows for varying the truncation ratio at the transmitter, the beam diameter in the target plane, the transmission optics and coupling optics, as well as the target diameter and the range to target. We will also see in Appendix B that with the appropriate assumptions, Eq. (3-35) reduces to the result obtained by Jacob for a resolved target with a singlemode return.[2]

3.3 Comparison with Geometric Model

Recalling from Eq. (3-24) that N is a collection of constants dependent on the transmitted beam and the range to the target, most of the components of N will be given as system parameters. N is also dependent on the focal length of the negative lens f_2 in Figure 3.1 and must be determined separately based on the desired beam diameter at the target. Since the beam is collimated by lens l_1 before illuminating lens l_2, we may envision f_2 as the radius of curvature R on a transmitted wavefront emerging from a single, equivalent source in front of the transmitter exit aperture, as shown in Figure 3.3.

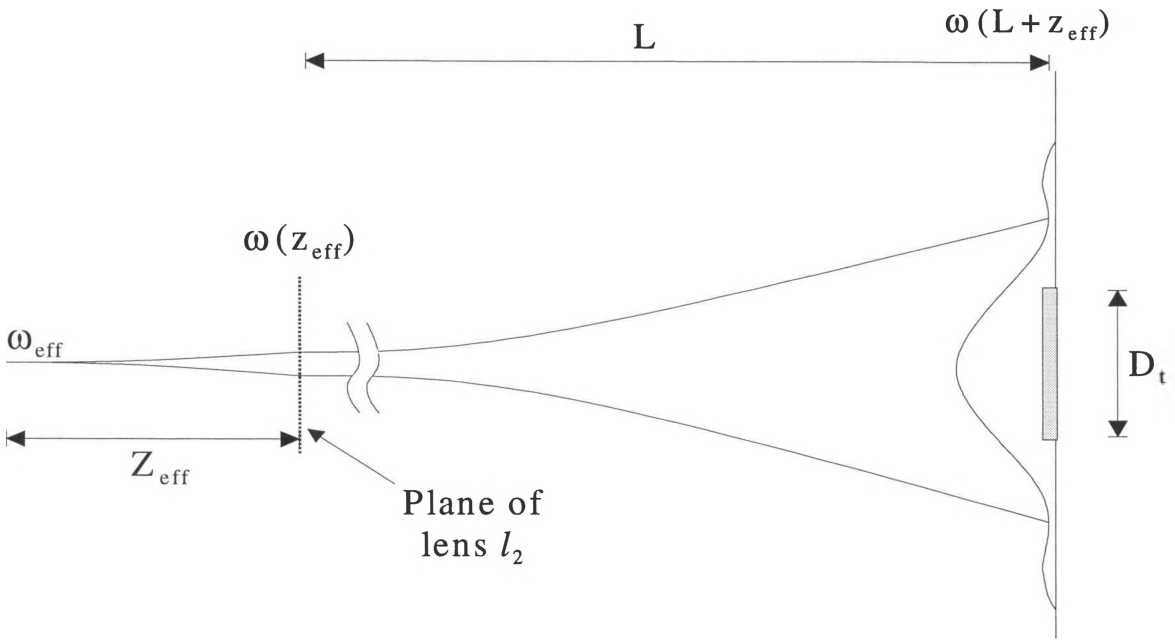

Figure 3.3: Illustration of the geometry used for calculating the focal length for the negative lens l_2.

Employing the propagation equations associated with Gaussian beams, the expression for the radius of curvature is,[11]

$$f_2 = R(z_{eff}) = z_{eff}\left[1+\left(\frac{\pi\omega_{eff}^2}{\lambda z_{eff}}\right)^2\right] \quad , \tag{3-36}$$

where ω_{eff} and z_{eff} are the effective beam waist and its effective distance behind lens l_2 respectively. These quantities can in turn be found by simultaneously solving the expressions for the Gaussian beam spot size at the plane of lens l_2 and at the target, respectively[11]

$$\omega(z_{eff}) = \omega_{eff}\left[1+\left(\frac{\lambda z_{eff}}{\pi\omega_{eff}^2}\right)^2\right]^{\frac{1}{2}} \quad , \tag{3-37}$$

$$\omega\left(L+z_{eff}\right)=\omega_{eff}\left[1+\left(\frac{\lambda\left(L+z_{eff}\right)}{\pi\omega_{eff}^{2}}\right)^{2}\right]^{\frac{1}{2}} \qquad (3\text{-}38)$$

To compare with the earlier geometric analysis where uniform target illumination was assumed, we consider a large beam diameter of $2\omega\left(L+z_{eff}\right)$=15 m on a small target at 20 km and a beam diameter of $2\omega\left(z_{eff}\right)$ = 2.5 cm, for a truncation ratio of R=4, at lens l_2. Using a wavelength of λ = 1.5 μm, the effective spot size and the effective distance from the transmitter exit aperture are found to be ω_{eff} = 1.27 mm and z_{eff} = 66.80 m, respectively. This corresponds to a radius of curvature, or focal length, of f_2= -66.98 m at the negative lens. Although this value is rather large, one can easily generate this type of effective lens with modern liquid crystal devices similar to those currently under investigation in our laboratory.[15]

Next, to verify that the target is in the far field with respect to the transmitter, the Rayleigh distance, z_R, can be determined for the above system. This range is given by[11]

$$z_R=\frac{\pi\omega_{eff}^{2}}{\lambda}=3.42\text{m} \qquad (3\text{-}39)$$

Therefore, to satisfy the far field condition, the target range L must be large enough that L > 34.2 m from the *effective* beam waist. Yet, with the effective beam waist 66.80 m from the negative lens, as long as the target is *anywhere* in front of the transmitter, the far field condition is satisfied. Thus, with the addition of the negative lens at the transmitter, the range to which the general illumination model is valid has been extended to any distance in front the transmitter, so long as the proper beam expansion focal length is chosen for l_2.

Equation (3-35) can now be evaluated numerically by substituting the appropriate values for receiver diameter (D_R = 10 cm) and target diameter (D_t = 0.3 m) from the geometric analysis. The ω and a parameters are then calculated by substituting the fiber core diameter of 8.3 μm and a normalized frequency parameter value of V = 2.26 into Eq. (2-9) and Eq. (3-25) respectively. Equation (3-35) is then evaluated using the numerical integration techniques of the *Mathematica* software package. Figure 3.4 is then a plot of $\eta_{F/R}$ vs. target range for both the geometrical model and full, general illumination model.

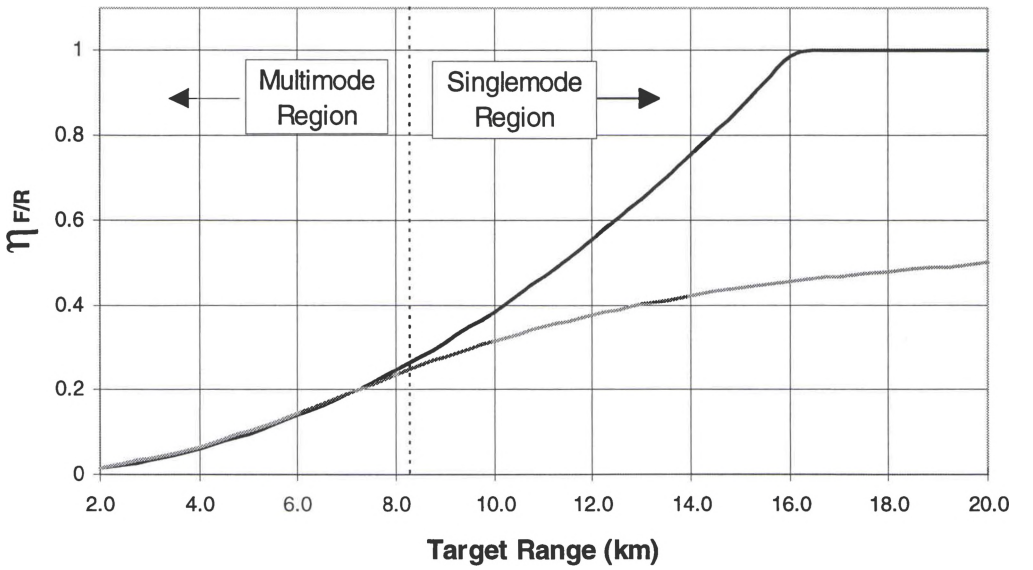

Figure 3.4: Received power coupling efficiency ($\eta_{F/R}$) vs. target range for a target diameter of 0.3 m.

As one can see, both curves agree very well throughout the multimode region, as expected. After all, this is the region where the geometric optics model still holds. However, after the boundary at 8.2 km, unlike the geometric model, the general

illumination model slowly starts to level off and approaches 100% coupling efficiency only as L goes to infinity.

To demonstrate the flexibility of the coupling efficiency model given by Eq. (3-35), we now examine $\eta_{F/R}$ for a variable diameter, unresolved target at a constant range of L = 20 km. Figure 3.5 displays a plot of Eq. (3-35) vs. target diameter for a beam diameter of 15 m on target, while all other system parameters remain the same as in the previous example.

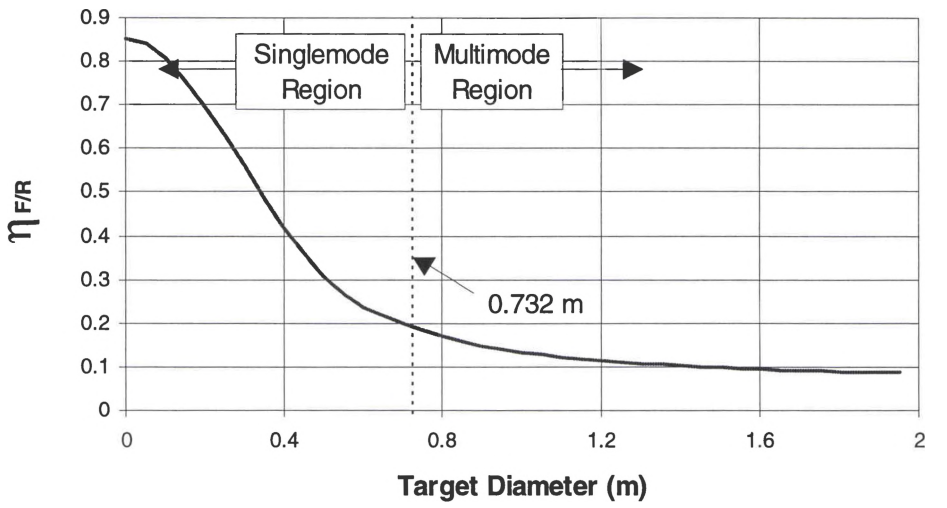

Figure 3.5: Receiver to fiber power coupling efficiency $\eta_{F/R}$ for a flood illuminated target vs. the illuminated target diameter at a constant range of 20 km.

As we see, at a fixed range $\eta_{F/R}$ increases as the diameter of the target decreases. This can readily be attributed to the singlemode nature of the returns from smaller targets. From Eq. (3-33), we see that the irradiance at the receiver aperture is essentially uniform [i.e. the energy scattered by the target in all directions]. As a result, as the size of the target decreases, the solid angle into which a small target scatters the returning light is

much smaller. Therefore, a greater portion of the light incident on the receiver falls within the diffraction limited acceptance cone of the fiber mode.

F/R coupling efficiency can be shown to drop off with increasing illumination spot size in the target plane. Keeping the range to a 1 m diameter target constant at L = 20 km and letting all other system parameters remain the same as in the last example, Figure 3.6 displays a plot of $\eta_{F/R}$ in Eq. (3-35) vs. illumination spot radius in the target plane.

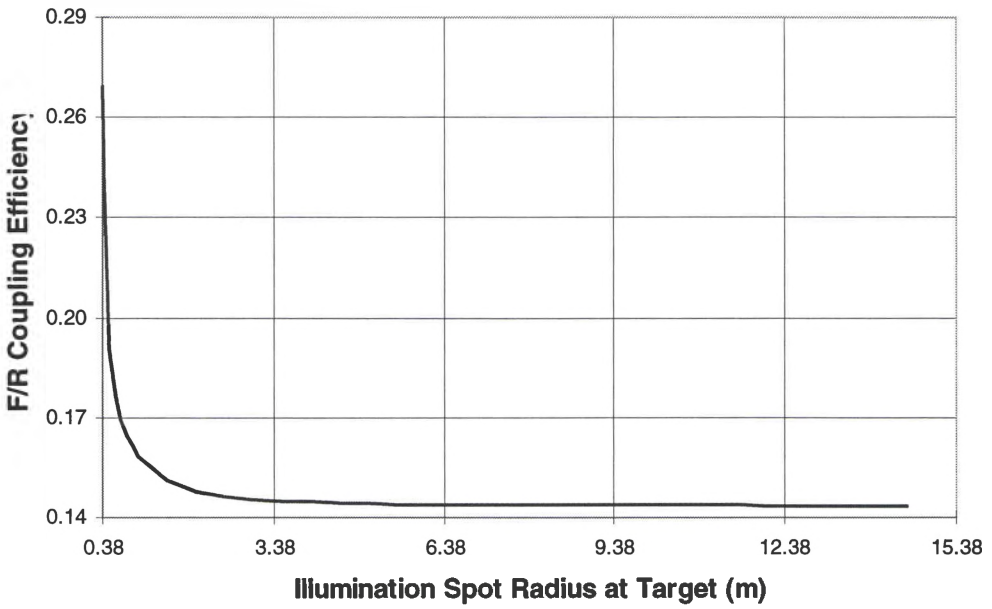

Figure 3.6: F/R coupling efficiency vs illumination spot radius on a 1 m target at a constant range of 20 km.

As we can see, $\eta_{F/R}$ decreases rapidly as the radius of the illumination beam approaches the radius the actual target, 0.5 m. Once past this boundary however, the target becomes unresolved and the rate of the curve's decent slows as the Gaussian illumination beam expands. Finally, the extent of the illumination beam becomes so large that the target is uniformly illuminated and the F/R coupling efficiency levels off at $\eta_{F/R}$~14.4% . This

observation leads us to conclude that after the target is completely illuminated, coupling efficiency becomes constant and any further beam expansion would only serve to decrease the overall system efficiency. In the next chapter, the idea of system efficiency is examined more carefully.

CHAPTER IV

System Efficiency Analysis

As seen in Chapter III, the $\eta_{F/R}$ coupling efficiency developed in the full analysis increased steadily as the target moves further and further away from the transmitter/receiver. From Figure 3.5, we saw that in some cases, such as for very small targets, this efficiency was very high, nearly 85%. Unfortunately with a smaller target, any increase in $\eta_{F/R}$ coupling efficiency is offset by a decrease in the amount of transmitted power reflected off of the target that is ultimately available for detection. Intuition tells us that the transmitted coupling efficiency $\eta_{F/T}$ will drop off dramatically as target range increases. This effect can be modeled by simply changing the denominator of Eq. (3-35) from the expected power collected by the receiver to the expected total power transmitted through lens l_2 of Figure 3.1. In this chapter, we will develop an expression for $\eta_{F/T}$. A baseline signal-to-noise ratio (SNR) analysis for both spot and flood illuminated targets in a direct detection ladar system will also be presented.

4.1 Transmitted Power Coupling Efficiency

To compute $\eta_{T/F}$ for a diffuse target, we must take the ratio of the power coupled into the LP_{01} mode of the fiber to the total power P_{Tx} transmitted through lens l_1. The

total power transmitted through l_1 can be found by taking the magnitude squared of the field given by Eq. (3-15) and integrating over the area of the transmitter, yielding the following expression for P_{Tx}

$$\begin{aligned} P_{Tx} &= \frac{2P_{Trans}}{\pi\omega_o^2}\iint_{A_{Trans}} d\bar{\rho}\left|\exp\left(-\frac{|\bar{\rho}|^2}{\omega_o^2}\right)\right|^2 \\ &= \frac{2P_{Trans}}{\pi\omega_o^2}\iint_{A_{Trans}} d\bar{\rho}\exp\left(-\frac{2|\bar{\rho}|^2}{\omega_o^2}\right) \end{aligned} \quad (4\text{-}1)$$

Extending the limits of integration over the transmitter plane out to infinity by substituting the transmitter aperture function $W_{Trans}(\bar{\rho})$, given by

$$W_{Trans}(\bar{\rho}) = \mathrm{circ}\left(\frac{\bar{\rho}}{D_{Trans}}\right) \equiv \begin{cases} 1, & |\bar{\rho}| \le \frac{D_{Trans}}{2} \\ 0, & |\bar{\rho}| > \frac{D_{Trans}}{2} \end{cases} \quad (4\text{-}2)$$

the total transmitted power becomes

$$P_{Tx} = \frac{2P_{Trans}D_{Trans}^2}{\pi\omega_o^2}\iint d\bar{\rho}\,\mathrm{circ}(\bar{\rho})\exp\left(-\frac{2D_{Trans}^2|\bar{\rho}|^2}{\omega_o^2}\right) \quad (4\text{-}3)$$

Note, the $d\bar{\rho}$ has been rescaled by D_{Trans}. Expressing the $d\bar{\rho}$ integral in polar coordinates, integration of Eq. (4-3) yields

$$\begin{aligned} P_{Tx} &= P_{Trans}\left[1-\exp\left(-\frac{D_{Trans}^2}{2\omega_o^2}\right)\right] \\ &= P_{Trans}\left[1-\exp\left(-\frac{R^2}{2}\right)\right] \end{aligned} \quad (4\text{-}4)$$

where R is the truncation ratio at the transmitter. However, recalling that we have assumed an optimum truncation ratio of R=4 at the transmitter, the power lost upon transmission through l_1 is negligible, causing the exponential term in Eq. (4-4) to vanish.

Thus, the expected total power transmitted through lens l_1 is simply P_{trans}. Dividing Eq. (3-29) by P_{trans}, $\eta_{F/T}$ becomes

$$\eta_{F/T} = \frac{E\left[\tilde{P}_{sig}\right]}{\tilde{P}_{Trans}} \cong \frac{128NT_o a^2 D_t^{\,2} D_R^{\,2}\pi}{L^2}\int_0^1 dr\, r \exp\left[-a^2 r^2\right]$$
$$\times \int_0^{\frac{1}{2}} dx_t \exp\left(-N\pi^2 D_t^2 x_t^{\,2}\right)\int_0^{\sqrt{\frac{1}{4}-x_t^2}} dy_t \exp\left(-N\pi^2 D_t^2 y_t^{\,2}\right)\cos\left(\frac{2\pi D_R D_t r y_t}{\lambda L}\right). \quad (4\text{-}5)$$
$$\times \int_0^{\frac{1}{2}\sqrt{1-r^2}} dx \exp\left(-4a^2 x^2\right)\int_0^{\sqrt{\frac{1}{4}-x^2}-\frac{r}{2}} dy \exp\left(-4a^2 y^2\right)\cos\left(\frac{2\pi D_R^{\,2} r y}{\lambda L}\right)$$

For purposes of illustration, we will now look at the special case of $\eta_{F/T}$ versus target range under the conditions that: 1) f_2 equals infinity, thus yielding the minimum illumination beam waist without actually focusing the beam itself; and, 2) the target diameter for all ranges less than 20 km is twice the illumination beam waist at 20 km . Using Eq. (47) with $z_{eff} = 0$ and $\omega_{eff} = D_{trans}/4 = 2.5$ cm, we find that our beam diameter (and thus our fixed target size) at a target range of 20 km is 76.5 cm. From Eq. (2-15), at the same range, we find the diffraction limited spot size of our receiver aperture (D_R = 10 cm) is 73.2 cm in diameter. Upon comparison, we see that under these conditions the illuminated portion of the target, regardless of range for $L \leq 20$ km, will always be slightly larger than the diffraction limited spot size of the receiver, and thus always yield a borderline multimode return. For this discussion, returns obtained under the above conditions will be defined as the return from one pixel in the target plane, and Figure 4.1 illustrates $\eta_{F/T}$ vs. target range under this scenario.

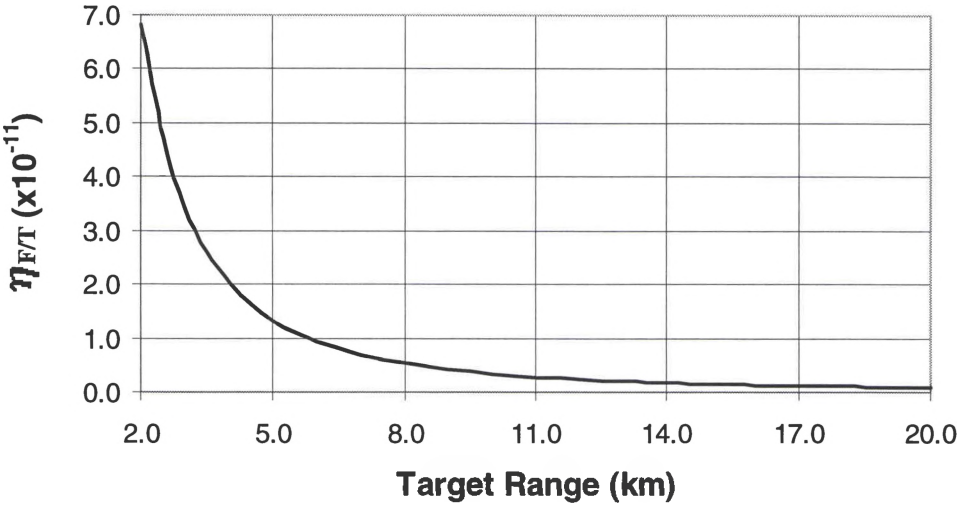

Figure 4.1: Transmitted power coupling efficiency ($\eta_{F/T}$) vs. target range for a resolved target with a nearly singlemode return.

Note, Figure 4.1 was generated using a receiver diameter of D_R = 10 cm and an N parameter calculated using a fiber core diameter of 8.3 μm and a normalized frequency parameter value of V = 2.26. Also, for purposes of illustration, we have assumed an arbitrary reflection coefficient of τ=0.5 thus, making $T_o = 0.5/\pi$. As we can see, Figure 4.1 exhibits a classic $1/e^2$ trend for an under filled object at most ranges. However, at close ranges of 4 km or less, this trend varies slightly as the cosine terms in Eq. (4-5) become more pronounced.

4.2 Signal To Noise Ratio Analysis

By itself, the significance of Figure 4.1 is not clearly obvious since the $\eta_{F/T}$ appears to be so small. However, expressing the data in terms of a baseline signal-to-noise ratio (SNR) that accounts for dark current noise, shot noise, and thermal noise gives

a better representation and puts the trend in a more appealing format. Writing our SNR expression in a form analogous to that of the SNR analysis developed by Overbeck *et al.* for a pulsed ladar system,[16] the post detection signal-to-noise ratio can be expressed as

$$SNR = \frac{\left(RJ_o\eta_{F/T}\right)^2}{T_1\left[2e\left(I_D + \frac{RJ_o\eta_{F/T}}{T_1}\right) + \frac{4k_bT}{R_L}\right]} \qquad (4\text{-}6)$$

where R is the responsivity of the detector, J_o is energy per pulse, T_1 is the pulse duration, e is the charge on an electron, and I_D is the dark current. Furthermore, k_b is Boltzmann's constant, R_L is the load resistance, and T is the temperature of the resistance in Kelvin. Assuming some reasonable values for the above constants such as R = 0.5 A/W, J_o = 100 mJ, T_1 = 3.5 nsec, I_D = 5 nA, T = 300 K, and R_L = 50 Ω, the signal-to-noise ratio vs. target range can be can be calculated using the appropriate values for the transmitted power coupling efficiency. Figure 4.2 illustrates the SNR vs. target range for a resolved target with a nearly singlemode return, one pixel wide and under the same conditions as Figure 4.1.

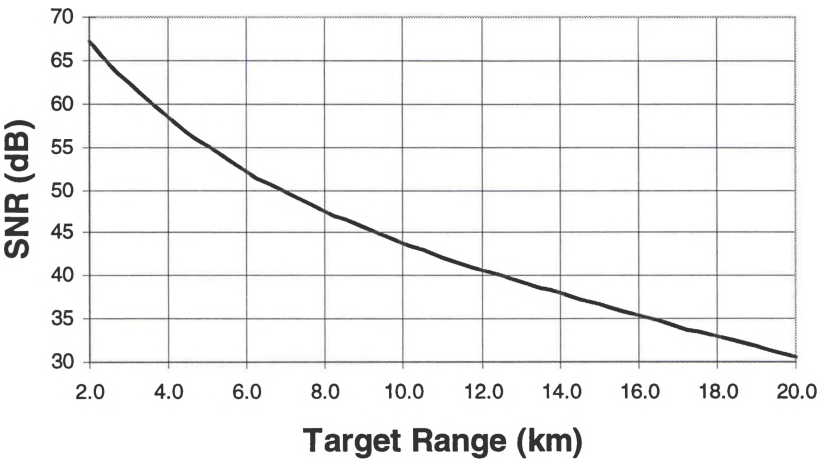

Figure 4.2: SNR vs. target range for a resolved target with a nearly singlemode return.

As can be seen, even though $\eta_{F/T}$ is very small, the coupled signal power is nearly eight hundred times greater than the noise, even at a range of 20 km due to the large pulse energy we have assumed.

However, expanding the beam to illuminate a larger target will greatly decrease the amount of energy density per pixel on the object. Since the above model gives $\eta_{F/T}$ for a single pixel in the target plane, the SNR for large targets can be roughly estimated by simply dividing the value of J_o by the total number of pixels in the expanded beam. For example, by assuming a large resolved target illuminated by a beam 15 m in diameter and a total pulse power of 100 mJ, the amount of power incident per pixel is reduced to approximately 0.260 mJ. The resulting effect on the SNR vs. target range is shown in Figure 4.3.

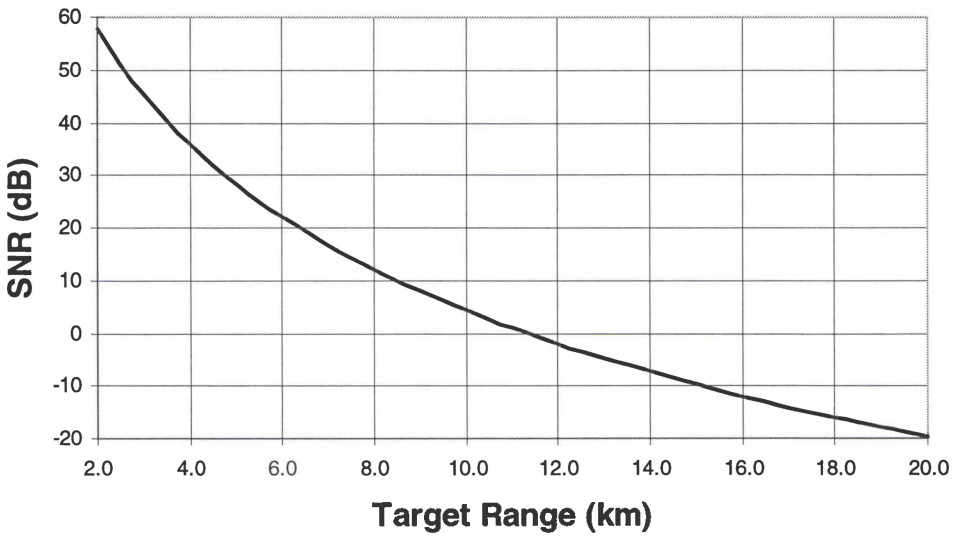

Figure 4.3: Signal-to-noise ratio (SNR) vs. target range for a multimode return, large resolved target. The beam diameter in the target plane has been set to 15 m.

Note, this estimate is a slight underestimate because it only accounts for the light reflected from the one pixel. In actuality, some of the scattered light from neighboring sectors will also be coupled into the fiber, increasing the effective energy incident on a pixel.

CHAPTER V

Glint Target Coupling Analysis

In this chapter, we will develop a theoretical model and calculate the F/R coupling efficiency for a circular glint target [i.e. a target that does not generate a random phase on the reflected wavefront]. This will then provide the baseline of comparison for the coupling efficiency enhancement simulations found in Chapter VI. Again, the same notation used in Chapter III will be employed, a boldface quantity will represent a complex field, an overscore will denote a vector quantity, and a tilde will indicate a random field. Also, $\overline{\rho}$, $\overline{\rho}_t$, $\overline{\rho}_R$, and $\overline{\rho}_f$ will still represent the two dimensional spatial variables associated with the transmitter, target, receiver, and fiber planes respectively.

5.1 Field Analysis for a Glint Target

To begin our analysis, we again start with the expression for the field at the fiber endface in a general illumination ladar system given by Eq. (3-6)

$$\tilde{\mathbf{U}}_f(\bar{\rho}_f) = \frac{\exp\left(ik\left(2L + f_3\right)\right)}{(i\lambda f_3)(\lambda L)^2} \iint_{A_t} d\bar{\rho}_t \, \tilde{T}(\bar{\rho}_t) \exp\left(\frac{i2\pi}{\lambda L}\left|\bar{\rho}_t\right|^2\right)$$
$$\times \iint_{A_{Trans}} d\bar{\rho} \, \mathbf{U}'_{Trans}(\bar{\rho}) \exp\left(-\frac{i2\pi}{\lambda L}\bar{\rho}\cdot\bar{\rho}_t\right) \qquad (5\text{-}1)$$
$$\times \iint d\bar{\rho}_R \, W_R(\bar{\rho}_R) \exp\left(\frac{i\pi}{\lambda L}\left|\bar{\rho}_R\right|^2\right) \exp\left(-i2\pi\bar{\rho}_R \cdot \left(\frac{\bar{\rho}_t}{\lambda L} + \frac{\bar{\rho}_f}{\lambda f_3}\right)\right)$$

Here, recall that $\mathbf{U}'_{Trans}(\bar{\rho})$ incorporates the phase curvature introduced by negative lens l_2 of Figure 3.1 and is defined by Eq. (3-7), λ is the source wavelength, k is the free space wavenumber, L is the distance to the target, and f_3 is the focal length of the coupling optic l_3. Again, we will assume the truncation of the transmitted beam is insignificant [i.e., R = 4]. As a result, the limits of integration over the A_{Trans} integral can be extended out to infinity, leaving the $d\bar{\rho}$ integral simply as the Fourier transform of Eq. (3-7). We can now determine the amount of power coupled into the LP_{01} mode of the fiber for a glint target.

The power $\bar{P}_{sig}$ coupled into the fundamental mode of the receiving fiber can again be approximated using the overlap integral of Eq. (2-6), following the same procedure as developed in Chapter III. However, by letting the entire phase across the target be zero, our target effectively becomes a "mirror" with reflectivity T_g. Then assuming that the object has no structure to it, the complex target reflectivity $\tilde{T}(\bar{\rho}_t)$ then becomes a constant which can be pulled out of the $d\bar{\rho}_t$ integral. Therefore, the steps associated with taking the expectation of signal power coupled into the LP_{01} mode of the fiber are no longer necessary. Making the appropriate substitutions back into Eq. (2-6), the signal power coupled into the fiber can be expressed as,

$$P_{sig,glint} \cong \frac{T_g^2}{(\lambda f_3)^2(\lambda L)^4}\left|\iint_{A_t} d\bar{\rho}_t \exp\left(\frac{i2\pi}{\lambda L}|\bar{\rho}_t|^2\right)\mathcal{U}'_{Trans}\left(\frac{\bar{\rho}_t}{\lambda L}\right) \iint d\bar{\rho}_f U^*_{01}(\bar{\rho}_f)\right.$$
$$\left.\times\iint d\bar{\rho}_R W_R(\bar{\rho}_R)\exp\left(\frac{i\pi}{\lambda L}|\bar{\rho}_R|^2\right)\exp\left(-i2\pi\bar{\rho}_R\cdot\left(\frac{\bar{\rho}_t}{\lambda L}+\frac{\bar{\rho}_f}{\lambda f_3}\right)\right)\right|^2 , \quad (5\text{-}2)$$

where $\mathcal{U}'_{trans}$ is the Fourier transform of transmitted field. Simplifying, we then arrive at the following expression after some straightforward rearrangement of the exponential terms,

$$P_{sig,glint} \cong \frac{T_g^2}{(\lambda f_3)^2(\lambda L)^4}\left|\iint_{A_t} d\bar{\rho}_t \exp\left(\frac{i2\pi}{\lambda L}|\bar{\rho}_t|^2\right)\mathcal{U}'_{Trans}\left(\frac{\bar{\rho}_t}{\lambda L}\right)\right.$$
$$\left.\times\iint d\bar{\rho}_R \mathcal{U}^*_{01}\left(\frac{\bar{\rho}_R}{\lambda f_3}\right)W_R(\bar{\rho}_R)\exp\left(\frac{i\pi}{\lambda L}|\bar{\rho}_R|^2\right)\exp\left(\frac{-i2\pi}{\lambda L}\bar{\rho}_R\cdot\bar{\rho}_t\right)\right|^2 , \quad (5\text{-}3)$$

where $\mathcal{U}^*_{01}$ is the Fourier transform of LP_{01} mode of the fiber.

To continue with the analysis, we must define the information about the transmitted beam, the aperture functions W_t and W_R, and the modal field in the fiber. For consistency, we will let the field transmitted through the negative lens l_2 be given by Eq. (3-16). For inclusion in Eq. (5-3), the Fourier transform of the transmitted field $\mathcal{U}'_{Trans}$ can be found by substituting Eq. (3-19) into Eq. (3-17) to give

$$\mathcal{U}'_{Trans}\left(\frac{\bar{\rho}_t}{\lambda L}\right) = \frac{\sqrt{8\pi P_{Trans}\omega_o^2 f_2^2}}{(2f_2)^2 + k^2\omega_o^4}\left(2f_2 + ik\omega_o^2\right)$$
$$\times\exp\left[\frac{-\pi^2\left(2f_2 + ik\omega_o^2\right)}{(\lambda L)^2}\left(\frac{2f_2\omega_o^2}{(2f_2)^2 + k^2\omega_o^4}\right)|\bar{\rho}_t|^2\right] . \quad (5\text{-}4)$$

The $d\bar{\rho}_t$ integral in Eq. (5-3) then becomes an integral over a circular target area $W_t(\bar{\rho}_t)$ of the complicated field in Eq. (5-4) multiplied by a quadratic phase factor. Recalling that

the field distribution of the fiber mode is given by Eq. (2-7), substitution of Eqs. (2-7) and (5-4) back into Eq. (5-3) results in the following expression for $P_{sig,glint}$

$$P_{sig,glint} \cong \frac{T_g^2}{(\lambda f_3)^2(\lambda L)^4}\left|\frac{\sqrt{16\pi^2 P_{Trans}\omega_o^2 f_2^2 \omega^2}}{(2f_2)^2 + k^2\omega_o^4}\left(2f_2 + ik\omega_o^2\right)\right|^2$$
$$\times\left|\iint_{A_t} d\bar{\rho}_t \exp\left[\frac{-\pi^2(2f_2)}{(\lambda L)^2}\left(\frac{2f_2\omega_o^2}{(2f_2)^2 + k^2\omega_o^4}\right)|\bar{\rho}_t|^2\right]\right.$$
$$\times\exp\left[-\left(\frac{i2\pi^2 f_2\omega_o^4}{(\lambda L)^2\left((2f_2)^2 + k^2\omega_o^4\right)} + \frac{i2\pi}{\lambda L}\right)|\bar{\rho}_t|^2\right] \qquad (5\text{-}5)$$
$$\left.\times\iint d\bar{\rho}_R W_R(\bar{\rho}_R)\exp\left(\frac{i\pi}{\lambda L}|\bar{\rho}_R|^2\right)\exp\left(\frac{i2\pi}{\lambda L}\bar{\rho}_R\cdot\bar{\rho}_t\right)\exp\left(\frac{\pi\omega^2}{\lambda f_3}|\bar{\rho}_R|^2\right)\right|^2$$

The $d\bar{\rho}_t$ integral in Eq. (5-5) can be evaluated by first defining a specific target area function $W_t(\bar{\rho})$ of Eq. (3-21) and extending the bounds of the integral out to infinity. Employing this technique and letting the receiver aperture function $W_R(\bar{\rho})$ be given by Eq. (3-22), we see that after the appropriate substitutions, Eq. (5-5) can be rearranged to obtain the following,

$$P_{sig,glint} \cong \frac{4BP_{Trans}\omega^2 T_g^2}{(\lambda f_3)^2(\lambda L)^2}\left|\iint d\bar{\rho}_t \exp\left[-B|\bar{\rho}_t|^2\right]\right.$$
$$\times\exp\left[-i\left(\frac{Bk\omega_o^2}{2f_2} + \frac{2\pi}{\lambda L}\right)|\bar{\rho}_t|^2\right]\mathrm{circ}\left(\frac{\bar{\rho}_t}{d_t}\right) \qquad (5\text{-}6)$$
$$\left.\times\iint d\bar{\rho}_R \mathrm{circ}\left(\frac{\bar{\rho}_R}{D_R}\right)\exp\left[-\left(\left(\frac{\pi\omega}{\lambda f_3}\right)^2 - \frac{i\pi}{\lambda L}\right)|\bar{\rho}_R|^2\right]\exp\left(\frac{i2\pi}{\lambda L}\bar{\rho}_R\cdot\bar{\rho}_t\right)\right|^2$$

where B is defined as

$$B \equiv \frac{4\pi^2 f_2^2 \omega_o^2}{(\lambda L)^2\left(4f_2^2 + \left(k\omega_o^2\right)^2\right)} \tag{5-7}$$

Equation (5-6) is the most general expression one can obtain for the signal power reflected off of a glint target and coupled into an optical fiber receiver in a general illumination ladar system. From this point, one can analyze any combination of resolved or unresolved circular targets with a singlemode or a multimode return. A complete derivation for the most complicated case of an unresolved glint target with a multimode return can be found in Appendix A. However, for simplicity of calculation, we will only examine here the special case of a resolved target [i.e. f_2 has gone to infinity] with a singlemode return [i.e. the illuminated portion of the target is smaller than the diffraction limited spot size of the receiver]. This allows us to greatly simplify the mathematics involved with solving the problem and directly compare our results to the earlier work of Jacob *et. al.*[2]

Assuming a resolved target implies that the $d\bar{\rho}_t$ integral in Eq. (5-5) is performed over all space, not just over the target's area itself. With this in mind, the step of defining a specific target function $W_t(\bar{\rho})$ is unnecessary, and thus we can eliminate the circ function over the target area in Eq. (5-6). Furthermore, by letting f_2 go to infinity, L'Hopital's Rule can be employed, thus collapsing the B constant to,[11]

$$B \Rightarrow \left(\frac{\pi\omega_o}{\lambda L}\right)^2 , \tag{5-8}$$

and reducing $\mathcal{U}'_{Trans}$ to

$$\mathcal{U}'_{Trans}\left(\frac{\bar{\rho}_t}{\lambda L}\right) = \sqrt{P_{Trans}\,2\pi\omega_o^2}\,\exp\left[-\left(\frac{\pi\omega_o}{\lambda L}\right)^2 |\bar{\rho}_t|^2\right] \quad . \tag{5-9}$$

As a result, this reduces the first quadratic term in the $d\bar{\rho}_t$ integral to a much simpler expression and causes the second quadratic term to vanish altogether. Moreover, allowing f_2 to go to infinity ensures that the illuminated portion of the target will always be smaller that the diffraction limited spot size of the receiver for all target ranges and thus, always generate a singlemode return. After these simplifications, the resulting expression for Eq. (5-6) can be written as,

$$P_{sig,glint} \cong \frac{4\pi^2 P_{Trans}\omega^2\omega_o^2 T_g^2}{(\lambda f_3)^2(\lambda L)^4}\left|\iint d\bar{\rho}_t \exp\left[-\left(\frac{\pi\omega_o}{\lambda L}\right)^2|\bar{\rho}_t|^2\right]\exp\left[i\left(\frac{2\pi}{\lambda L}\right)|\bar{\rho}_t|^2\right]\right.$$
$$\left.\times\iint d\bar{\rho}_R\,\mathrm{circ}\left(\frac{\bar{\rho}_R}{D_R}\right)\exp\left[-\left(\left(\frac{\pi\omega}{\lambda f_3}\right)^2 - \frac{i\pi}{\lambda L}\right)|\bar{\rho}_R|^2\right]\exp\left(\frac{i2\pi}{\lambda L}\bar{\rho}_R\cdot\bar{\rho}_t\right)\right|^2 \quad . \tag{5-10}$$

Upon inspection of Eq. (5-10), one easily recognizes that with a little rearrangement, the $d\bar{\rho}_t$ integral merely becomes the Fourier transform of the two $\bar{\rho}_t$ exponentials. Carrying out this step yields,

$$P_{sig,glint} \cong \frac{4\pi^2 P_{Trans}\omega^2\omega_o^2 T_g^2}{(\lambda f_3)^2(\lambda L)^4}\left|\iint d\bar{\rho}_R\,\mathrm{circ}\left(\frac{\bar{\rho}_R}{D_R}\right)\exp\left[-\left(\left(\frac{\pi\omega}{\lambda f_3}\right)^2 - \frac{i\pi}{\lambda L}\right)|\bar{\rho}_R|^2\right]\right.$$
$$\left.\times\mathcal{F}^{-1}\left\{\exp\left[-\left(\frac{\pi\omega_o}{\lambda L}\right)^2|\bar{\rho}_t|^2\right]\exp\left[i\left(\frac{2\pi}{\lambda L}\right)|\bar{\rho}_t|^2\right]\Big|_{\bar{\rho}_t=\frac{\bar{\rho}_R}{\lambda L}}\right\}\right|^2 \quad . \tag{5-11}$$

To evaluate this transform kernel, we begin with a slight rearrangement of terms,

$$\mathcal{F}^{-1}\left\{\exp\left[-\left(\frac{\pi\omega_o}{\lambda L}\right)^2|\bar{\rho}_t|^2\right]\exp\left[i\left(\frac{2\pi}{\lambda L}\right)|\bar{\rho}_t|^2\right]\Bigg|_{\bar{\rho}_t=\frac{\bar{\rho}_R}{\lambda L}}\right\}$$
$$=\mathcal{F}^{-1}\left\{\exp\left[-\pi^2\left(i\left(\frac{-2}{\pi\lambda L}\right)+\left(\frac{\omega_o}{\lambda L}\right)^2\right)|\bar{\rho}_t|^2\right]\Bigg|_{\bar{\rho}_t=\frac{\bar{\rho}_R}{\lambda L}}\right\} \quad (5\text{-}12)$$

Now, letting a_2 equal

$$a_2 = i\left(\frac{-2}{\pi\lambda L}\right)+\left(\frac{\omega_o}{\lambda L}\right)^2 , \quad (5\text{-}13)$$

Eq. (5-12) simply becomes the Fourier transform of a standard Gaussian function and can be readily calculated to give

$$\mathcal{F}^{-1}\left\{\exp\left[-\left(\frac{\pi\omega_o}{\lambda L}\right)^2|\bar{\rho}_t|^2\right]\exp\left[i\left(\frac{2\pi}{\lambda L}\right)|\bar{\rho}_t|^2\right]\Bigg|_{\bar{\rho}_t=\frac{\bar{\rho}_R}{\lambda L}}\right\}$$
$$=\mathcal{F}^{-1}\left\{\exp\left[-\pi^2 a_2|\bar{\rho}_t|^2\right]\Big|_{\bar{\rho}_t=\frac{\bar{\rho}_R}{\lambda L}}\right\} \quad (5\text{-}14)$$
$$=\frac{1}{a_2}\exp\left[\frac{-1}{a_2(\lambda L)^2}|\bar{\rho}_R|^2\right]$$

Rationalizing the denominator gives us the following expression for the transform kernel in Eq. (5-11),

$$\frac{1}{a_2}\exp\left[\frac{-1}{a_2(\lambda L)^2}|\bar{\rho}_R|^2\right]=\frac{(\lambda L)^2(\omega_o^2\pi+i2\lambda L)}{(\omega_o^2\pi)^2+(2\lambda L)^2}\exp\left[-\frac{\pi(\omega_o^2\pi+i2\lambda L)}{(\omega_o^2\pi)^2+(2\lambda L)^2}|\bar{\rho}_R|^2\right] . \quad (5\text{-}15)$$

Equation (5-15) can now be substituted back into Eq. (5-11) to obtain,

$$P_{sig,glint} \cong \frac{4\pi B_2 P_{Trans}\omega^2 T_g^2}{(\lambda f_3)^2}\left|\iint d\bar{\rho}_R \exp\left[-\left(\frac{\pi\omega}{\lambda f_3}\right)^2|\bar{\rho}_R|^2\right]\exp\left[-\pi B_2\,|\bar{\rho}_R|^2\right]\right.$$
$$\left.\times\exp\left[\frac{i\pi}{\lambda L}|\bar{\rho}_R|^2\right]\exp\left[\frac{i2B_2\lambda L}{\omega_o^2}|\bar{\rho}_R|^2\right]\mathrm{circ}\left(\frac{\bar{\rho}_R}{D_R}\right)\right|^2 , \quad (5\text{-}16)$$

where

$$B_2 \equiv \frac{\omega_o^2\pi}{(\omega_o^2\pi)^2 + (2\lambda L)^2} . \quad (5\text{-}17)$$

Once again, we notice that Eq. (5-16) is an integral over all space of a circ function weighted by four exponential terms. Equation (5-16) then becomes, after scaling the $d\bar{\rho}_R$ variable of integration by D_R,

$$P_{sig,glint} \cong \frac{4\pi B_2 P_{Trans}\omega^2 D_R^4 T_g^2}{(\lambda f_3)^2}\left|\iint d\bar{\rho}_R \exp\left[-D_R^2\left(\left(\frac{\pi\omega}{\lambda f_3}\right)^2 + \pi B_2\right)|\bar{\rho}_R|^2\right]\right.$$
$$\left.\times\exp\left[iD_R^2\left(\frac{2B_2\lambda L}{\omega_o^2} + \frac{\pi}{\lambda L}\right)|\bar{\rho}_R|^2\right]\mathrm{circ}(\bar{\rho}_R)\right|^2 . \quad (5\text{-}18)$$

Expressing the $d\bar{\rho}_R$ integral in polar coordinates and using the circ functions to define the bounds over the receiver area, the coupled signal power for a resolved glint target with a single mode return is,

$$P_{sig,glint} \cong \frac{16\pi^3 B_2 P_{Trans}\omega^2 D_R^4 T_g^2}{(\lambda f_3)^2}\left|\int_0^{\frac{1}{2}} dr\, r \exp\left[-D_R^2 r^2\left(\left(\frac{\pi\omega}{\lambda f_3}\right)^2 + \pi B_2\right)\right]\right.$$
$$\left.\times\exp\left[iD_R^2 r^2\left(\frac{2B_2\lambda L}{\omega_o^2} + \frac{\pi}{\lambda L}\right)\right]\right|^2 . \quad (5\text{-}19)$$

Now to compute $\eta_{F/R}$ for a glint target, we need to take the ratio of the power coupled into the LP_{01} mode of the fiber to the total power collected by the receiver aperture. Therefore, we must determine the nature of the field at the receiver and

determine how much energy is actually collected. From Eqs. (3-1), (3-2), and (3-3), we can show that the field at the receiver plane is given by

$$\tilde{U}_R(\bar{\rho}_R) = \frac{\exp(i2kL)}{(i\lambda f_3)(\lambda L)^2}\iint_{A_t} d\bar{\rho}_t \tilde{T}(\bar{\rho}_t)\exp\left(\frac{ik}{2L}\left(|\bar{\rho}_t|^2 + |\bar{\rho}_R|^2 - 2\bar{\rho}_t\cdot\bar{\rho}_R\right)\right) \times \iint_{A_{Trans}} d\bar{\rho} U_{Trans}(\bar{\rho})\exp\left(\frac{ik}{2f_2}|\bar{\rho}|^2\right)\exp\left(\frac{ik}{2L}\left(|\bar{\rho}_t|^2 - 2\bar{\rho}\cdot\bar{\rho}_t\right)\right) \quad , \quad (5\text{-}20)$$

if the assumption of $A_{Trans} << \lambda L$ is made. The total irradiance $I_{R,glint}$ at the receiver plane is then simply the magnitude squared of $\tilde{U}_R$. Given that the transmitted beam is untruncated and that we are looking at a resolved glint target [i.e. $\tilde{T}(\bar{\rho}_t) = T_g$ and f_2 has gone to infinity], the bounds on the A_t integral can be extended to infinity. With the simplifications, the irradiance can be written as

$$I_{R,glint} = \frac{T_g}{(\lambda L)^4}\left|\iint d\bar{\rho}_t \exp\left(\frac{i2\pi}{\lambda L}|\bar{\rho}_t|^2\right)\exp\left(-\frac{i2\pi}{\lambda L}\bar{\rho}_R\cdot\bar{\rho}_t\right)\mathcal{U}'_{Trans}\left(\frac{\bar{\rho}_t}{\lambda L}\right)\right|^2 \quad , \quad (5\text{-}21)$$

where $\mathcal{U}'_{Trans}$ is the Fourier transform of transmitted field in Eq. (5-9). Substituting the transform of transmitted field back into Eq. (5-21) above gives an integral identical to the Fourier transform kernel of Eq. (5-11). Thus, using the result of Eq. (5-15), the irradiance at the receiver aperture is given by

$$\begin{aligned} I_{R,glint} &= 2B_2 P_{Trans} T_g^2 \left|\exp\left[\frac{i2B_2\lambda L}{\omega_o^2}|\bar{\rho}_R|^2\right]\exp\left[-\pi B_2 |\bar{\rho}_R|^2\right]\right|^2 \\ &= 2B_2 P_{Trans} T_g^2 \exp\left[-2\pi B_2 |\bar{\rho}_R|^2\right] \end{aligned} \quad , \quad (5\text{-}22)$$

where B_2 is given by Eq. (5-17).

The above expression is then the irradiance across the receiver plane, however, the total power received will be limited by the finite extent of the receiver aperture.

Therefore, the power received for coupling into the fiber can be found by integrating the result of Eq. (5-22) over the area of the receiver to obtain

$$P_{R,glint} = 2B_2 P_{Trans} T_g^2 \iint_{A_R} d\overline{\rho}_R \exp\left[-2\pi B_2 \left|\overline{\rho}_R\right|^2\right] \quad . \tag{5-23}$$

Extending the limits of integration over the receiver plane out to infinity by substituting the receiver aperture function $W_R(\overline{\rho})$ of Eq. (3-21) into Eq. (5-23), the total collected power becomes

$$P_{R,glint} = 2B_2 P_{Trans} T_g^2 \iint d\overline{\rho}_R \, circ\left(\frac{\overline{\rho}_R}{D_R}\right) \exp\left[-2\pi B_2 \left|\overline{\rho}_R\right|^2\right] \quad . \tag{5-24}$$

The total power at the receiver can readily be found by scaling the $d\overline{\rho}_R$ variable of integration by D_R and rewriting the entire integral in polar coordinates. Performing these operations gives us the following expression for the received power

$$\begin{aligned} P_{R,glint} &= 4\pi B_2 P_{Trans} D_R^2 T_g^2 \int_0^{\frac{1}{2}} dr \, r \exp\left[-2\pi B_2 D_R^2 r^2\right] \\ &= P_{Trans} T_g^2 \left[1 - \exp\left(-\frac{\pi B_2 D_R^2}{2}\right)\right] \end{aligned} \quad . \tag{5-25}$$

Finally, dividing Eq. (5-19) by Eq. (5-25), we obtain the final expression for $\eta_{F/R}$ for glint target analyzed by a general illumination ladar system incorporating a single mode optical fiber receiver. This equation, expressed in terms of the truncation ratio at the transmitter R, is given by

$$\begin{aligned} \eta_{F/R,glint} \cong \frac{32\pi a^2 D_R^2}{1 - \exp\left[-\frac{\pi D_R^2 B_2}{2}\right]} \Bigg| \int_0^{\frac{1}{2}} dr \, r \exp\left[-D_R^2 r^2 \left(2a^2 + \pi B_2\right)\right] \\ \times \cos\left[r^2 D_R^2 \left(\frac{2B_2 \lambda L}{\omega_o^2} + \frac{\pi}{\lambda L}\right)\right] \Bigg|^2 \end{aligned} \quad , \tag{5-26}$$

where the "a" parameter is given by Eq. (3-25).

Equation (5-26) can now readily be compared to the coupling efficiency expression in Eq. (3-35) for diffuse resolved target with a single mode return, by letting f_2 in the N parameter of Eq. (3-24) go to infinity. After some manipulation, this gives us the following expression

$$\eta_{F/R,diffuse} = \frac{E\left[\tilde{P}_{sig}\right]}{E\left[\tilde{P}\right]} \cong \frac{128a^2}{\pi}\int_0^1 dr \exp\left[-\left(\frac{1}{2}R^2 + a^2\right)r^2\right] r$$
$$\times \int_0^{\frac{1}{2}\sqrt{1-r^2}} dx \exp\left(-4a^2x^2\right) \qquad (5\text{-}27)$$
$$\times \int_0^{\sqrt{\frac{1}{4}-x^2}-\frac{r}{2}} dy \exp\left(-4a^2y^2\right)\cos\left(\frac{2\pi D_R{}^2 ry}{\lambda L}\right)$$

where the beam at the transmitter has already been assumed to be untruncated. Upon inspection of Eq. (5-27), one soon notices that it is slightly different from Eq. (31) found in Reference 2. Although both presentations of $\eta_{F/R,diffuse}$ contain mostly the same components, the dy integral in Eq. (5-27) above has been altered to account for several false assumptions made during Jacob's original analysis. A complete derivation of Eq. (5-27) and a full explanation of where each corrective term arises from can be found in Appendix B.

The optical fiber receiver we will be coupling into is again the Corning SMF-28 fiber with a core diameter of 8.3 μm and a NA of 0.13. Yet, unlike in earlier models where this fiber was used with an illumination wavelength of 1.5 μm [i.e. the geometric model and full analysis], we will now switch to a wavelength of 1.064 μm. This change in wavelength will enable us to use the pre-calibrated phase vs. voltage curves developed by Missy[15] for a particular liquid crystal spatial light modulator (LCSLM) device that will

be used in Chapters VI and VII for the phase filtering experiments. Although we will not go into the specifics of exactly how the LCSLM will be used at this time, it is necessary to motivate the reason for changing the operating wavelength.

When changing the operating wavelength of the system, however, care must be taken to make sure that the optical fiber still behaves as a singlemode fiber. Using Eq. (2-9), the V number at 1.064 μm for this fiber can be readily determined to be 3.184. Then employing the classical table developed by Gloge for the normalized propagation parameter b vs. V number in weakly guiding fibers,[17] our fiber at this wavelength corresponds to a slightly multimode fiber where both the LP_{01} and LP_{11} modes are present.

Applying the computational techniques developed by Jacob,[2] an expression for the power coupled into a multimode fiber receiver can easily be obtained for a glint target with a multimode return. Note, since both the x and y polarization states of the LP_{11} have the same mode profile, they will be treated as one mode throughout the remainder of this argument. With two modes propagating down the fiber, P_{sig} is now the magnitude squared of the overlap between the field at the fiber endface and both the LP_{01} and LP_{11} fiber modes. Thus, Eq. (2-6) becomes

$$\tilde{P}_{sig} \approx \left| \iint d\bar{\rho}_f \, \tilde{U}_f(\bar{\rho}_f) \, U_{01}^*(\bar{\rho}_f) + \iint d\bar{\rho}_f \, \tilde{U}_f(\bar{\rho}_f) \, U_{11}^*(\bar{\rho}_f) \right|^2 \quad . \tag{5-28}$$

This equation can be greatly simplified by examining the LP_{11} mode a bit more carefully. Unlike the LP_{01} mode which can be approximated with a Gaussian profile, the LP_{11} modal field is the odd function[10] displayed in Figure 5.1.

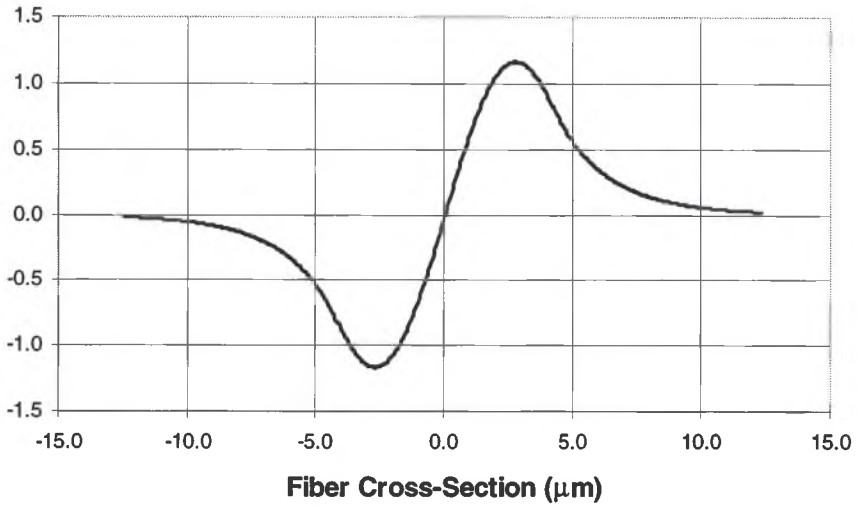

Figure 5.1: LP_{11} modal field in an optical fiber.

Substituting the expression for the field at the fiber endface given by Eq. (5-1) and recalling that $\tilde{\mathbf{T}}(\bar{\rho}_t) = T_g$ for a glint target, the contribution of the second half of Eq. (5-28) to P_{sig} can be quickly determined. By inspection, we see that this portion of the coupled signal power becomes the overlap integral between the even function $\tilde{\mathbf{U}}_f(\bar{\rho}_f)$ and the odd function of the LP_{11} modal field. Extending the limits on the integral out to infinity by defining a fiber receiver aperture function, the area resulting from this field overlap will be equal to zero, leaving us with the same identical expression for P_{sig} developed earlier. Therefore, even though the Corning SMF-28 fiber is slightly multimode at 1.064 μm, the LP_{11} modes will not be excited by the return from a glint target, allowing us to treat the fiber as singlemode.

For the diffuse case though, this will not be the case. Due to the diffuse nature of the target, the second double integral in Eq. (5-28) will no longer be zero. To properly evaluate this expression for P_{sig}, we must expand the magnitude squared and take the

expectation of each of the resulting terms as in Chapter III. As one can imagine, this process quickly becomes very complicated. Therefore, for simplicity and because it will be the most dominant term of the two, we will merely focus on the P_{sig} power coupled into the LP_{01} mode of the fiber. This simplification also allows us to use Eq. (5-27) to theoretically model the F/R coupling efficiency for a resolved, diffuse target with a single mode return. However, it is important to note that if these results were verified experimentally, the actual coupling efficiency measured would be higher than predicted due to the coupling into the second fiber mode.

With these issues in mind, one can determine the maximum F/R coupling efficiency for a glint target in the far field by letting L→infinity in Eqs. (5-10) and (5-21). As a result, all complex exponential terms drop out of each expression and upon evaluation of the remaining terms, we can obtain the following relationship,

$$\eta_{F/R} = \frac{4}{a^2}\left[1 - \exp\left(-\frac{a^2}{2}\right)\right] \quad , \qquad (5\text{-}29)$$

where "a" is given by Eq. (3-25). We can now make a direct comparison between Eqs. (5-26), (5-27), and (5-29). First, we assume an optimum truncation ratio of R=4 and a transmitter diameter of D_{Trans}=10 cm. Thus, a transmitted beam diameter ω_o can be readily calculated to be 2.5 cm for inclusion in the B_2 constant. Then, letting the distance to the target L equal 20 km, the wavelength λ equal 1.064 μm, and the diameter of the receiver equal 10 cm, both equations can be plotted vs. the "a" parameter again given in Eq. (3-25). This particular plot is shown in Figure 5.2 below.

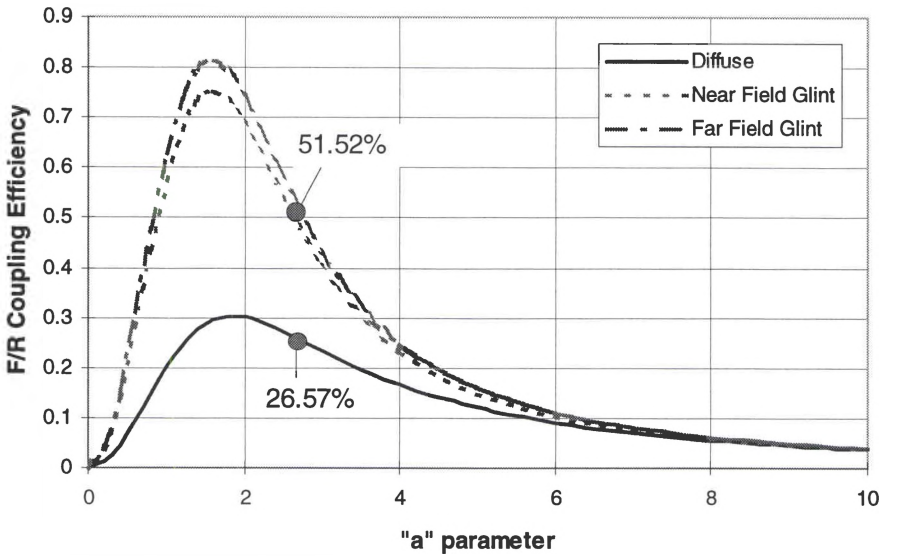

Figure 5.2: Receiver/fiber coupling efficiency vs. the "a" parameter for a diffuse and a glint target in the near field, as well as a glint target in the far field. Each target is resolved and has a singlemode return. Range to the diffuse and glint targets in the near field is 20 km.

Note, a value for $\eta_{F/R}$ has been singled out on each of the curves in Figure 5.2 at "a"= 2.58. These coupling efficiencies will be compared to the computer simulations of Chapter VI, for a fiber 8.3 μm in diameter, for any coupling efficiency enhancement resulting from phase only filtering with a liquid crystal beam steerer.

As expected, the F/R coupling efficiency for a glint target is much higher than that of an identical diffuse target when the numerical apertures of the fiber receiver and the coupling optics are closely matched to each other. From Figure 5.2, when the "a" parameter is equal to 1.84 and both coupling efficiencies are near their maximums with the $\eta_{F/R}$ for the glint target being more than twice as great as the $\eta_{F/R}$ of the diffuse target ($\eta_{F/R,glint}$ = 73.39% vs. $\eta_{F/R,diffuse}$ = 30.32%). This dramatic difference results from different nature of the two targets. By definition, the surface variations across a diffuse

target will cause the reflected light off the target to scatter over a much larger area of space leading to more interference in the wavefront across the plane of the fiber. Therefore, less collected light falls within the acceptance cone of the optical fiber, giving a lower coupling efficiency for the diffuse target. On the other hand, the return from the smoother, glint target does not experience this effect nearly as much and the field at the fiber has a greater F/R coupling efficiency. One also notices that a maximum coupling of 81.5% can be obtained for a glint target in the far field, thus setting an upper limit for F/R coupling efficiency.

CHAPTER VI

Coupling Efficiency Enhancement with Phase Only Filtering for Singlemode Glint and Diffuse Targets

In Chapter V, expressions for the F/R coupling efficiency were developed for a glint target. From Figure 5.2, we saw that the coupling efficiency of singlemode returns from resolved, diffuse targets was nearly half that of an identical glint target in a NA matched, general illumination ladar system. With this $\eta_{F/R}$ trend between glint and diffuse targets in mind, we will now investigate the prospect of enhancing the coupling efficiency by phase only filtering the singlemode return from a target with a liquid crystal spatial light modulator.

In this chapter, we will present a computer simulation technique capable of predicting a corrective, phase filter across the receiver aperture for a resolved, glint target with a singlemode return. Once this phase profile is known, we will apply it to the return signal with a liquid crystal spatial light modulator LCSLM, recalculate the F/R coupling efficiency. Once these routines are established, we will investigate the F/R coupling efficiency for a specific example of a circular target with a singlemode return and compare it to the baseline glint coupling efficiency in Figure 5.2 for any enhancement. Then we will use the same phase mask generated for the glint target to filter the return

signal from a diffuse target. The resulting values for diffuse F/R coupling efficiency will also be compared to the data in Chapter V with and without the phasemask across the device.

6.1 Gerchberg-Saxton Algorithm

Although there are several error reduction algorithms available today capable of minimizing the difference or error between two functions,[18] one of the most widely accepted is the Gerchberg-Saxton algorithm. First developed in 1971, the Gerchberg-Saxton algorithm is an iterative process that allows one to find an ideal phase filter that converts a known intensity pattern in the diffraction plane into a desired pattern in the imaging plane.[19] This phase filter is found by substituting the modulus of the diffraction pattern to the modulus of the desired image pattern at each individual step in the algorithm. However, while matching the two moduli of the fields, the phase is left to vary freely until the error between the two patterns is minimized [i.e. a stable solution is reached].

We will now apply this process to the receiver end of our direct detection ladar system. To allow for phase filtering of the return signal collected by the receiver, the LCSLM is inserted into the return path of the laser radar system, as shown in Figure 6.1,

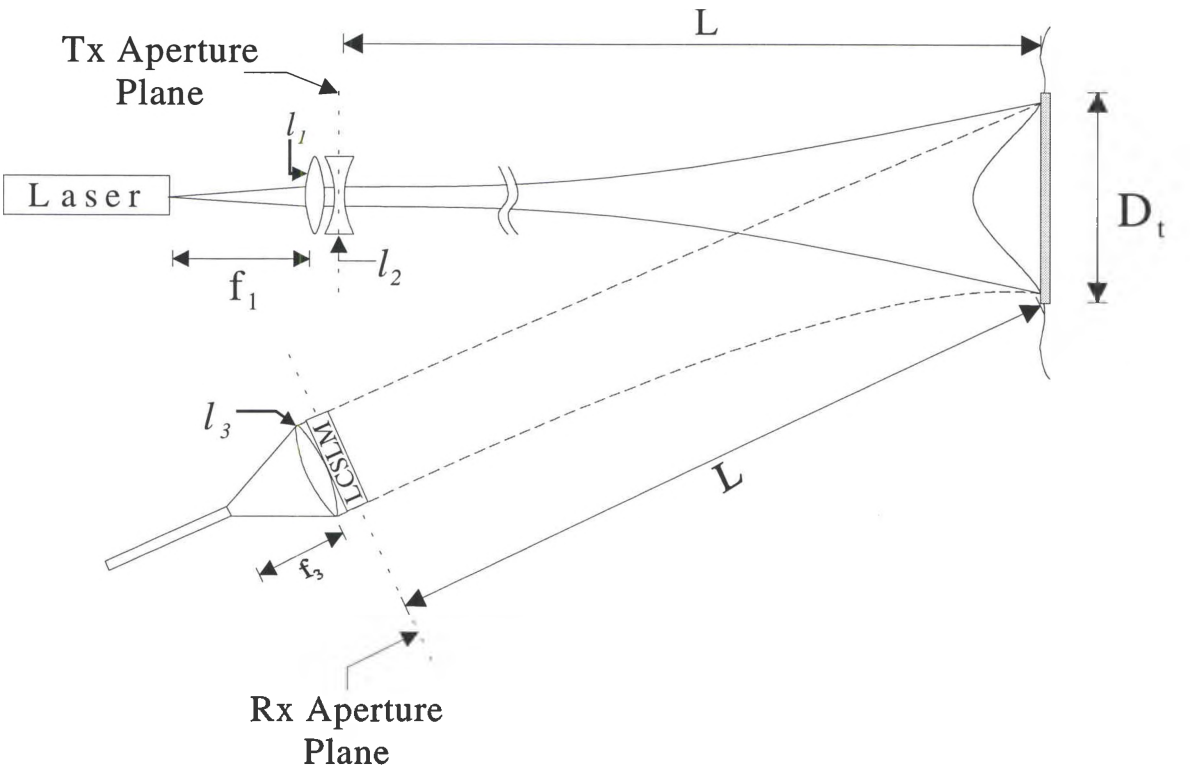

Figure 6.1: Modified laser radar system with a liquid crystal spatial modulator (LCSLM) in the receiver.

where all of the other variables in the above figure are the same as in Figure 3.1. Also notice that l_3 is no longer in the receiver aperture plane, but is merely a Fourier transform lens positioned between the liquid crystal device in the receiver plane and the fiber endface. It is important to note that the input receiver aperture in Chapter III *was* located at lens l_3. However, any slight shift in the receiver aperture plane due to the insertion of the LCSLM will result in an extra quadratic phase term at the fiber endface that is negligible. Thus, the mathematics developed earlier will not be effected.

With this new system, one can clearly see that in order to obtain the maximum F/R coupling efficiency, the shape of the Fourier transformed LCSLM field must match

the shape of the modal field supported by the fiber as nearly as possible. This gives us two very distinct fields with which to perform the Gerchberg-Saxton algorithm, the target return at the receiver aperture plane and the LP_{01} mode of the fiber. The basic Gerchberg-Saxton algorithmic process can readily be applied to the receiver of the general illumination ladar system shown in Figure 6.1. For ease of understanding, a flowchart depicting the steps of the algorithm, as applied to our system, is shown in Figure 6.2.

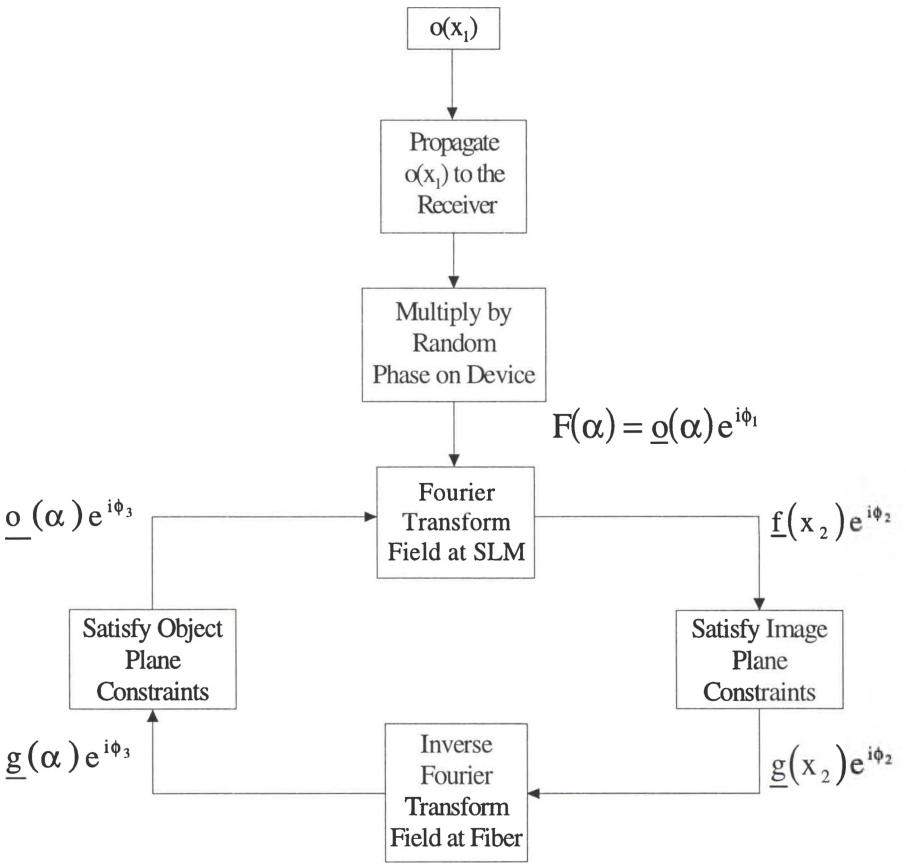

Figure 6.2: Flowchart depicting the steps involved in the Gerchberg-Saxton algorithm.

Walking our way through the process, we see the field at the target plane, after multiplying by the target's reflectivity, $o(x_1)$ is propagated to the plane of the receiver.

This field is then multiplied by the initial phase across the LCSLM. The resulting field $F(\alpha)$ is then expressed in terms of its modulus $\underline{o}(\alpha)$ and phase ϕ_1. $F(\alpha)$ is now the diffraction field we use as the starting point for the Gerchberg-Saxton algorithm. To obtain the image field at the fiber endface, we simply take the Fourier transform of $F(\alpha)$ with l_3, giving us a new field modulus $\underline{f}(x_2)$ and phase ϕ_2.

Now, here is where the power of the Gerchberg-Saxton algorithm to solve our particular problem becomes apparent. Since we ultimately want to phase filter the field at the LCSLM in an effort to make the resulting field at the fiber more like the Gaussian mode of the fiber, we satisfy the constraints in the plane of the fiber. That is, we mathematically replace the modulus of the transformed field with the modulus of the LP_{01} fiber mode $\underline{g}(x_2)$ in the algorithm, but leave the accumulated phase ϕ_2 at the fiber endface alone. The field at the fiber is then inverse Fourier transformed back to the plane of the receiver aperture, generating a new field modulus $\underline{g}(\alpha)$ and a new phase ϕ_3. This new phase ϕ_3 now contains the original object phase ϕ_1 plus an extra phase term that alters the image of the received field at the fiber endface such that it more closely matches the fiber mode. Replacing $\underline{g}(\alpha)$ with modulus $\underline{o}(\alpha)$ from the received field and combining it with ϕ_3, we now have the starting point for another iteration through the algorithm. This process is repeated until the solution stabilizes after a number of iterations. The ideal phase mask for minimizing the error between the received beam and the fiber mode can then be obtained by subtracting the original object phase from the resulting phase in the diffraction plane field at the receiver aperture.

6.2 Glint Target Coupling Efficiency Enhancement Analysis

To perform the following glint target coupling efficiency enhancement analysis, we will employ the *Matlab* software package. The ease with which this package simulates complex vector fields gives us the ability to not only model our system effectively, but allows us to easily incorporate the Gerchberg-Saxton algorithm into the routine as well. The steps involved with calculating the coupling efficiency using the computer simulations are very similar to those of the numerical integration technique developed in Chapter V. The amount of power coupled into the fiber mode can be found by adapting the steps outlined by Eq. (5-3) to typical *Matlab* modeling techniques. These steps are outlined by the flowchart depicted in Figure 6.3.

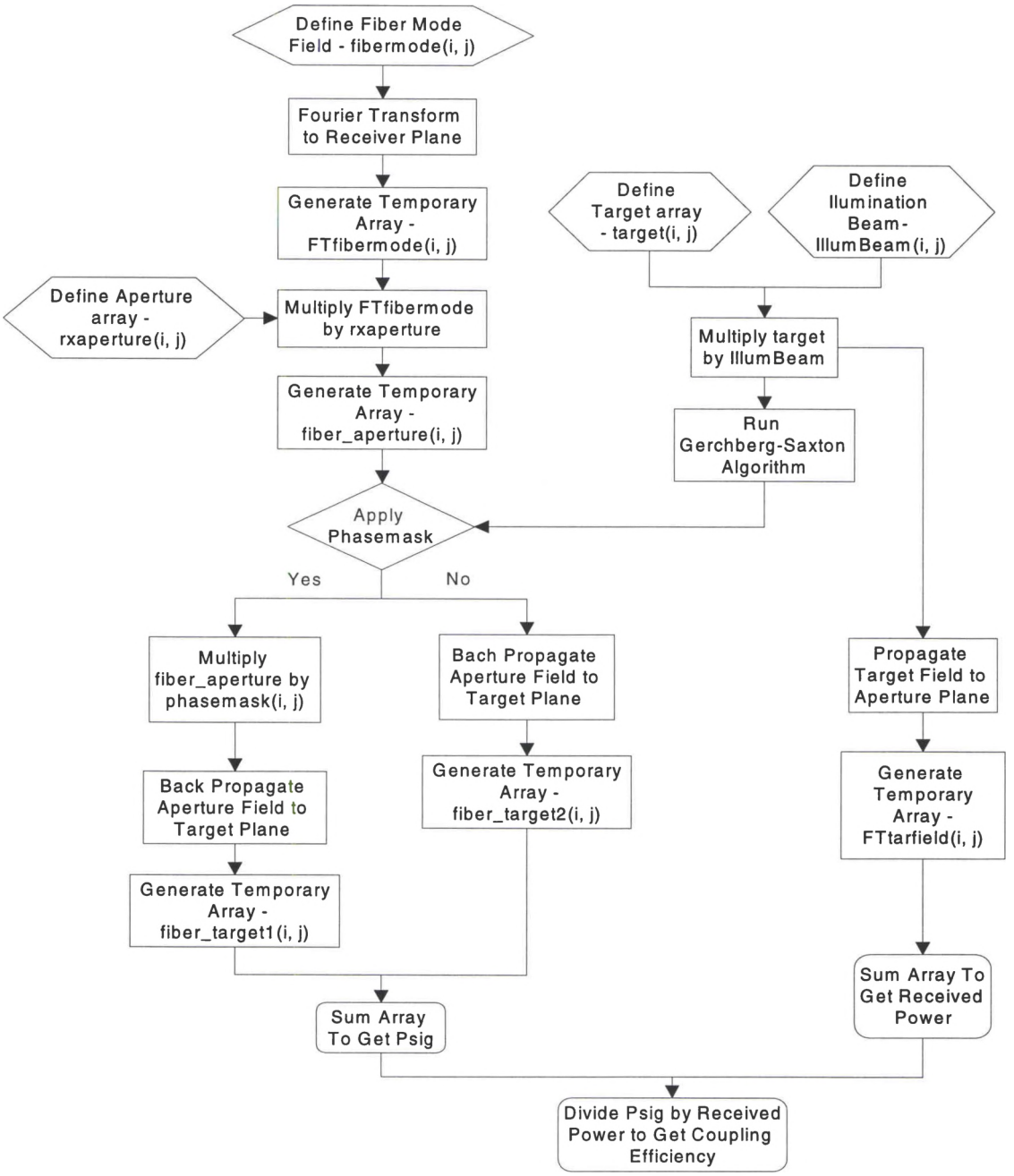

Figure 6.3: Flowchart depicting the steps involved in calculating the F/R coupling efficiency via the *Matlab* computer simulations.

Working our way through the flow chart, first a Gaussian function that simulates the LP_{01} mode of the fiber is represented here by the two dimensional array fibermode(i, j), with i and j the indices of the array in pixels. The fibermode(i, j) array is then inverse Fourier transformed to the receiver plane, generating a temporary array FTfibermode(i, j).

Multiplying the FTfibermode(i, j) array point-by-point with a separate 2-D array, $\text{rxaperture}(i, j)$, that simulates the shape of the aperture, another temporary array, $\text{fiber\_aperture}(i, j)$, can be generated. Finally, $\text{fiber\_aperture}(i, j)$ is back propagated fiber in the target plane, giving us a new array fiber_target(i, j).

Once the fiber mode is propagated to the target plane, the final overlap integral is performed between fiber_target(i, j) array, the illumination beam array, $\text{IllumBeam}(i, j)$, and the target array, target(i, j). At this point, all of the information about a specific target is defined. Depending on how the parameters of $\text{IllumBeam}(i, j)$ and target(i, j) are set, the F/R coupling for any combination of resolved/unresolved, glint/diffuse targets with singlemode/multimode returns can be examined. With all the field arrays now characterized, the power coupled into the fiber mode P_{sig} can be calculated by numerically integrating the final $\text{Psig}(i, j)$ and taking the magnitude squared of the resulting sum. Here, the numerical integration was approximated by summing all elements of the two-dimensional array and multiplying by the sampling period in x and y.

Yet, to find the F/R coupling efficiency we also need to know the amount of power collected by the receiver aperture. This is found separately by propagating the product of the $\text{IllumBeam}(i, j)$ and target(i, j) arrays to the receiver aperture and multiplying resulting array on a point by point basis with the aperture array, $\text{rxaperture}(i, j)$. Thus, P_R can be readily calculated by numerically integrating the magnitude squared of the resulting field, $\text{FTtarfield}(i, j)$. We then divide the summed value from $\text{Psig}(i, j)$ by the corresponding value from the $\text{FTtarfield}(i, j)$ array. This

result is then multiplied by a single constant, accounting for the all of the Fourier transform scaling terms generated throughout this process, to finally obtain the F/R coupling efficiency. Note, the methodology involved in determining the specific scaling constant for both glint and diffuse targets will be discussed in greater detail in Appendix C.

After the above routine for determining the F/R coupling efficiency is established, incorporating the Gerchberg-Saxton algorithm into the process is rather straightforward. Before running the subroutine that calculates the F/R coupling efficiency, the optimal phasemask for increasing coupling is determined using the error reduction algorithm outlined in Section 6.1 with the *Matlab* software package. This phasemask is then another 2-D array across the plane of the receiver given by $\text{phasemask}(i, j)$. Thus, when FTfibermode(i, j) is multiplied by $\text{rxaperture}(i, j)$ on a point-by-point basis, including the $\text{phasemask}(i, j)$ array into the coupling efficiency subroutine can be accomplished simply by performing another point-by-point multiplication in the plane of the receiver before proceeding with the calculation.

Continuing with our analysis, we now calculate the F/R coupling efficiency for a specific resolved, glint target with and without the phasemask across the LCSLM using the *Matlab* code found in Appendix C. Again we will examine a general illumination ladar system illuminating a circular resolved target with a singlemode return and incorporating a singlemode optical fiber receiver, 8.3 μm in diameter and a wavelength of λ=1.064 μm. Furthermore, we will also assume that vignetting does not occur with the addition of the liquid crystal spatial light modulator directly in front of the receiver

aperture. This allows us to keep our original 10 cm circular receiver for consistency. The other relevant parameters that will be used in this analysis are the following: an optimum truncation ratio of R=4, a beam waist of ω_0 = 2.5 cm at the transmitter, a target range of L = 20 km, an illumination wavelength of λ = 1.064 μm, a receiver numerical aperture of NA = 0.13, and a diameter of D_R = 10 cm. Incorporating these specific parameters into the routine allows us to directly compare our results with those of Figure 5.2.

Inspecting the *Matlab* computer code in Appendix C, one finds that after each of the arrays are initially defined, the Gerchberg-Saxton phasemask can be determined. Figure 6.4 displays the phasemask across the receiver for the circular glint target described above.

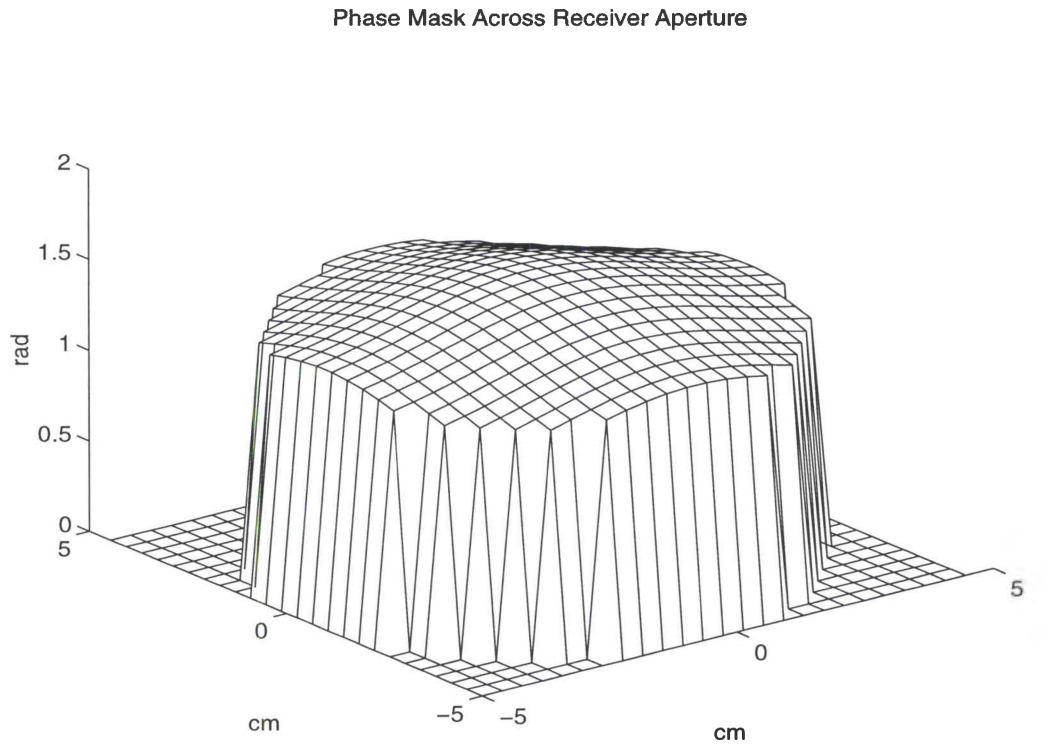

Figure 6.4: Gerchberg-Saxton phasemask across the liquid crystal spatial light modulator for a resolved, glint target with a singlemode return.

As we can see, the magnitude of the beam shaping phase mask across the entire aperture is fairly constant. Only at the edges of the lens, where the Fresnel phase curvature is more pronounced, do we see any appreciable change in the optimal phasemask and even then, the magnitude of the difference from the center of the pattern is only about ¼ radians.

It is also important to note that for the computer simulations, a circular target with a diameter of D_t = 1 m was assumed in order to define the target(i, j) matrix. However, because we ultimately want to compare the simulation results with results for the resolved targets of Figure 5.2, the portion of the IllumBeam(i, j) array that actually overlaps with the target(i, j) array is small. Thus, the illuminated portion of the target still falls within the diffraction limited spot size of the receiver, and thus we have a singlemode return.

Having calculated the ideal error reduction phasemask with the Gerchberg-Saxton algorithm, we can now determine the F/R coupling efficiency with and without the phasemask across the receiver. Table 6.1 displays the values of F/R coupling efficiency for the numerical integration found in Figure 5.2 as well as the values for coupling efficiency found by the *Matlab* simulations.

Table 6.1: Glint target F/R coupling efficiency values from the numerical integration and *Matlab* computer simulations for a singlemode target.

Calculation Technique	F/R Coupling Efficiency Without Phasemask	F/R Coupling Efficiency With Phasemask
Numerical Integration (Figure 5.2)	51.52%	NA
Matlab Computer Simulations	52.09%	52.38%

Note, by calculating the F/R coupling efficiency after each iteration through the Gerchberg-Saxton routine, it was observed that the solution stabilized after only five times through the error reduction cycle and remained constant through ten thousand iterations of the routine. Therefore, the above values of F/R coupling efficiency incorporating the phasemask have been found for one hundred iterations through the Gerchberg-Saxton error reduction algorithm.

As we can see in Table 6.1, there is a slight discrepancy between the numerical integration and computer simulation baseline values for coupling without the phasemask. This effect can be readily attributed to the discrete sampling of the functions necessary for the computer simulations.[20] When a function is modeled within the framework of the *Matlab* computer software, one can not simulate the original, continuous function with infinite support exactly [i.e. the function must be truncated]. Instead, the truncated function is sampled at a regular pixel interval, and individual magnitude values calculated at these positions. These values are then substituted into the array describing the specific function to be incorporated into the program routine. Thus, it becomes the responsibility of the programmer to set the discrete sampling such that the simulated computer function matches the original, continuous function as closely as possible.

To illustrate this point more clearly, let us examine the Gaussian modal field of the fiber shown in Figure 6.4.

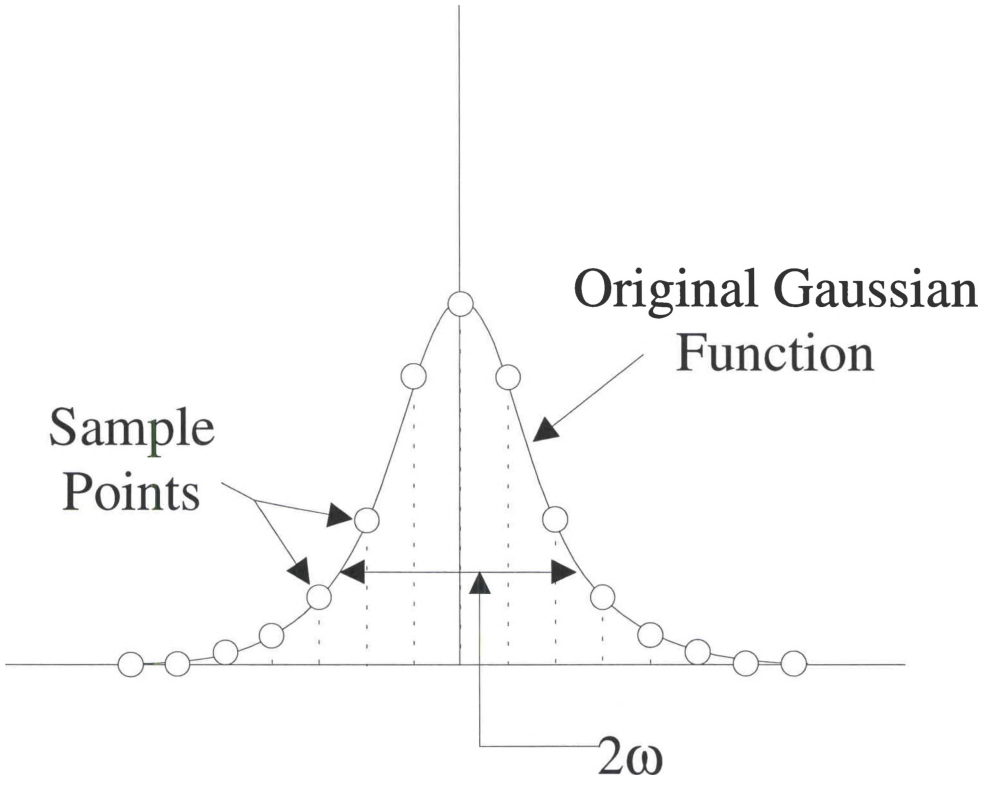

Figure 6.4: Discrete sampling example for the LP_{01} mode of the fiber as used in the computer simulations.

Here N_s is the number of samples across the Gaussian and ω is the 1/e waist of the Gaussian mode in pixels. To model the Gaussian mode of the fiber with the *Matlab* software appropriately, the modal function must be sampled at a minimum interval in order to ensure that aliasing does not occur.[21] This minimum sampling rate is generally accepted to be at least twice the highest spatial frequency contained within the function and is known as the Nyquist rate. Since the Gaussian function extends out to infinity, we must assume an upper frequency limit, above which there is very little remaining energy. To accomplish this, the Fourier transform of the Gaussian mode function can be calculated analytically and the spatial frequency below which 99% of the energy is still present can be found. This then leads to the sampling rate necessary to avoid aliasing.

Once this sampling rate is determined, one can quickly ascertain the minimum number of N_s sample points across the Gaussian needed to model the length of the mode radius ω in pixels. Yet, by sampling the function at a frequency higher than the Nyquist rate, one can simulate the given function more accurately. For this simulation we have set the sampling rate at 15 times greater than the minimum Nyquist rate in the plane of the fiber. Here, it is important to note, that this rate was chosen so that when the fiber mode was propagated to the receiver plane and then to the target plane for the F/R coupling efficiency calculation, the Nyquist criteria would still be satisfied in both the planes. Setting this limitation becomes especially difficult when the magnitude or phase is rapidly varying at the receiver plane and care must be taken to avoid any aliasing in each plane.

Having addressed the sampling issues, we now turn our attention to the effects observed with the inclusion of a phasemask across the LCSLM. From Table 6.1, we see that incorporating the phasemask across the aperture has almost no effect whatsoever on the F/R coupling efficiency for a resolved, glint target with a singlemode return. This result can be readily explained by carefully examining the nature of the overlap integral between the back propagated fiber field in the target plane and illuminated portion of the target. Since we have assumed that the focal length of the negative lens l_2 is infinity, the illumination beam in the target plane is simply an expanded Gaussian given by Eqs. (3-36) and (3-38). This beam is then completely reflected off of a glint target and overlapped with the back propagated LP_{01} mode of the fiber, which is also Gaussian. Thus, for a singlemode glint target, the two fields are already spatially matched to each other and as a result very little beam shaping occurs.

6.3 Diffuse Target Coupling Efficiency Enhancement Analysis

Although the F/R coupling efficiency did not improve for a resolved, glint target, we will now investigate the effects of filtering the same glint target phasemask from the return signal of a resolved, diffuse target. However, properly simulating a random phase across a diffuse target presents an interesting problem. By definition, a diffuse target will scatter reflected light off of it in all directions with some sort of random scintillation across the reflected wavefront. Predicting these phase fluctuations in the wavefront is nearly impossible unless specific, statistical information about the target's surface is known *a priori*. Unfortunately, under normal circumstances, this data would never be known by a real world, ladar operator.

Modeling this effect with computer software packages becomes rather challenging. To simulate a certain group of random targets with specific mean variances, correlation sizes, etc., we must generate an ensemble of phase functions. However, just by picking a random target phase for the simulation means that the phase is no longer random, but is now deterministic! When the F/R coupling efficiency is calculated for each sample function, the $\eta_{F/R}$ results obtained are only valid for that particular target phase and not a purely diffuse target. Thus, to overcome this problem and truly simulate a diffuse target, several different phase profiles across the target can be chosen and a separate F/R coupling efficiency calculated for each one of them. These coupling efficiency values are then averaged in the following manner

$$\overline{\eta}_{F/R} = \sum_{i=1}^{N_p} \left(\frac{\eta_{F/R_i}}{N_p} \right) , \qquad (6\text{-}1)$$

where N_p is the number of different phase profiles chosen within the computer simulation and $\eta_{F/Ri}$ is the individual $\eta_{F/R}$ results calculated with each new target phase. Although this function may oscillate wildly at the beginning, as N_p increases, more and more phase profiles are averaged together. As a result, the value for the computer simulated, F/R coupling efficiency should approach the results obtained through the numerical integration techniques of Chapter V.

Integrating this technique of averaging distinct, phase profiles into the routine developed in Appendix C is merely a matter of using a random variable to establish a separate array of random numbers between zero and 2π with the *Matlab* software package. This array $\text{objectphase}(i, j)$ then multiplies the same $\text{target}(i, j)$ array of the glint target routine on a point-by-point basis and the F/R coupling efficiency for a diffuse target is calculated in the manner outlined above. The balance of the glint target routine [i.e. the phasemask calculation and field propagations] however, remains unchanged. This process is illustrated in the flowchart of Figure 6.5 below.

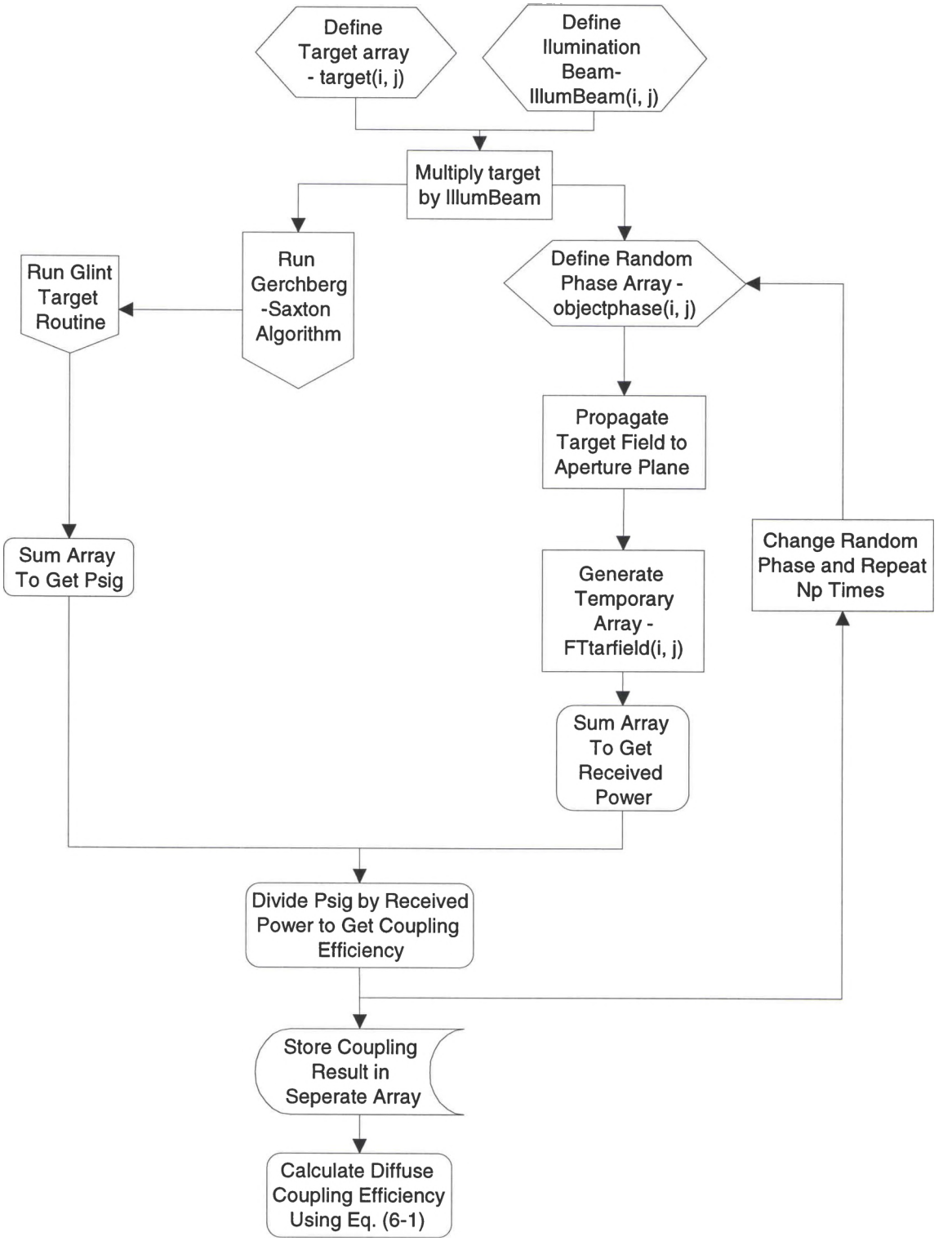

Figure 6.5: Flowchart depicting the steps involved in calculating the F/R coupling efficiency for a diffuse target via the *Matlab* computer simulations.

Figure 6.6 illustrates the results of the diffuse coupling efficiency simulations with and without the phasemask across the device for N_p = 1024 iterations of Eq. (6-1).

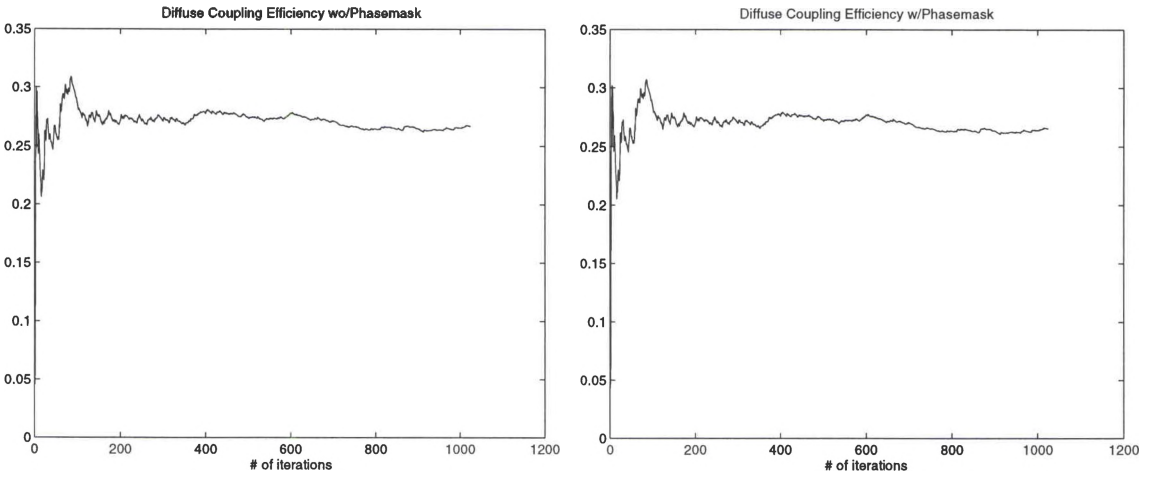

(a.) (b.)

Figure 6.6: F/R coupling efficiency for a resolved, diffuse target with a singlemode return a.) without and b.) with the glint target phase mask across the liquid crystal device.

Again, all parameters such as the truncation ratio and beam waist at the transmitter, target range, illumination wavelength, receiver numerical aperture and a diameter, and target diameter are identical to that of the glint target.

A comparison of the resulting values for diffuse F/R coupling efficiency at N_p = 1024 iteration with the numerical analysis data in Chapter V is shown in Table 6.2 below.

Table 6.2: Diffuse target F/R coupling efficiency values from the numerical integration and *Matlab* computer simulations.

Calculation Technique	Diffuse F/R Coupling Efficiency Without Phasemask	Diffuse F/R Coupling Efficiency With Phasemask
Numerical Integration (Figure 5.2)	26.57%	NA
Matlab Computer Simulations	26.68%	26.54%

Once again, we observe that the values for the computer simulation coupling efficiencies are slightly different. This is again due to the aforementioned truncation error embedded within the *Matlab* software. Since the results of the *Matlab* computer simulations with and without the phasemask do not change in Table 6.2, we can conclude that phase filtering the singlemode return from a resolved target does not increase the F/R coupling efficiency.

CHAPTER VII

Theoretical and Experimental Analysis of Phase Only Filtering Multimode Returns from Unresolved Targets

As we saw in Chapter VI, phase only filtering the singlemode returns from circular, glint and diffuse targets had no effect on the F/R coupling efficiencies for either target. This trend can be directly related to the plot of $\eta_{F/R}$ vs. illuminated target diameter shown in Figure 3.5. From the figure, we see that the F/R coupling efficiency for a truly singlemode target is already relatively high. With such a high F/R coupling efficiency already present, any room for improvement resulting from phase only filtering the return from smaller, resolved targets is limited. On the other hand, if a larger, multimode target with an inherently lower coupling efficiency is interrogated, any enhancement in coupling should be easily seen.

In this chapter, we will focus on investigating the F/R coupling efficiency from unresolved, glint and diffuse targets with multimode returns. Again, we will apply a phase filter calculated with the Gerchberg-Saxton algorithm in an effort to enhance the coupling into the LP_{01} mode of the fiber. Yet, instead of merely expanding the illumination beam and the size of the circular target to simulate an unresolved target with multimode return, we can tailor the shape of our target with a bit of intelligent foresight

to be more representative of a real world target. However, since we only have access to a 1-D LCSLM, we will switch from a circular target to a simple, separable target [i.e. a rectangular target] in all of the following simulations.

7.1 Imaging a Rectangular Target

In Chapter III, we saw that for a 10 cm target to be in the far field with respect to a single lens receiver with D_R = 10 cm in a general illumination ladar system operating at λ = 1.5 μm, L must be greater than 52 km. This requirement remained unaffected by the addition of the liquid crystal spatial light modulator in Section 6.1 since we assumed that the device was at least as large as the receiver. However, by changing to the operating wavelength to λ = 1.064 μm, our far field requirement is extended to L = 74 km. Therefore, if a rectangular target is 20 km away from the receiver, we are not in the far field and a Fresnel pattern of the target is generated at the liquid crystal device.

The collected portion of the return from an unresolved target 20 km away is simply the integral of the irradiance of the Fresnel propagated field from the target over the area LCSLM. If the target is highly multimode though, its Fresnel pattern across the LCSLM is *much* larger than the area of the aperture. To illustrate this point more clearly, the one dimensional intensity profile $I(x_R)$ of Figure 7.1 for the propagated field can be found using the Fresnel integrals given by Goodman for a rectangular target aperture,[12]

$$I(x_R) = \left| \frac{\exp\left(\frac{i2\pi L}{\lambda}\right)}{i\lambda L} \left[c(x_R) + i \cdot s(x_R) \right] \right|^2 , \qquad (7\text{-}1)$$

where

$$c(x_R) = \int_{-w}^{w} dg \cos\left[\frac{\pi}{\lambda L}(x_R - g)^2\right] \qquad (7\text{-}2)$$

and

$$s(x_R) = \int_{-w}^{w} dg \sin\left[\frac{\pi}{\lambda L}(x_R - g)^2\right] \qquad (7\text{-}3)$$

Furthermore, L is the propagation distance, λ is the illumination wavelength, w is the diameter of the target, and g is a dummy variable of integration.

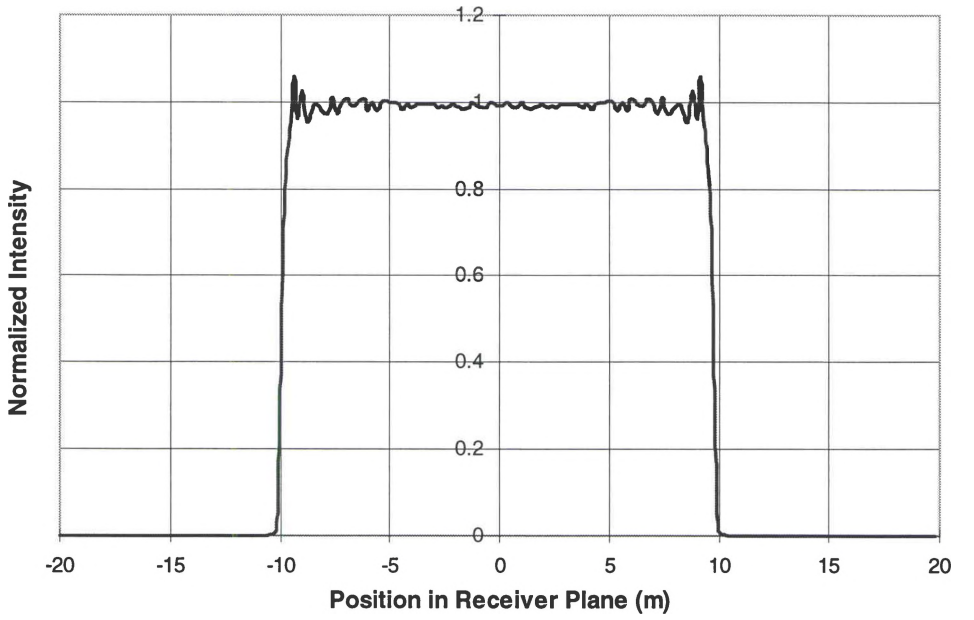

Figure 7.1: Normalized, 1-D Fresnel field from a 20 m unresolved target with multimode return at the receiver aperture.

Figure 7.1 displays the Fresnel field at the receiver for a uniformly illuminated target 20 km away and 20 m in width. As we can see, with the Fresnel field still nearly 20 m wide, a 4 cm X 4 cm liquid crystal device would only sample a very small portion of total field

near the origin. From Figure 7.1, we can also see that the intensity over the LCSLM will be essentially uniform, but still possess all of the phase information about the target.

7.2 **Fraunhofer Diffraction from a Slit Target**

In the previous section, we saw that the multimode return from a target in the near intensity profile is much larger than the extent of the LCSLM aperture but still contains the phase information about the target. Unfortunately simulating this phase profile in the laboratory would be nearly impossible. However, this difficulty can be overcome by modifying the receiver in such a manner that we first image the target with an imaging lens l_{IL} and then Fourier transform the *image* with a second transform lens l_4. As a result, a very different phase pattern can be generated across the liquid crystal device. These alterations to the current receiver in Figure 6.1 are shown in Figure 7.2.

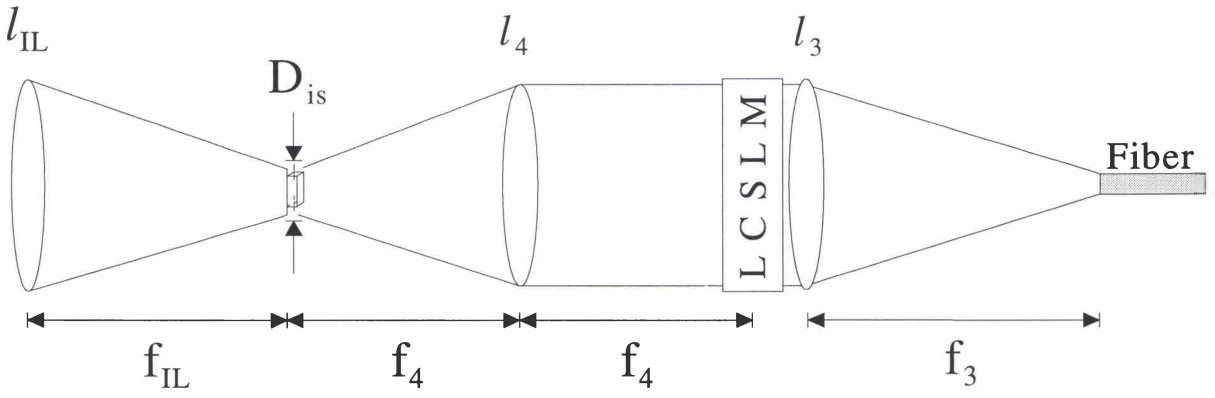

Figure 7.2: Modified general illumination ladar receiver with an imaging and Fourier transform lens before the LCSLM.

Here, the D_{is} denotes the width of the imaged rectangular target and f_{IL}, f_4 and f_3 and the focal lengths of the imaging lens, the second transform lens, and the receiver coupling optic respectively.

With the addition of the second transform lens into the system, several advantages are gained. Situating l_4 such that the image of the rectangular target is in the front focal plane, a Fraunhofer pattern of the target can be formed across the device if the spatial light modulator is placed in the back focal plane of the lens. Thus, we effectively move the target out to the far field regardless of its actual distance from the receiver. For a rectangular target, this far field pattern at the LCSLM is the all too familiar sinc pattern given by[22]

$$\mathcal{F}\left\{\text{rect}\left(\frac{x_1}{D_{t,x_1}}\right)\Bigg|_{x_1=\frac{x_2}{\lambda f_4}}\right\} = \text{sinc}\left(\frac{D_{t,x_1}x_2}{\lambda f_4}\right) \qquad (7\text{-}4)$$

with its zeros located at

$$x_2 = \frac{\lambda f_4}{D_{t,x_1}} \qquad (7\text{-}5)$$

Here, D_{t,x_1} is the x dimension of the target image, x_1 and x_2 are the spatial variables associated with the front and back focal planes of l_4 respectively. At this stage, it is also important to note that due to the separable nature of the x and y coordinates of a rectangular target, a similar expression can be generated for the y dimension simply by replacing every x in Eqs. (7-4) and (7-5) with y. Thus, throughout the remainder of this argument, we will focus our attention only on the 1-D pattern in the x direction while still maintaining that an identical process can be performed along the y dimension.

By knowing the locations of the sinc pattern's zeros, the spatial extent of the sinc function on the device may be adjusted by varying the focal length of l_4 if the size of the target image is also known. Since the target is several kilometers away, the approximate Fresnel magnification M_{IL} of the imaging lens in Figure 7.2 can be found using the relationship[11]

$$M_{IL} = -\frac{S_2}{S_1} \cong -\frac{f_{IL}}{L} \tag{7-6}$$

Multiplying Eq. (7-6) by the dimensions of the target, we can readily attain the size of the imaged target in the focal plane of l_{IL}. Now choosing some typical ladar parameters such as L = 20 km and that l_{IL} is a f/3 lens with a focal length of f_{IL} = 30 cm, the association between the image size and the true target width can be determined as shown in Figure 7.3. Note, this relationship will be the same for either the x or y dimension and is independent of the whether or not the target is glint or diffuse.

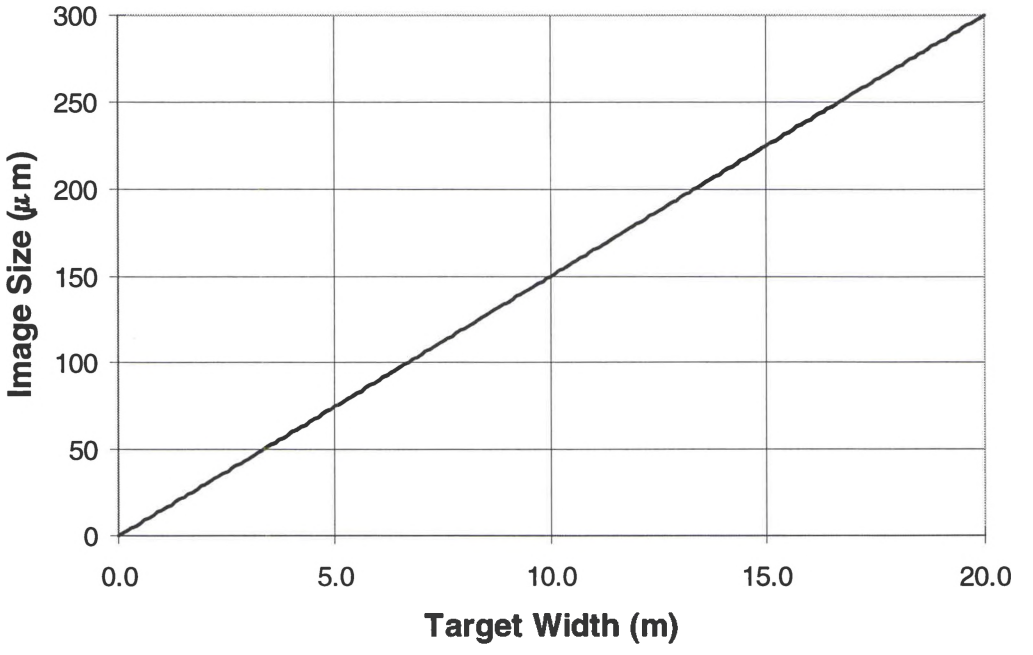

Figure 7.3: Imaged spot size vs. true target diameter.

With the size of the imaged target now known, the sinc pattern across the LCSLM can readily be determined. For this example, let us consider the normalized intensity pattern shown in Figure 7.4 for a target image diameter of $D_{t,x_1} = 300$ μm, a focal length of $f_4 = 1$ m, and a wavelength of $\lambda = 1.064$ μm.

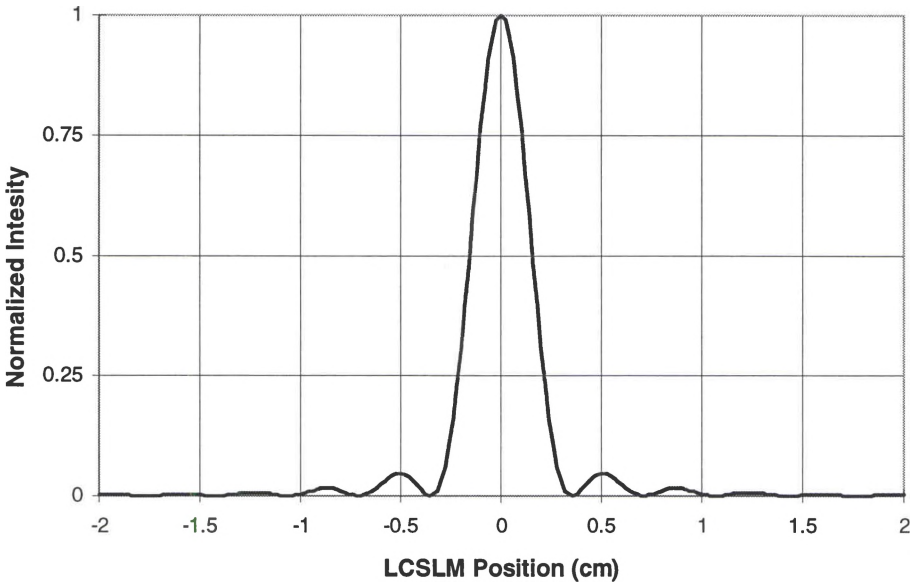

Figure 7.4: Sinc pattern across the LCSLM.

Looking at the figure, one recognizes that the majority of energy is contained in the central lobe and the three side lobes of the pattern. Thus expanding the sinc pattern until only the central lobe and the three side lobes are incident on the LCSLM, not only increases the number of device electrodes under each of the main intensity lobes, but still allows most of the energy to be passed through the aperture. Upon inspection of Eq. (7-5), we see that by increasing the focal length f_4, the zeros of the sinc pattern can be moved further away from the origin until the desired, seven lobe pattern is achieved.

Relating the f_4 that generates this seven lobe pattern on the liquid crystal device to the real target diameter, Figure 7.5 can be generated for a wavelength of $\lambda = 1.064$ μm.

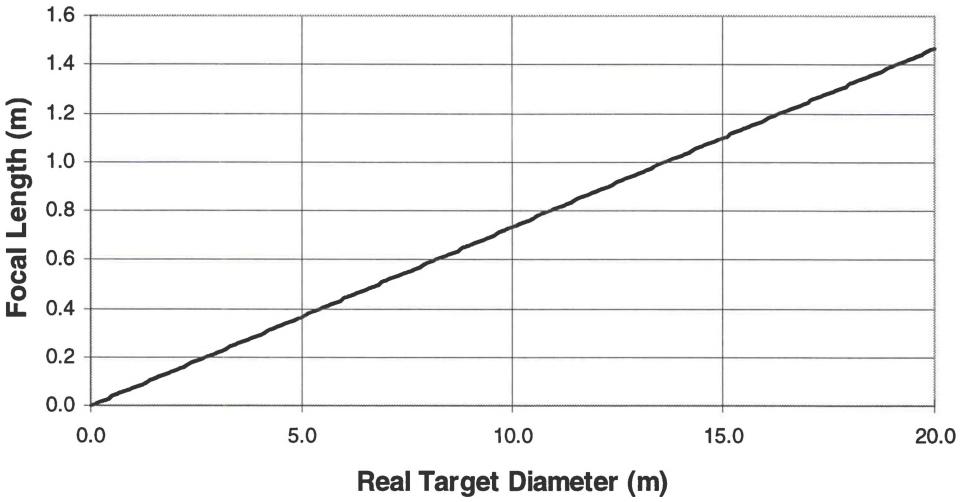

Figure 7.5: Transform lens focal length f_4 required to produce a seven lobe pattern on SLM vs. true target diameter at 20 km.

7.3 1-D Beam Shaping Simulations

Armed with the data from Figure 7.3 and Figure 7.5, we can now effectively model a real world system both theoretically and experimentally for any given target size. The image size can be simulated by illuminating a rectangular slit of the appropriate dimensions, as determined from Figure 7.3, for a specific target. Once this target is chosen, the focal length of l_4 can be extracted from Figure 7.5 to generate our sinc pattern on the spatial light modulator. In this section, we will specifically examine an unresolved target at 20 km that is 10 m in diameter and has a multimode return. Again we will assume that imaging lens is a f/3 lens with a focal length of $f_{IL} = 30$ cm. From the graphs in Section 7.2, this target would correspond to a 150 μm slit aperture and a 750 mm focal

length transform lens l_4. With the experimental criteria now established, computer simulations of the receiver system shown in Figure 7.2 can be performed to evaluate the possibility of enhancing the coupling efficiency.

Now, to ensure that we are properly modeling our system, let us briefly turn our attention to the actual components that will be used later on in the experimental setup. In Section 6.1, we assumed that the LCSLM device was at least as large as the receiver. Unfortunately, beam steering devices of this extent are commercially unavailable. Therefore, we will "exchange" the LCSLM used earlier for a more typical device, the Raytheon Demo 4 Fine 1-D device with a 4 cm x 4 cm clear aperture, and continue to operate the device at a wavelength of $\lambda = 1.064$ μm. Therefore, even though it may be possible to develop a 2-D phase mask capable of increasing the $\eta_{F/R}$ coupling into a singlemode fiber receiver, our device only possesses 1-D beam steering abilities. Thus, the degree of correction we can impose upon the incoming wavefront will be limited. With this in mind, all of the subsequent modeling and corresponding experiments will investigate the effects of applying a corrective phasemask across only one dimension of the receiver aperture. Furthermore, to minimize the spherical and coma aberrations in the transform pattern across the LCSLM and in the plane of the fiber, both l_3 and l_4 for this set of experiments will be two achromatic lenses (Newport model PAC094) with focal lengths $f_3 = f_4 = 750$ mm. By choosing the same focal length for f_3 and f_4, we have strictly a one-to-one magnification relationship between the image planes of the system. However, the effects of varying both focal lengths will be examined in Section 7.5.

Having set the experimental parameters, we again employ the Gerchberg-Saxton algorithm outlined in Chapter VI to find the ideal 1-D phasemask for a rectangular, glint

target. Yet, it is important to realize that though an imaging lens and Fourier transform lens have been inserted before the spatial light modulator, we more or less still have the same general illumination system as in Figure 6.1. Instead of Fresnel propagating the reflected field from a 10 m target, 20 km to the receiver as before, we are now merely imaging the target with the imaging lens l_{IL} first and then performing a Fourier transform operation to the receiver with a second transform lens l_4. Modifying the *Matlab* computer code in Appendix C to account for these changes as well as the new experimental guidelines, the ideal phasemask for a 150 μm target image and a 750 mm focal length transform lens l_4 is displayed in Figure 7.6.

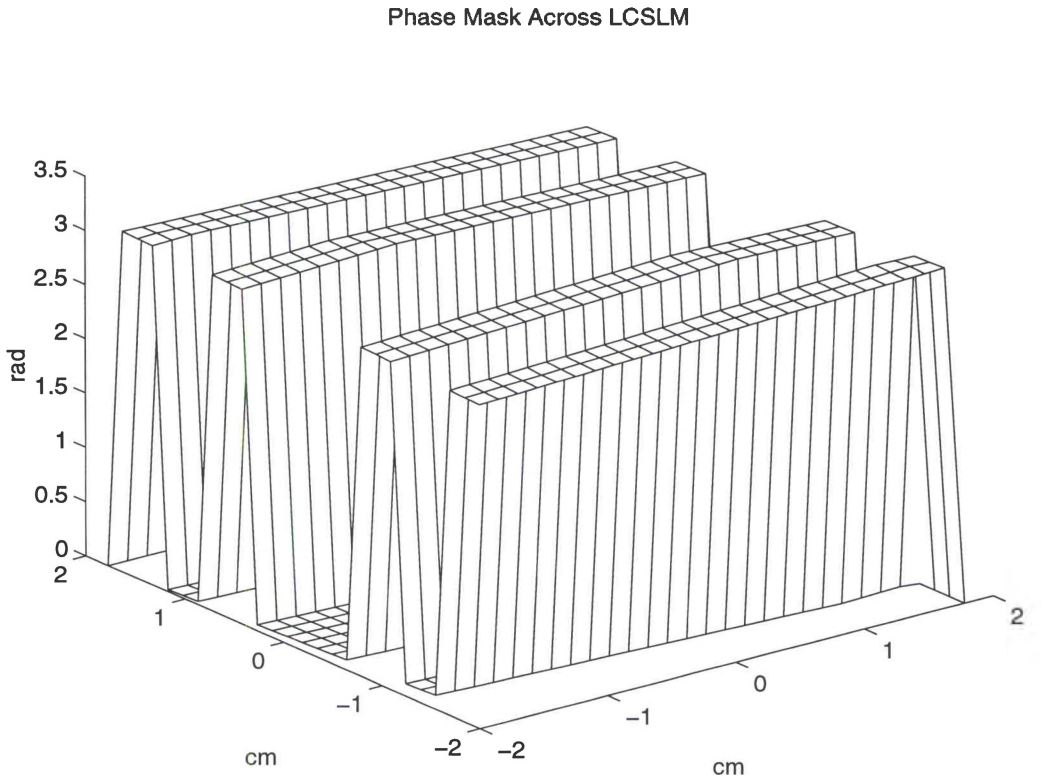

Figure 7.6: Ideal phasemask for increasing the F/R coupling efficiency from a 150 mm rectangular, target image that has been Fourier transformed onto the LCSLM with a 750 mm lens.

Upon inspection of the figure, one can see seven distinct regions of alternating zero and π phase. This effect arises from the alternating side lobes in the sinc pattern of the *field* across the device. Every time the field pattern crosses a zero, the values of the sinc pattern change from positive to negative, causing an abrupt phase shift of $-\pi$ in the wavefront. Thus, everywhere the field at the receiver has a negative value, the ideal phasemask compensates for this with a region of π phase

Once the Gerchberg-Saxton phasemask has been determined, the F/R coupling efficiency with and without the phasemask can be calculated by following the same process outlined in Chapter VI. Yet, this time instead of calculating the overlap integral in the target plane, the overlap integral is performed between the back propagated LP_{01} fiber mode and the *slit* target in the front focal plane of l_4. The ideal phasemask is then calculated and used to phase only filter the returns from various targets/image spots. Figure 7.7 illustrates the results for the factor increase in F/R coupling efficiency .

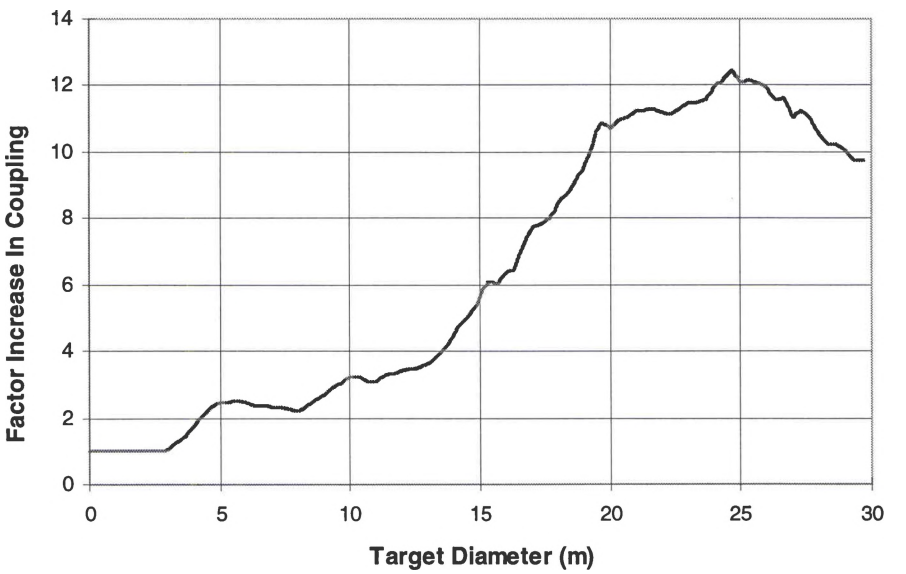

Figure 7.7: Factor increase in coupling vs. target diameter resulting from 1-D phase only filtering the return from a glint target.

As in Chapter VI, we again see that for singlemode targets and targets whose diameters are less than three meters, no increase in F/R coupling is realized. Yet, as the target's diameter is slowly increased, the factor increase in coupling steadily improves until a factor of 12x for a 25 m target is achieved. Form this point, the factor increase in coupling decreases for larger targets. We can attribute this decrease to the fact that for larger targets, the sinc pattern across the LCSLM narrows. This reduces the number of sample points [i.e. electrodes] across each oscillation of the sinc pattern in the receiver plane, and thus causing an under sampling problem within the *Matlab* routine.

Close inspection of Figure 7.7 also reveals a slight oscillation in the curve where regions of lower coupling increases are created. This effect is especially prominent in the target diameter region between 5 and 10 m. After reaching a maximum coupling increase of 2.48x for a 5.5 m target, the factor increase drops to 2.21x for an 8 m target before climbing to 3.25x for a 10.5 m target. This peculiarity arises from the changes in the number of zero and π phase shifts within the calculated phase mask. In the areas where coupling increases actually turns and starts to decrease, another region of zero phase shift is added to either side of the phase pattern in Figure 7.6. Therefore, the edging effects caused by the Discrete Fourier Transform (DFT) within the *Matlab* routine are slightly enhanced[19] and the energy in the target plane of the back propagated LP_{01} mode is spread out over a wider area. This brings the magnitude of the corrected P_{sig} integral down and decreases the overall change in coupling increase. Once the target size is sufficiently increased, the phase mask reaches its next transition point, another region of π phase is added to Figure 7.6, and the curve in Figure 7.7 starts to increase again. Alternation between these zero and π phase additions continue, but as the target sizes get larger, the

time between these transitions decreases. As a result, the sinc pattern across the LCSLM narrows and the effect becomes less obvious. In the next section, we will examine experimentally several points along the curve in Figure 7.7 to verify the theoretical data and test the feasibility of the phase filtering process in a general illumination ladar system.

7.4 Experimental Phase Only Filtering of Multimode Returns

Having completed the necessary system modeling, we will now investigate the methodology involved with experimentally verifying the factor increases in $\eta_{F/R}$ for several different targets. As stated earlier, a real world target can be imaged to the front focal plane of l_4. Using the relationship developed in Figure 7.3, this image size can be simulated experimentally by back illuminating an air slit of the appropriate dimensions. For the following analysis, we will specifically look at a series of precision air slits 100 μm, 150 μm, and 200 μm by 3 mm manufactured by Melles Griot. These particular slits correspond to set of rectangular targets 20 km away and 6.67 m, 10 m, and 13.67 m in width respectively.

The experimental setup used for the phase only filtering measurements is shown in Figure 7.8.

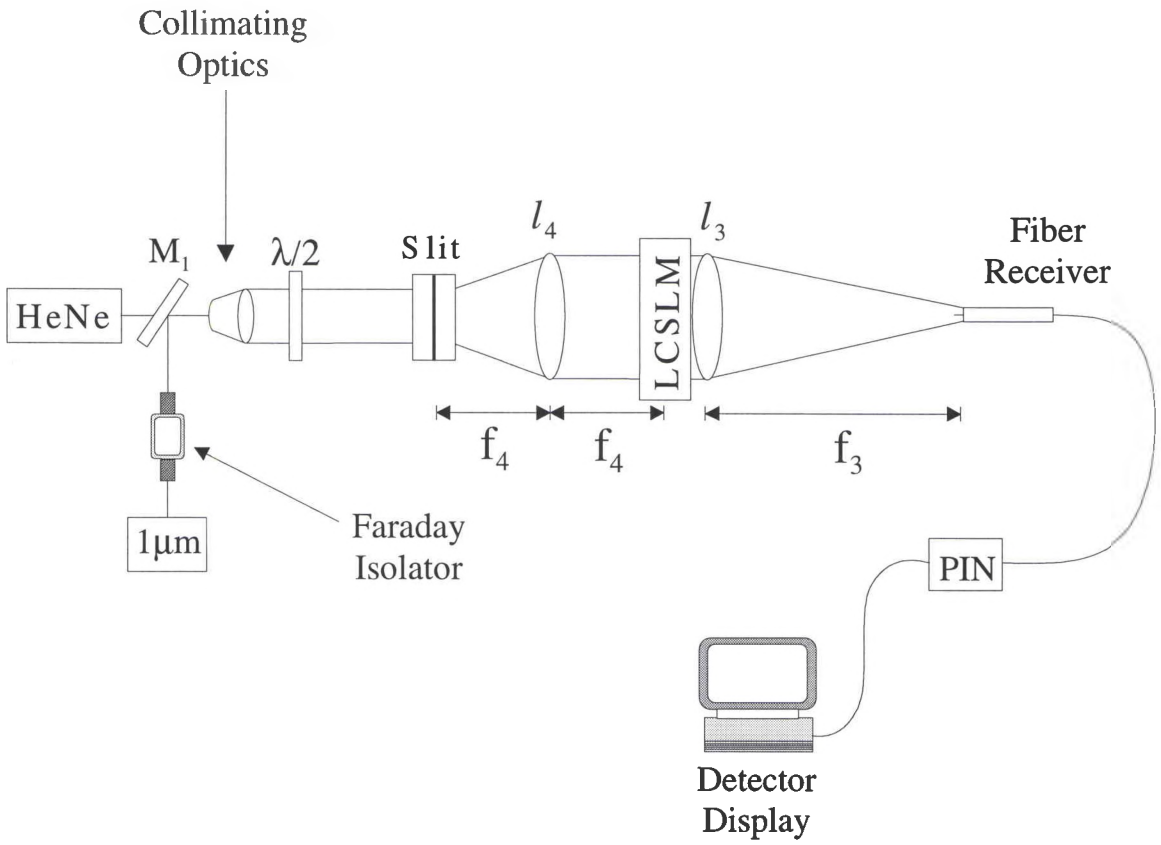

Figure 7.8: Experimental setup.

To aid with the alignment of the 1.064 μm beam from a Lightwave 120-03 Nd:YAG laser system, a green HeNe laser beam (λ = 532 nm) was initially passed through two pinholes spaced three meters apart along the optic axis. A high energy laser mirror M1, reflective between 1053-1064 nm, was then placed in the path of the HeNe beam at a 45° angle. While maintaining the alignment of the green HeNe beam through the two pinholes, the one micron beam was passed through a Faraday isolator, reflected off M1, and the position of the Lightwave laser adjusted until the 1.064 μm beam was coincident with the

green beam through the pinholes. Once the alignment of the two beams was established, the remainder of the components where added one at a time.

Proceeding through the optical setup, the one micron beam is first collimated and then passed through a half waveplate λ/2. This waveplate allows one to adjust the polarization of the light such that it is parallel to the axis of the extraordinary refractive index of the liquid crystals in the Raytheon Demo 4 device required for proper phase modulation. After emerging from the collimator and half waveplate assemblies, the infrared beam has been expanded to approximately 6 mm in diameter. Therefore, by the time the beam reaches the apparatus holding either the 100, 150, or 200 micron slit, the extent of the beam is large enough that we can assume that the illumination over the narrow dimension of the slit is nearly uniform. Now we have our simulated target image in the front focal plane of l_4 and the remainder of the components including the fiber are identical to those described in Section 7.3. From here, the signal coupled into the optical fiber is measured with a Coherent LabMaster-E power meter equipped with a LP-2 silicon photodiode detector.

Table 7.1 gives the experimental results for the 100, 150, and 200 micron slits and compares these results with the specific theoretical values from Figure 7.7.

Table 7.1: Theoretical and experimental results for factor increase in coupling for a.) 100 μm slit, b.) 150 μm slit and c.) 200 μm slit.

Quantity	Theoretical Results, 100 μm Slit	Experimental Results, 100 μm Slit
Power coupled w/o phasemask	NA	96 ± 5 nW
Power coupled w/ phasemask	NA	207 ± 5 nW
Total power in fiber plane	NA	209 ± 5 nW
$\eta_{F/R}$ w/o phasemask	0.0488%	0.046 ± 0.003 %
$\eta_{F/R}$ w/ phasemask	0.1144%	0.099 ± 0.003 %
$\Delta\eta_{F/R}$	2.35x	2.16 ± 0.12x

(a).

Quantity	Theoretical Results, 150 μm Slit	Experimental Results, 150 μm Slit
Power coupled w/o phasemask	NA	185 ± 5 nW
Power coupled w/ phasemask	NA	550 ± 5 nW
Total power in fiber plane	NA	0.48 ± 0.01 μW
$\eta_{F/R}$ w/o phasemask	0.038%	0.038 ± 0.001 %
$\eta_{F/R}$ w/ phasemask	0.122%	0.114 ± 0.002 %
$\Delta\eta_{F/R}$	3.22x	2.97 ± 0.08x

(b.)

Quantity	Theoretical Results, 200 μm Slit	Experimental Results, 200 μm Slit
Power coupled w/o phasemask	NA	184 ± 5 nW
Power coupled w/ phasemask	NA	630 ± 5 nW
Total power in fiber plane	NA	0.53 ± .01 mW
$\eta_{F/R}$ w/o phasemask	0.0302%	0.0347 ± 0.002%
$\eta_{F/R}$ w/ phasemask	0.1184%	0.1188 ± 0.009%
$\Delta\eta_{F/R}$	3.87x	3.42 ± 0.10x

(c.)

Note, all experimentally measured values contain a ± error for the power coupled into the fiber. This inaccuracy arises from the fluctuations in the position of the fiber due to the air circulation in the laboratory area. Even after taking this discrepancy into account,[23] one can see that the experimental results for both the 100 μm and 150 μm slits are very close to the theoretical predictions from the *Matlab* routine. The 200 μm slit on the other hand, does differ somewhat and has a slightly lower factor increase than expected.

Inspecting Table 7.1, one realizes that the experimental F/R coupling efficiency enhancements is slightly lower than theoretical predictions for each slit. These discrepancies can easily be attributed to the difficulty involved with aligning the specific phasemasks in the system. Since the spacing between each zero and π phase transition within the phasemask is only 80 μm, it is very difficult to align the phasemask with the diffraction pattern from the slit across the LCSLM. Any deviation from the proper position will decrease the amount of beam shaping we can perform upon the incoming wavefront. The effects of this misalignment can be seen by profiling the corrected dimension of the beam in the plane of the fiber. Employing a simple knife-edge scanning technique and measuring the power incident on a detector at various positions, beam profiles for the uncorrected and corrected wavefronts may be found. These experimental profiles are shown in Figure 7.9 while the theoretical profiles are given in Figure 7.10.

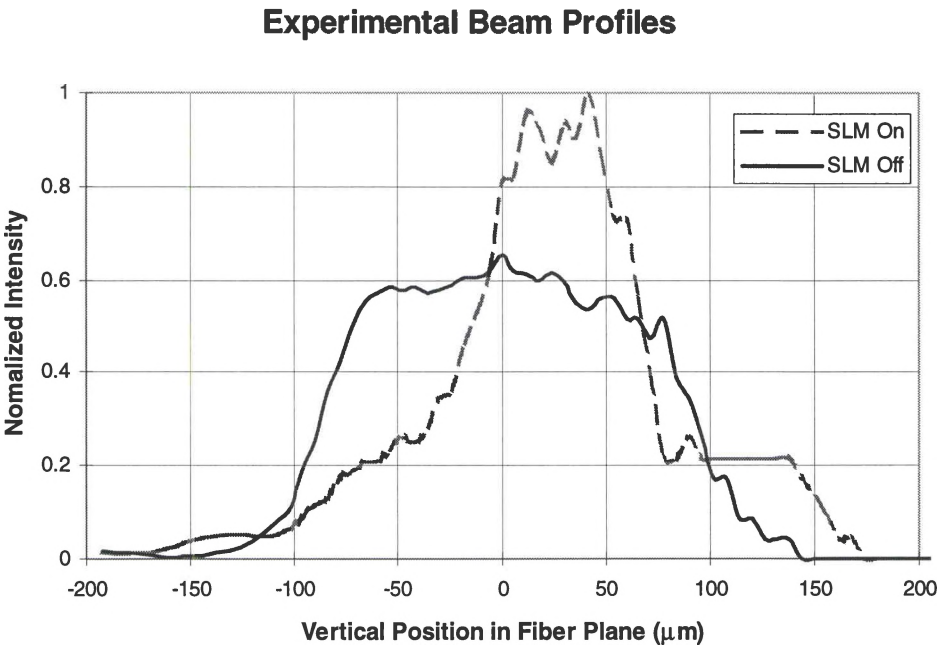

Figure 7.9: Experimental beam profiles in the plane of the fiber with and without the phasemask present.

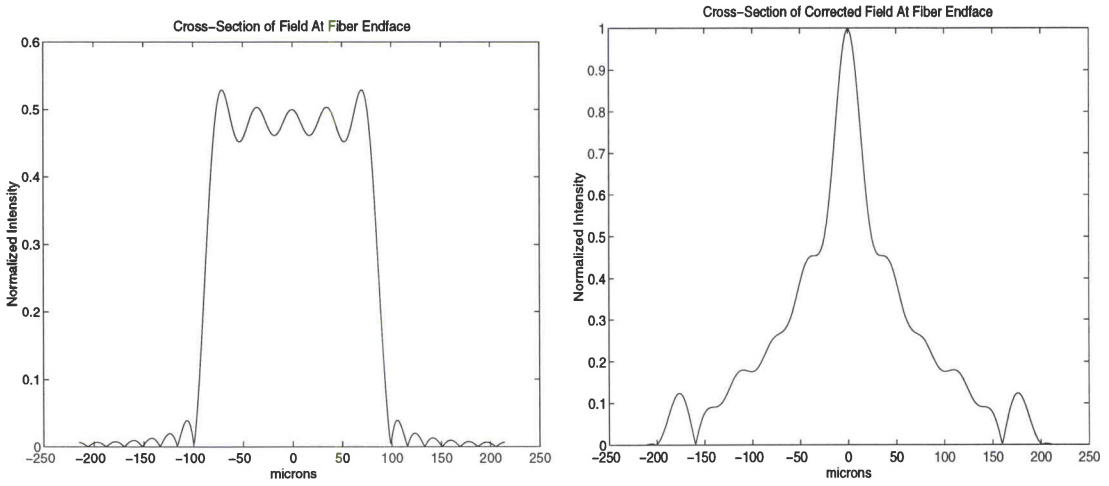

(a.) (b.)

Figure 7.10: Theoretical beam profiles in the plane of the fiber a.) without and b.) with the phasemask present.

Comparison of the two beam profiles show that unlike Figure 7.10b, the corrected wavefront in Figure 7.9 is shifted to the right of center and fluctuates a bit near the peak. These effects are most likely due to the misalignment of the phasemask itself and will ultimately affect the degree of coupling realized. Figure 7.9 also shows a significant fluctuation in the difference between the filtered and unfiltered wavefronts depending on where the fiber is located. This could further explain the discrepancy in the factor increase between the experimental and theoretical models. Correcting for these mistakes in the future could only improve the results.

7.5 Further Observations

Although we have just seen that improperly aligning the phasemask or the fiber within the system can greatly effect the factor increase in F/R coupling efficiency, changing any other component in the system will also effect the degree of coupling increase obtained. As in Chapter III, by changing the back focal length of l_3 after the LCSLM one runs the risk of mismatching the NA of the lens to the NA of the fiber. If f_3 is too small, the NA of the lens is much bigger than that of the fiber. This mismatch in NA will then cause the F/R power coupling to drop off. The opposite is true if the focal length gets too big. Even though the NA of the lens gets smaller, there is a trade off in coupling due to the increased size of focused spot. As a result, if f_3 is too big, most of the focused energy fails to overlap with the core of the fiber and the F/R power coupling will again decline. This effect is displayed in Figure 7.11 for a constant slit size of 150 μm, a front focal length f_4 = 750 mm, and a transmitted power of 1 Watt.

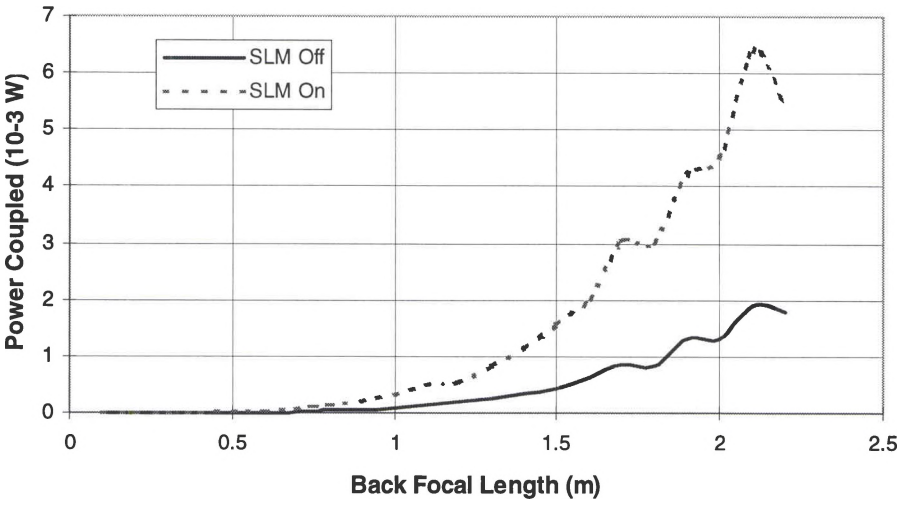

Figure 7.11: Power coupled vs. back focal length of l_3 for a 150 μm slit.

Again we see the same edging effects as in Figure 7.7. However, it is relatively simple to determine the effect on the F/R coupling enhancement by dividing the value of the power coupled while the LCSLM is on by the value when it is off. These results are shown in Figure 7.12.

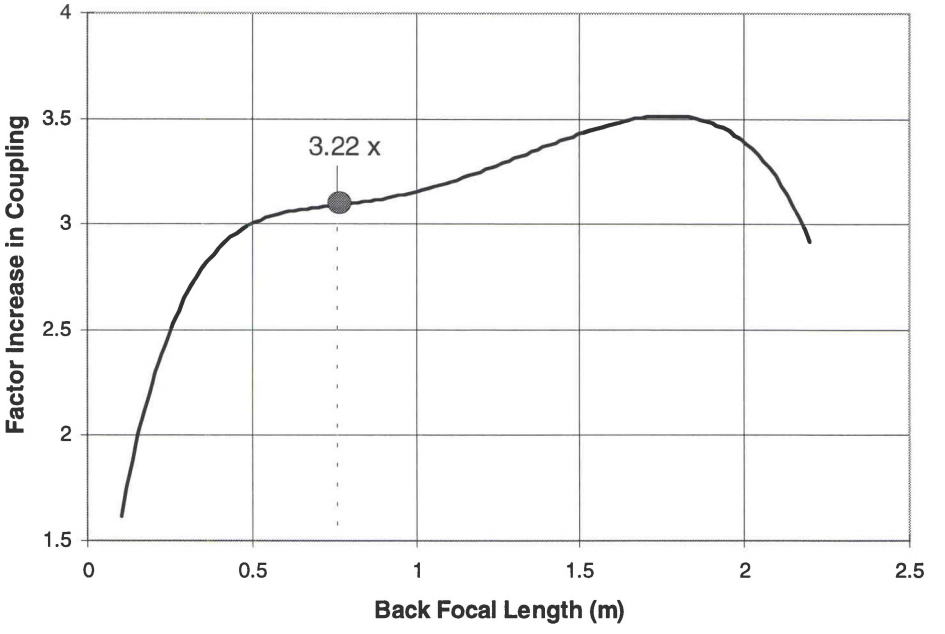

Figure 7.12: Factor increase in coupling vs. back focal length of l_3 for a 150 μm slit .

Using Eq. (2-12) with M = 1, one can calculate that the system would be NA matched to the 8.3 μm fiber when the focal length of $f_3 \approx 1.95$ m. As expected in the above figure, we see the maximum enhancement in F/R coupling efficiency occurs near this value as well.

Changing the focal length of the front transform lens l_4 has a similar effect on the factor increase in coupling. This trend can best be explained by recalling Eq. (7-5) and focusing on the patterns at the LCSLM, we see that by increasing f_4, the zeros in the transform pattern for a given slit/image size will move further apart. This will cause the pattern across the device to become more spread out and its shape to look more Gaussian. Thus, the back propagated fiber mode looks more like the received field and the overall F/R coupling efficiency will improve. Eventually increasing the front focal length too much pushes the first zeros of the sinc pattern past the edge of the liquid crystal device, leaving us with only the central lobe upon which to perform any beam shaping operations. After this point, the pattern changes very little and the effects of the phasemask on F/R coupling efficiency will level off. The baseline $\eta_{F/R}$, on the other hand, will continue to rise and thus cause the factor increase in coupling to decline. This effect of varying the front focal length is shown in Figure 7.12 for a slit size of 150 μm and a back focal length of f_3 = 750 mm. Again, the actual values of F/R coupling efficiency calculated with the *Matlab* routine of Appendix C, with and without phasemask, are examined.

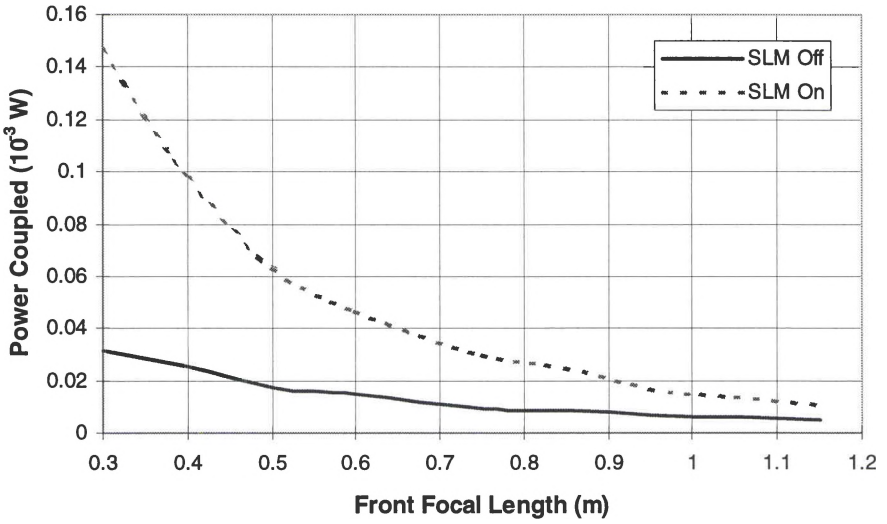

Figure 7.13: Power coupled vs. varying front focal length with and without the phasemask across the device for a 150 μm slit.

The effect on the F/R coupling enhancement can again be verified by dividing the values for coupling efficiency from the top curve in Figure 7.13 by the bottom curve. These results are displayed in Figure 7.14 below.

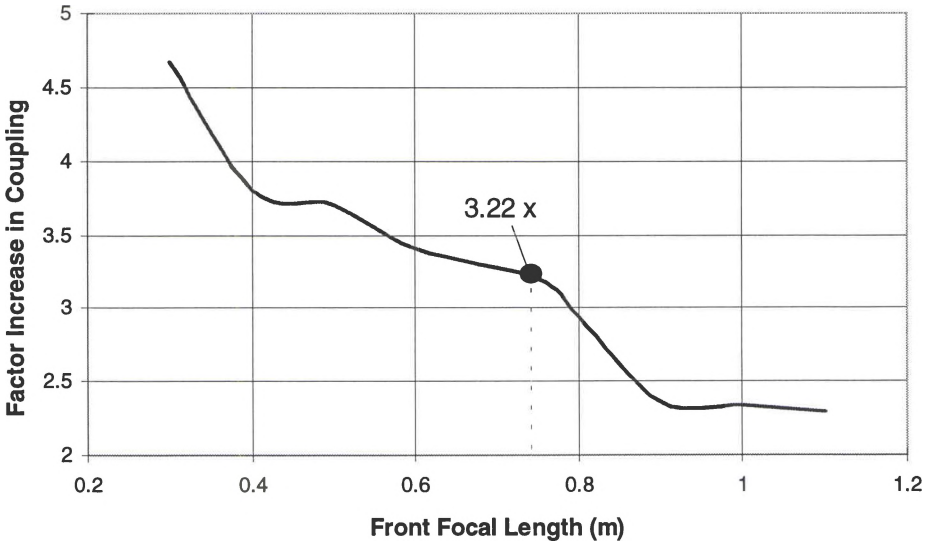

Figure 7.14: Factor increase in coupling vs. front focal length of l_4.

Altering the nature of the target itself will effect the increase in F/R coupling as well. Applying the computer simulation techniques developed in Chapter VI to a slit, the targets in Figure 7.7 may be changed from glint targets to purely diffuse targets and the factor increase in coupling efficiency for each target diameter determined. This can be accomplished by choosing several different random phase profiles N_p across the actual target and then propagating each profile to the plane of the imaging lens. Here, the imaging lens acts as a low pass spatial filter which only allows certain frequencies to pass through the aperture. The filtered phase profile is then propagated to the image plane and overlapped on a point-by-point basis with the slit target. Finally, the F/R coupling enhancement can be determined by calculating a separate F/R coupling efficiency for each N_p phase profile, and using Eq. (6-1) to find the overall coupling efficiency with an without a phase filter across the receiver. Figure 7.15 illustrates the results of the F/R coupling efficiency enhancement for a diffuse slit target with and without the phasemask across the device. Note, these results are for $N_p = 512$ iterations of Eq. (6-1).

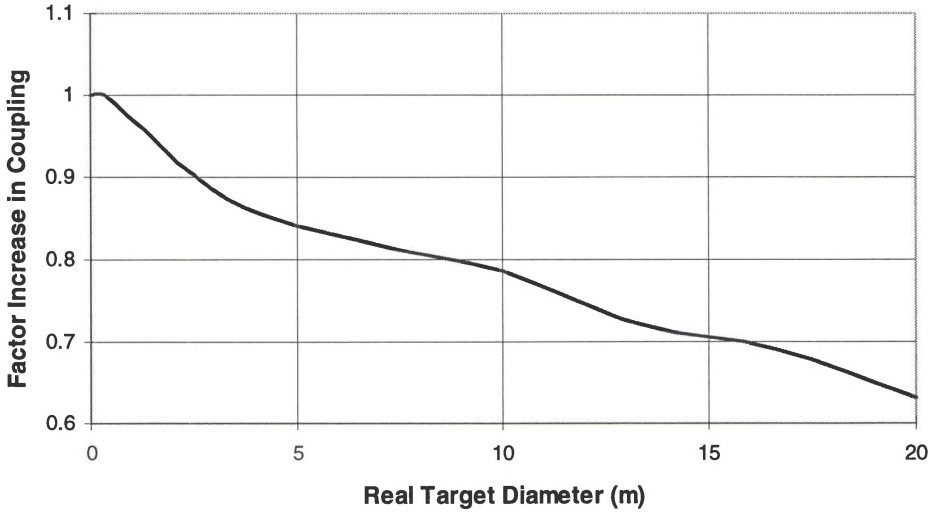

Figure 7.15: Factor increase in coupling vs. target diameter resulting from phase only filtering the return from a diffuse target.

Inspecting the above figure, one notices that instead of increasing the F/R coupling efficiency, the application of the Gerchberg-Saxton phasemask actually decreases the coupling. With a diffuse target, the reflected wavefront is scattered out in all directions by the tiny variations across the surface of the material. Since the spacing between the scattering elements is so small, the phase profile of the return contains a wider range of spatial frequencies than do the glint targets. Therefore when the back propagated fiber mode is overlapped with the reflected target field, more of the energy is located in the higher spatial frequencies [i.e. the side lobes outside of the LCSLM aperture].

Thus, for a small target, the Fourier transform of the target in the plane of the LCSLM is dominated by shape of the target itself and not the diffuse scatters of the target. The resulting sinc pattern then interacts with the phasemask across device as in Section 7.3 and we again see the same effects of Figure 7.7. However, as target size increases, more and more diffuse target scatters are present. This causes the magnitudes of the lower spatial frequencies that overlap with the phasemask to decrease and cancels out any F/R coupling efficiency gains from the phasemask. Thus effect becomes more pronounced as the target size increases, causing the curve in Figure 7.15 to decline.

7.6 Ronchi Ruling Experiment

Having established that it is possible to increase the F/R coupling efficiency into a SMOF ladar receiver by phase filtering the return from a glint target, we will now investigate more complicated target will contain several other higher spatial frequencies not present in a simple rectangular slit target. However, since we are limited to only correcting across one dimension by the Raytheon device, the target we choose must be

constant along the other dimension. These requirements can be met by merely inserting a Ronchi ruling in front of one of the slits used earlier. The alternating bands of light and dark across the ruling gives us the desired spatial complexity and the lines are symmetric.

With this target in mind, a Ronchi ruling having a line spacing of 300 lines/inch was placed in front of the 200 μm precision air slit. Converting the line spacing to lines/μm, each light and dark band was calculated to be 46 μm wide. Therefore, the resulting slit target consisted of two complete line pairs and 16 μm of another line. For simplicity, the air slit was aligned under a microscope such that the edge of the slit was parallel to the leading edge of one of the dark bands of the Ronchi ruling. Thus, the fractional portion of the fifth band corresponded to a third dark band across the slit. This arrangement is shown in Figure 7.16.

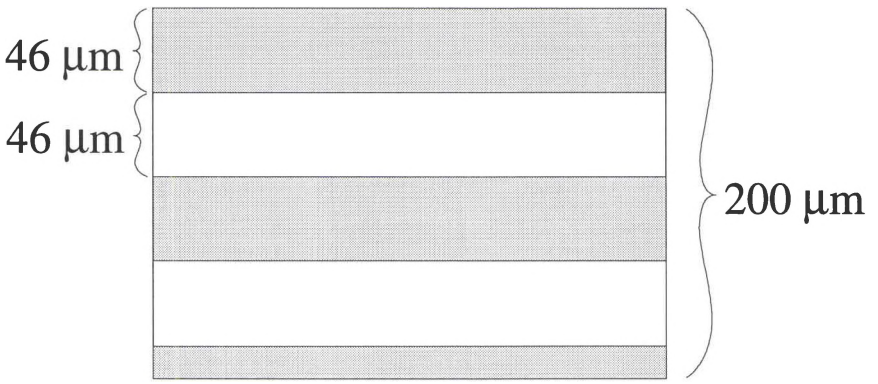

Figure 7.16: Ronchi ruling target.

Once the Ronchi ruling and slit were aligned, the target was placed in the front focal plane of l_4. The necessary computer simulations were then completed by modifying

the *Matlab* routine in Appendix C to account for the Ronchi ruling and the ideal phasemask shown in Figure 7.17 generated via the Gerchberg-Saxton algorithm.

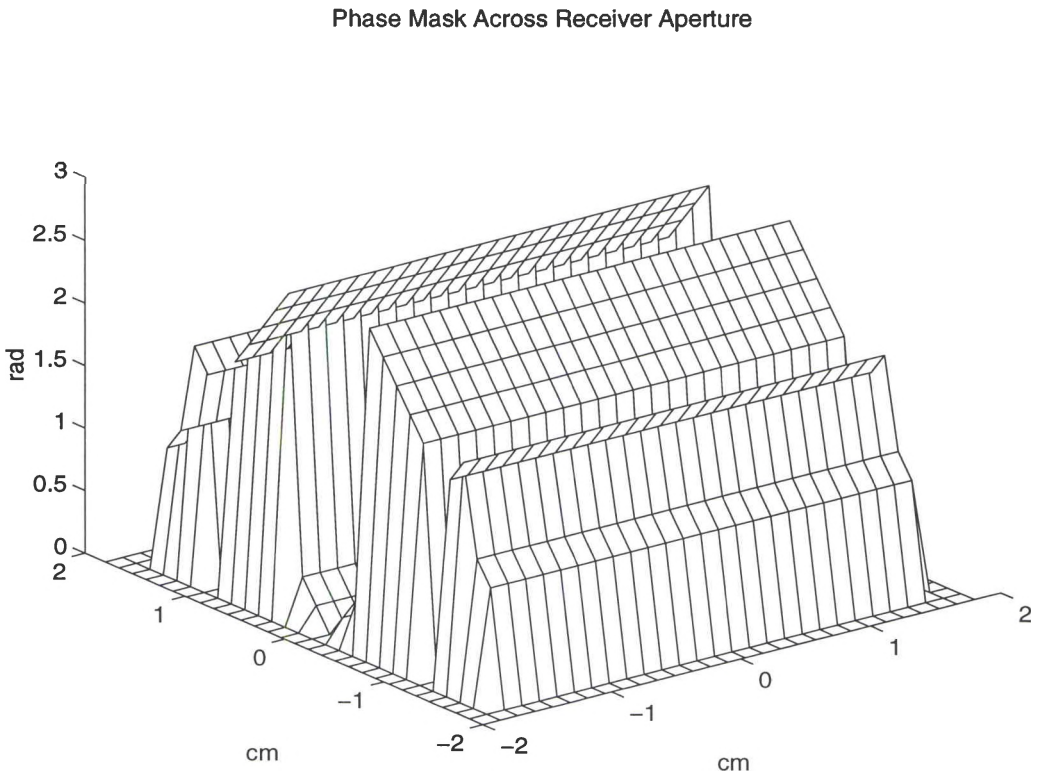

Figure 7.17: Phasemask for Ronchi ruling target.

Note, all system components such as the fiber receiver, the transform lenses, and operating wavelength in the experimental setup remained the same. Writing this phasemask across the LCSLM, the F/R coupling efficiency enhancement for the Ronchi ruling target was determined. Table 7.2 displays both the theoretical and experimental results for this target.

Table 7.2: Theoretical and experimental results for factor increase in coupling for the Ronchi ruling target.

Quantity	Theoretical Results, Ronchi Ruling	Experimental Results, Ronchi Ruling
Power coupled w/o phasemask	NA	59 ± 5 nW
Power coupled w/ phasemask	NA	183 ± 5 nW
Total power in fiber plane	NA	0.46 ± 0.01 mW
$\Delta\eta_{F/R}$	3.11x	3.10 ± 0.01x

Here we see that even though the ideal phasemask has become much more complicated, the experimental and theoretical results match each other very well and a significant factor increase in F/R coupling can be obtained.

Chapter VIII

Conclusions and Recommendations

Incorporating a SMOF detector into a real-world ladar system limits one's ability to couple a return signal. Previous models[2] have demonstrated that received power coupling efficiency for a purely diffuse target, based on system parameters, can be optimized by adjusting the truncation ratio at the transmitter and matching the NA of the coupling optics with the NA of the fiber receiver. However, this optimization technique assumed a resolved target generating a singlemode return and did not allow for variations in target size. In this thesis, we have developed a general model for predicting coupling efficiency in terms of general target illumination, target size, and system parameters.

Through numerical analysis, we have shown that received power coupling efficiency depends not only on optimizing transmitter and receiver optics, but on the size and range of the target as well. If the illuminated portion of a target falls within the receiver's diffraction limited spot size at the target plane, a larger amount of the collected return will be coupled into the fiber mode. Thus, singlemode returns will have a higher $\eta_{F/R}$ than multimode returns from targets at the same range. However, for a target of constant size, whether or not its return is singlemode or multimode depends on the target's range and the receiver's diameter. As the distance from the receiver increases,

the receiver's diffraction limited spot size in the target plane also increases. Therefore, at some distance from receiver, the spot size and target diameter will be identical. At any point beyond this range, the target will have a singlemode return and a higher received power coupling efficiency.

A model has also been developed to determine the transmitted power coupling efficiency in terms of general target illumination. Transmitted power coupling efficiency and the resulting signal-to-noise ratio has been shown to decrease with increasing target range. For singlemode returns, the signal-to-noise ratio was shown to be well above the noise levels even at significant target ranges. Unfortunately, if one expands the transmitted beam to illuminate a larger target, we have shown that $\eta_{F/T}$ will decrease rapidly with increasing range.

To offset these declining trends in $\eta_{F/T}$ and $\eta_{F/R}$ for unresolved targets with multimode returns, it is possible to insert a phase modulating device such as a liquid crystal spatial light modulator (LCSLM) into the path of the ladar receiver. This device allows one to compensate for the phase accumulated upon propagation from the target to the receiver and filter it from the collected return signal. By incorporating the Gerchberg-Saxton error reduction algorithm into a theoretical *Matlab* simulations of the general illumination ladar system, this target specific, phase profile can be found. Applying this modeling technique, the F/R coupling efficiencies for several uniformly illuminated/unresolved, rectangular glint targets [i.e. diffuse targets with zero random phase] were examined with and without the phasemask present in the system. Through theoretical simulations it was shown that factor increase in F/R coupling efficiency by applying an ideal phase filter across the receiver has no effect for targets with singlemode

returns. Yet for some larger targets generating multimode returns, the 1-D factor increase in coupling was found to be as high as 12x greater with the insertion of the phasemask.

The factor increase results were then verified experimentally for several different glint target sizes and found to agree well with their predicted values. Once establishing that it was possible to increase the F/R coupling efficiency into a SMOF ladar receiver by phase filtering the return, a Ronchi ruling target containing several higher spatial frequencies not present in the simple rectangular target was investigated. In spite of the fact that a noticeable change was seen in the ideal phasemask, both the theoretical and experimental F/R coupling efficiency was found to improve by a factor of 3.1x.

In this thesis, we have seen that almost no effect occurs for a 1-D phase filtering of singlemode target returns while the 1-D F/R coupling enhancement of multimode returns from very large targets appears to be greatly enhanced, almost 12x in some cases. However, one must remember that in the singlemode fiber receiver regime where we are working, both $\eta_{F/R}$ and $\eta_{F/T}$ are very small and thus a 2-D of 144x increase, although substantial, may never be realized. Several factors are seen to adversely affect the factor increase in coupling such as improperly aligning the phasemask within the system or changing the focal lengths of any of the transform lens. In addition to these effects, if the target is not centered within the illumination field, its image in the front focal plane of the first transform lens will move off axis and may never overlap with the back propagated fiber mode. Thus the system is not shift invariant. This type of alignment nightmare could easily be overcome by increasing the size of the fiber receiver to a larger multimode fiber and then amplifying the received signal with a multimode fiber amplifier to improve both $\eta_{F/R}$ and $\eta_{F/T}$ efficiencies.

Finally the effects of applying the same glint target phasemask to the returns from a diffuse target of identical proportions was investigated. Unlike for the glint case, F/R coupling efficiency improvement actually decreased with the application of the phasemask across the LCSLM. The phenomenon can be attributed to the fact that most of the energy in the return signal is scattered into the higher spatial frequencies by the individual diffuse scatters on the target's surface. As the target gets bigger, more and more energy fails to overlap with the back propagated fiber mode. Thus, this energy is unaffected by the application of the glint target phasemask. Therefore, if the coupling for this type of target is to be improved, another method for determining the ideal phasemask must be found.

Appendix A

F/R Coupling Efficiency for an Unresolved, Glint Target with a Multimode Return

A.1 Coupled Signal Power

First we recall the general expression given by Eq. (5-6) for the power scattered off of a glint target and coupled into an optical fiber receiver in a general illumination ladar system,

$$P_{sig,glint} \cong \frac{4BP_{Trans}\omega^2 T_g^2}{(\lambda f_3)^2(\lambda L)^2}\left|\iint d\bar{\rho}_t \exp\left[-B|\bar{\rho}_t|^2\right]\right.$$
$$\times \exp\left[-i\left(\frac{Bk\omega_o^2}{2f_2}+\frac{2\pi}{\lambda L}\right)|\bar{\rho}_t|^2\right]\mathrm{circ}\left(\frac{\bar{\rho}_t}{d_t}\right) \qquad , \quad \text{(A-1)}$$
$$\left.\times \iint d\bar{\rho}_R \,\mathrm{circ}\left(\frac{\bar{\rho}_R}{D_R}\right)\exp\left[\left(\left(\frac{\pi\omega}{\lambda f_3}\right)^2+\frac{i\pi}{\lambda L}\right)|\bar{\rho}_R|^2\right]\exp\left(\frac{i2\pi}{\lambda L}\bar{\rho}_R\cdot\bar{\rho}_t\right)\right|^2$$

where B has been defined as

$$B \equiv \frac{4\pi^2 f_2^2 \omega_o^2}{(\lambda L)^2\left(4f_2^2+\left(k\omega_o^2\right)^2\right)} \qquad . \quad \text{(A-2)}$$

From this branch point, one can derive an expression for the F/R coupling efficiency for the complicated case of an unresolved target with a multimode return. Applying Euler's

rule to each of the complex exponentials in Eq. (A-1) and scaling both the $d\bar{\rho}_R$ and $d\bar{\rho}_t$ variables of integration by D_R and D_t respectively, $P_{sig,glint}$ becomes

$$\begin{aligned} P_{sig,glint} \cong & \frac{4BP_{Trans}\omega^2 T_g^2 D_t^4 D_R^4}{(\lambda f_3)^2(\lambda L)^2}\left|\iint d\bar{\rho}_t \exp\left[-BD_t^2|\bar{\rho}_t|^2\right]\right. \\ & \times\cos\left[D_t^2\left(\frac{Bk\omega_o^2}{2f_2}+\frac{2\pi}{\lambda L}\right)|\bar{\rho}_t|^2\right]\mathrm{circ}(\bar{\rho}_t) \\ & \times\iint d\bar{\rho}_R\,\mathrm{circ}(\bar{\rho}_R)\exp\left[-\left(\frac{\pi\omega D_R}{\lambda f_3}\right)^2|\bar{\rho}_R|^2\right] \\ & \left.\times\cos\left(\frac{2D_R^2}{\lambda L}|\bar{\rho}_R|^2+\frac{2\pi D_R D_t}{\lambda L}\bar{\rho}_R\cdot\bar{\rho}_t\right)\right|^2 \end{aligned} \tag{A-3}$$

Expressing the both integrals in polar coordinates and using the circ functions to define the bounds over the receiver and target area, we obtain the following for the coupled signal power from a glint target,

$$\begin{aligned} P_{sig,glint} \cong & \frac{64BP_{Trans}\omega^2 T_g^2 D_t^4 D_R^4}{(\lambda f_3)^2(\lambda L)^2}\left|\int_0^{\frac{1}{2}} dr_t\int_0^{\frac{1}{2}} d\theta_t \exp\left[-BD_t^2 r_t^2\right]\cos\left[D_t^2\left(\frac{Bk\omega_o^2}{2f_2}+\frac{2\pi}{\lambda L}\right)r_t^2\right]\right. \\ & \times\int_0^{\frac{1}{2}} dr_R \exp\left[-\left(\frac{\pi\omega D_R}{\lambda f_3}\right)^2 r_R{}^2\right] \\ & \left.\times\int_0^{2\pi} d\theta_R \cos\left[\frac{2\pi D_R^2}{\lambda L}r_R{}^2+\frac{2\pi D_R D_t}{\lambda L}\left(r_R r_t\cos\theta_t\cos\theta_R+r_R r_t\sin\theta_t\sin\theta_R\right)\right]\right|^2 \end{aligned} \tag{A-4}$$

A slight rearrangement of terms then yields

$$\begin{aligned} P_{sig,glint} \cong & \frac{64BP_{Trans}\omega^2 T_g^2 D_t^4 D_R^4}{(\lambda f_3)^2(\lambda L)^2}\left|\int_0^{\frac{1}{2}} dr_t\, r_t \exp\left[-BD_t^2 r_t^2\right]\cos\left[D_t^2\left(\frac{Bk\omega_o^2}{2f_2}+\frac{2\pi}{\lambda L}\right)r_t^2\right]\right. \\ & \times\int_0^{\frac{1}{2}} dr_R\, r_R \exp\left[-\left(\frac{\pi\omega D_R}{\lambda f_3}\right)^2 r_R{}^2\right] \\ & \left.\times\int_0^{2\pi} d\theta_t\int_0^{2\pi} d\theta_R \cos\left[\frac{2\pi D_R^2 r_R{}^2}{\lambda L}\left(1+\frac{D_t r_t}{D_R r_R}\cos\left[\theta_t-\theta_R\right]\right)\right]\right|^2 \end{aligned} \tag{A-5}$$

Unfortunately, the nested integral relationship of Eq. (A-5) for the coupled signal power can not be simplified any further. Therefore, to calculate the F/R coupling efficiency this complicated expression must be divided by the total received power.

A.2 Total Received Power

Providing the assumption of $A_{Trans} << \lambda L$ is made, the field across the receiver plane (from Eq. (5-20)) is given by

$$\tilde{\mathbf{U}}_R(\bar{\rho}_R) = \frac{\exp(i2kL)}{(i\lambda f_3)(\lambda L)^2} \iint_{A_t} d\bar{\rho}_t \tilde{\mathbf{T}}(\bar{\rho}_t) \exp\left(\frac{ik}{2L}\left(|\bar{\rho}_t|^2 + |\bar{\rho}_R|^2 - 2\bar{\rho}_t \cdot \bar{\rho}_R\right)\right) \times \iint_{A_{Trans}} d\bar{\rho}\, \mathbf{U}_{Trans}(\bar{\rho}) \exp\left(\frac{ik}{2f_2}\right) \exp\left(\frac{ik}{2L}\left(|\bar{\rho}_t|^2 - 2\bar{\rho}\cdot\bar{\rho}_t\right)\right) \quad \text{(A-6)}$$

Thus total irradiance $I_{R,glint}$ at the receiver plane is simply the magnitude squared of $\tilde{\mathbf{U}}_R$. Given that the transmit beam is untruncated and that we are looking at an unresolved glint target [i.e. $\tilde{\mathbf{T}}(\bar{\rho}_t) = T_g$], this irradiance can be written as

$$I_{R,glint} = \frac{T_g}{(\lambda L)^4} \left| \iint_{A_t} d\bar{\rho}_t \exp\left(\frac{i2\pi}{\lambda L}|\bar{\rho}_t|^2\right) \exp\left(-\frac{i2\pi}{\lambda L}\bar{\rho}_R \cdot \bar{\rho}_t\right) \mathcal{U}_{Trans}\left(\frac{\bar{\rho}_t}{\lambda L}\right) \right|^2 , \quad \text{(A-7)}$$

where $\mathcal{U}_{Trans}$ is the Fourier transform of transmitted field in Eq. (3-15). Substituting the transform of transmitted field back into Eq. (5-20) and using Eq. (A-2), the irradiance at the receiver aperture can be written as

$$I_{R,glint} = \frac{2P_{Trans}BT_g^2}{\pi(\lambda L)^4} \left| \iint_{A_t} d\bar{\rho}_t \exp\left(\frac{i2\pi}{\lambda L}|\bar{\rho}_t|^2\right) \exp\left(-\frac{i2\pi}{\lambda L}\bar{\rho}_R \cdot \bar{\rho}_t\right) \times \exp\left(-B|\bar{\rho}_t|^2\right) \exp\left(\frac{iB\omega_o^2}{\lambda f_2}|\bar{\rho}_t|^2\right) \right|^2 \quad \text{(A-8)}$$

The limits of integration for the $d\bar{\rho}_t$ integral can be extended to infinity by defining a specific aperture function in the target plane $W_t(\bar{\rho})$. Then letting $W_t(\bar{\rho})$ be given by Eq. (3-21) and scaling the circ function to D_t, I_R becomes

$$I_{R,glint} = \frac{2P_{Trans}BT_g^2D_t^2}{\pi(\lambda L)^4}\left|\iint d\bar{\rho}_t \mathrm{circ}(\bar{\rho}_t)\exp\left(\frac{i2\pi D_t^2}{\lambda L}|\bar{\rho}_t|^2\right)\right.$$
$$\left.\times\exp\left(-\frac{i2\pi D_t}{\lambda L}\bar{\rho}_R\cdot\bar{\rho}_t\right)\exp\left(-BD_t^2|\bar{\rho}_t|^2\right)\exp\left(\frac{iB\omega_o^2D_t^2}{\lambda f_2}|\bar{\rho}_t|^2\right)\right|^2 . \quad \text{(A-9)}$$

Once the field at the receiver plane is known, the total power collected is simply the integral of this field over the area of the receiver. That is, after some manipulation

$$P_{R,glint} = \iint_{A_R} d\bar{\rho}_R I_{R,glint} = \iint d\bar{\rho}_R \mathrm{circ}\left(\frac{\bar{\rho}_R}{d_R}\right) I_{R,glint}$$

$$= \frac{2P_{Trans}BT_g^2D_t^2D_R^2}{\pi(\lambda L)^4}\iint d\bar{\rho}_R \mathrm{circ}(\bar{\rho}_R)\left|\iint d\bar{\rho}_t \mathrm{circ}(\bar{\rho}_t)\exp\left(\frac{i2\pi D_t^2}{\lambda L}|\bar{\rho}_t|^2\right)\right. \quad \text{(A-10)}$$
$$\left.\times\exp\left(-\frac{i2\pi D_tD_R}{\lambda L}\bar{\rho}_R\cdot\bar{\rho}_t\right)\exp\left(-BD_t^2|\bar{\rho}_t|^2\right)\exp\left(\frac{iB\omega_o^2D_t^2}{\lambda f_2}|\bar{\rho}_t|^2\right)\right|^2$$

Applying Euler's rule to the complex exponentials, expressing the both integrals in polar coordinates, and then using the circ functions to define the bounds over the receiver and target area yields

$$P_{R,glint} = \frac{2P_{Trans}BT_g^2D_t^2D_R^2}{\pi(\lambda L)^4}\int_0^{\frac{1}{2}} dr_R\, r_R \int_0^{2\pi} d\theta_R \left|\int_0^{\frac{1}{2}} dr_t\, r_t \cos\left[\left(\frac{2\pi D_t^2}{\lambda L}+\frac{B\omega_o^2D_t^2}{\lambda f_2}\right)r_t^2\right]\right.$$
$$\left.\times\exp\left(-BD_t^2r_t^2\right)\int_0^{2\pi} d\theta_t \cos\left(\frac{2\pi D_tD_R}{\lambda L}r_tr_R\cos\left[\theta_R-\theta_t\right]\right)\right|^2 . \quad \text{(A-11)}$$

Finally dividing Eq. (A-5) by Eq. (A-11), we attain the F/R coupling efficiency expression for an unresolved, glint target with a multimode return,

$$\eta_{F/R,glint} \cong \frac{8\omega^2 D_R^2}{(\lambda f_3)^2} \frac{\left| \int_0^{\frac{1}{2}} dr_t\, r_t \exp\left[-BD_t^2 r_t^2\right] \cos\left[D_t^2 \left(\frac{Bk\omega_o^2}{2f_2} + \frac{2\pi}{\lambda L} \right) r_t^2 \right] \right.}{\int_0^{\frac{1}{2}} dr_R\, r_R \int_0^{2\pi} d\theta_R \left| \int_0^{\frac{1}{2}} dr_t\, r_t \exp\left[-BD_t^2 r_t^2\right] \cos\left[\left(\frac{2\pi D_t^2}{\lambda L} + \frac{Bk\omega_o^2 D_t^2}{2f_2} \right) r_t^2 \right] \right.}$$

$$\left. \times \int_0^{\frac{1}{2}} dr_R\, r_R \exp\left[-\left(\frac{\pi\omega D_R}{\lambda f_3} \right)^2 r_R^{\,2} \right] \right.$$

$$\left. \times \int_0^{2\pi} d\theta_t \int_0^{2\pi} d\theta_R \cos\left[\frac{2\pi D_R^2 r_R^{\,2}}{\lambda L} \left(1 + \frac{D_t r_t}{D_R r_R} \cos\left[\theta_t - \theta_R\right] \right) \right] \right|^2$$

$$\left. \times \int_0^{2\pi} d\theta_t \cos\left[\frac{2\pi D_R D_t r_R r_t}{\lambda L} \cos\left[\theta_t - \theta_R\right] \right] \right|^2$$

Appendix B

F/R Coupling Efficiency for a Resolved, Diffuse Target with a Singlemode Return

B.1 Field at the Fiber

Recalling the paper originally written by Jacob *et. al.*,[2] we extract the following expression (Eq. 8) for the received field at the fiber endface

$$\begin{aligned}\tilde{\mathbf{U}}_f(\bar{\rho}_f) = \frac{1}{(i\lambda f)(\lambda L)^2}\exp\left(\frac{ik}{2f}|\bar{\rho}_f|^2\right)\iint d\bar{\rho}_R W_R(\bar{\rho}_R)\exp\left(-\frac{ik}{f}\bar{\rho}_f\cdot\bar{\rho}_R\right)\\ \times\iint_{A_t} d\bar{\rho}_t\tilde{\mathbf{T}}(\bar{\rho}_t)\exp\left(-\frac{ik}{2L}\left(|\bar{\rho}_t|^2+|\bar{\rho}_R|^2-2\bar{\rho}_t\cdot\bar{\rho}_R\right)\right)\\ \times\iint_{A_{Trans}} d\bar{\rho}\mathbf{U}_{Trans}(\bar{\rho})\exp\left(\frac{ik}{2L}\left(|\bar{\rho}|^2+|\bar{\rho}_t|^2-2\bar{\rho}\cdot\bar{\rho}_t\right)\right)\end{aligned}, \quad \text{(B-1)}$$

where as earlier a boldface quantity represents complex fields, an overscore denotes a vector quantity, and a tilde represents a random fields. Furthermore, A_{trans} and A_t represent the transmitter aperture area and the target area respectively. Upon examination of Eq. (B-1), several assumptions can be made. The quadratic phase term due to $\bar{\rho}_f$ is negligible since, the diameter of the fiber core is only a couple of microns while the focal length of the receiver optics is on the order of several centimeters. The phase term

resulting from $\bar{\rho}$ can also be ignored as well. In the far field, $A_{trans} << \lambda L$ and this quadratic term will be insignificant.

At this point, two of the original assumptions made by Jacob was found to be incorrect. Initially, the quadratic term arising from $\bar{\rho}_R$ was assumed to be insignificant. The previous analysis concluded that, in the far field, $A_R << \lambda L$. Unfortunately, this is not the case. If one evaluates this expression for a target range of 20 km, a transmitted wavelength of 1.064 mm, and a receiver diameter of 10 cm, this relationship does not hold. Therefore, this phase term can not be ignored and must included in the final analysis. Another inconsistency was also found in the reflected wavefront from the target. As the transmitted beam propagates toward the target, its wavefront diverges. This is apparent in positive exponential associated with the A_{Trans} integral in Eq. (B-1). Upon reflection from the target, the resulting wavefront will continue to diverge. However, the exponential within the A_t integral is negative, implying a converging wavefront. This error is easily corrected by making entire exponential positive.

Correcting these false assumptions and rearranging terms, Eq. (B-1) can be rewritten more compactly as

$$\begin{aligned}\tilde{\mathbf{U}}_f(\bar{\rho}_f) = \frac{1}{(i\lambda f)(\lambda L)^2}\iint_{A_t} d\bar{\rho}_t \tilde{\mathbf{T}}(\bar{\rho}_t)\exp\left(\frac{i2\pi}{\lambda L}|\bar{\rho}_t|^2\right) \\ \times \iint_{A_{Trans}} d\bar{\rho}\mathbf{U}_{Trans}(\bar{\rho})\exp\left(-\frac{i2\pi}{\lambda L}\bar{\rho}\cdot\bar{\rho}_t\right) \\ \times \iint d\bar{\rho}_R W_R(\bar{\rho}_R)\exp\left(\frac{i\pi}{\lambda L}|\bar{\rho}_R|^2\right)\exp\left(-i2\pi\bar{\rho}_R\cdot\left(\frac{\bar{\rho}_t}{\lambda L}+\frac{\bar{\rho}_f}{\lambda f}\right)\right)\end{aligned} \quad \text{(B-2)}$$

Now, if we assume that the truncation of the transmitted beam is insignificant, the limits of integration over the A_{Trans} integral can be extended out to infinity. Equation (B-2) is

now a series of Fourier transforms resulting in the following expression for the field at the focal plane of the receiver

$$\tilde{U}_f(\bar{\rho}_f) = \frac{1}{(i\lambda f_3)(\lambda L)^2}\iint_{A_t} d\bar{\rho}_t\, \tilde{T}(\bar{\rho}_t)\exp\left(\frac{i2\pi}{\lambda L}|\bar{\rho}_t|^2\right)\mathcal{U}_{Trans}\left(\frac{\bar{\rho}_t}{\lambda L}\right)$$
$$\times\iint d\bar{\rho}_R\, W_R(\bar{\rho}_R)\exp\left(\frac{i\pi}{\lambda L}|\bar{\rho}_R|^2\right)\exp\left(-i2\pi\bar{\rho}_R\cdot\left(\frac{\bar{\rho}_t}{\lambda L}+\frac{\bar{\rho}_f}{\lambda f}\right)\right) \quad . \quad \text{(B-3)}$$

where $\mathcal{U}_{trans}$ is the Fourier transform of the transmitted field and $\mathcal{W}_R$ is the Fourier transform of the generalized pupil function.

B.2 Coupling Efficiency

Using Eq. (B-3) above for the field at the fiber plane, the amount of power coupled into the fundamental mode of the fiber is merely the correlation between this field and the complex conjugate of the modal field, $\mathbf{U}_{01}^*(\bar{\rho}_f)$. This coupled, signal power can then be approximated via an overlap integral between the two fields,[9]

$$\bar{P}_{sig} \approx \left|\iint d\bar{\rho}_f \mathbf{U}_f(\bar{\rho}_f)\mathbf{U}_{01}^*(\bar{\rho}_f)\right|^2 \quad . \quad \text{(B-4)}$$

Substituting Eq. (B-3) into Eq. (B-4) and rearranging terms we obtain the following expression for signal power,

$$\tilde{P}_{sig} \approx \left|\frac{1}{(i\lambda f)(\lambda L)^2}\iint_{A_t} d\bar{\rho}_t\tilde{T}(\bar{\rho}_t)\exp\left(\frac{i2\pi}{\lambda L}|\bar{\rho}_t|^2\right)\mathcal{U}_{Trans}\left(\frac{\bar{\rho}_t}{\lambda L}\right)\right.$$
$$\left.\times\iint d\bar{\rho}_f\mathbf{U}_{01}^*(\bar{\rho}_f)W_R(\bar{\rho}_R)\exp\left(\frac{i2\pi}{\lambda L}|\bar{\rho}_R|^2\right)\exp\left[-i2\pi\bar{\rho}_R\left(\frac{\bar{\rho}_t}{\lambda L}+\frac{\bar{\rho}_f}{\lambda f}\right)\right]\right|^2 \quad . \quad \text{(B-5)}$$

Now, using the following statistical relationships given in Eq. (3-10) for a purely diffuse target, we see that after some rearrangement and manipulation, the expectation of the signal power coupled into the fundamental fiber mode can be expressed as

$$E\left[\tilde{P}_{sig}\right] \cong \frac{T_0}{f^2(\lambda L)^4}\iint_{A_t} d\bar{\rho}_t \left|\mathcal{U}_{Trans}\left(\frac{\bar{\rho}_t}{\lambda L}\right)\right|^2$$
$$\times \iint d\bar{\rho}_R \mathcal{U}_{01}^*\left(\frac{\bar{\rho}_R}{\lambda f}\right) W_R(\bar{\rho}_R) \exp\left(\frac{i\pi}{\lambda L}|\bar{\rho}_R|^2\right)\exp\left(\frac{i2\pi}{\lambda L}\bar{\rho}_R\cdot\bar{\rho}_t\right) \qquad \text{(B-6)}$$
$$\times \iint d\bar{\rho}_R' \mathcal{U}_{01}\left(\frac{\bar{\rho}_R'}{\lambda f}\right) W^*{}_R(\bar{\rho}_R') \exp\left(-\frac{i\pi}{\lambda L}|\bar{\rho}_R'|^2\right)\exp\left(-\frac{i2\pi}{\lambda L}\bar{\rho}_R'\cdot\bar{\rho}_t\right)$$

where $\mathcal{U}_{01}$ is the Fourier transform of the fiber mode and $\bar{\rho}_R$ and $\bar{\rho}_R'$ are arbitrary variables of integration in the receiver plane.

A change of variables is now order to simplify the integration. By defining the following variables

$$\bar{\rho}_o \equiv \frac{\bar{\rho}_R + \bar{\rho}_R'}{2} \text{ and } \Delta\bar{\rho} \equiv \bar{\rho}_R' - \bar{\rho}_R \quad \Rightarrow \iint d\bar{\rho}_R \iint d\bar{\rho}_R' = \iint d\bar{\rho}_0 \iint d\Delta\bar{\rho}\,, \qquad \text{(B-7)}$$

and making the appropriate substitution back into Eq. (B-6), we obtain

$$E\left[\tilde{P}_{sig}\right] \cong \frac{T_0}{f^2(\lambda L)^4}\iint d\Delta\bar{\rho}\left[\iint_{A_t} d\bar{\rho}_t \left|\mathcal{U}_{Trans}\left(\frac{\bar{\rho}_t}{\lambda L}\right)\right|^2 \exp\left(-\frac{i2\pi}{\lambda L}\bar{\rho}_t\cdot\Delta\bar{\rho}\right)\right]$$
$$\times \iint d\bar{\rho}_o \mathcal{U}_{01}^*\left(-\frac{\bar{\rho}_o}{\lambda f}+\frac{\Delta\bar{\rho}}{2\lambda f}\right)\mathcal{U}_{01}\left(-\frac{\bar{\rho}_o}{\lambda f}-\frac{\Delta\bar{\rho}}{2\lambda f}\right) \qquad \text{(B-8)}$$
$$\times W_R\left(\bar{\rho}_0 - \tfrac{1}{2}\Delta\bar{\rho}\right) W^*{}_R\left(\bar{\rho}_0 + \tfrac{1}{2}\Delta\bar{\rho}\right)\exp\left(-\frac{i2\pi}{\lambda L}\bar{\rho}_o\cdot\Delta\bar{\rho}\right)$$

Up until now, we have made no assumptions about the nature of the target. However, if we assume that the target area is much larger than the illuminating beam, the target is said to be resolved. Therefore, the limits of integration over A_t can be extended

out to infinity and the $d\bar{\rho}_t$ integral merely becomes the inverse Fourier transform of the transmitted field, $\mathcal{F}^{-1}\{\}$. This allows us to rewrite Eq. (B-8) as follows

$$
\begin{aligned}
E\left[\tilde{P}_{sig}\right] \cong \frac{T_0}{f^2(\lambda L)^4} \iint d\Delta\bar{\rho}\, \mathcal{F}^{-1}\left\{\left|\mathcal{U}_{Trans}\left(\frac{\bar{\rho}_t}{\lambda L}\right)\right|^2\right\}_{\frac{\Delta\bar{\rho}}{\lambda L}} \\
\times \iint d\bar{\rho}_o \mathcal{U}_{01}^*\left(-\frac{\bar{\rho}_o}{\lambda f}+\frac{\Delta\bar{\rho}}{2\lambda f}\right)\mathcal{U}_{01}\left(-\frac{\bar{\rho}_o}{\lambda f}-\frac{\Delta\bar{\rho}}{2\lambda f}\right), \\
\times W_R\left(\bar{\rho}_0-\tfrac{1}{2}\Delta\bar{\rho}\right)W^*{}_R\left(\bar{\rho}_0+\tfrac{1}{2}\Delta\bar{\rho}\right) \\
\times \exp\left(\frac{-i2\pi}{\lambda L}\bar{\rho}_0\cdot\Delta\bar{\rho}\right)
\end{aligned}
\qquad \text{(B-9)}
$$

thus obtaining an expression for expected signal power coupled into the fundamental mode of the fiber. Any further development of this equation requires a priori knowledge of the transmitted field, the aperture function, and the field in the fiber.

We can now define the transmitted field $\mathbf{U}_{Trans}(\bar{\rho})$, normalized to the transmitted power, as

$$
\mathbf{U}_{Trans}(\bar{\rho}) \equiv \sqrt{\frac{2P_{Trans}}{\pi\omega_o^2}}\exp\left(-\frac{|\bar{\rho}|^2}{\omega_o^2}\right), \qquad \text{(B-10)}
$$

and let our aperture function $W_R(\bar{\rho})$ be given by Eq. (3-21), and U_{01} be given by Eq. (2-7). Substituting these expressions into Eq. (B-9) and scaling all spatial variables, we obtain the following expression for $E\left[P_{sig}\right]$ after some rearrangement

$$E\left[\tilde{P}_{sig}\right] \cong \frac{4T_0 P_{Trans} D_R^2 a^2}{\pi L^2} \iint d\Delta\bar{\rho} \exp\left[-\left(\frac{1}{2}\left(\frac{D_R^2}{\omega_o^2}\right)+a^2\right)\left|\Delta\bar{\rho}\right|^2\right]$$
$$\times \iint d\bar{\rho}_o \mathrm{circ}(\bar{\rho}_0 - \tfrac{1}{2}\Delta\bar{\rho})\mathrm{circ}(\bar{\rho}_0 + \tfrac{1}{2}\Delta\bar{\rho}) \exp\left(-4a^2\left|\bar{\rho}_0\right|^2\right) \quad , \quad \text{(B-11)}$$
$$\times \exp\left(\frac{-i2\pi D_R}{\lambda L}\bar{\rho}_0 \cdot \Delta\bar{\rho}\right)$$

where a is a collection of constants associated with the receiver and defined as

$$a^2 \equiv \frac{1}{2}\left(\frac{\pi\omega D_R}{\lambda f}\right)^2 \quad , \quad \text{(B-12)}$$

and ω is given by Eq. (2-8). It is important to note that Eq. (3-23) of the general illumination model for a resolved, circular diffuse target reduces to the above expression simply by letting f_2 go to infinity in the N parameter.

Recalling that we have defined the two circ functions as unit diameter functions centered at $\pm\Delta\bar{\rho}/2$ in the $\bar{\rho}_o$ plane, the $d\bar{\rho}_o$ integral is merely the area of overlap between the two functions. Upon inspection on the Figure 3.2, if the separation between the two centers of the circ functions is greater the one [i.e., $|\Delta\bar{\rho}| > 1$], there will be no overlap between the two functions and the expected signal power will be zero. One also notices that the two circ functions are weighted by an extra exponential term in the second integral. If we employ Euler's relationship, this exponential can be expanded into a sine and cosine term. The $d\bar{\rho}_o$ integral now contains two even circ functions, an even cosine function, and an odd sine function. With the limits on the integral extended to infinity, the area resulting from the sine term will be equal to zero due to the odd nature of the function. Equation (B-11) then becomes

$$E\left[\tilde{P}_{sig}\right] \cong \frac{4T_0 P_{Trans} D_R^2 a^2}{\pi L^2} \iint d\Delta\bar{\rho} \exp\left[-\left(\frac{1}{2}R^2 + a^2\right)\left|\Delta\bar{\rho}\right|^2\right]$$
$$\times \iint d\bar{\rho}_o \mathrm{circ}(\bar{\rho}_0 - \tfrac{1}{2}\Delta\bar{\rho})\mathrm{circ}(\bar{\rho}_0 + \tfrac{1}{2}\Delta\bar{\rho}) \exp\left(-4a^2\left|\bar{\rho}_0\right|^2\right) \quad , \quad \text{(B-13)}$$
$$\times \cos\left(\frac{2\pi D_R{}^2}{\lambda L}\bar{\rho}_0 \cdot \Delta\bar{\rho}\right)$$

where the system truncation ratio $R = D_R/\omega_o$ has been introduced.

Now, recognizing that the exponential associated with the $d\Delta\bar{\rho}$ integral is a modulated, circularly symmetric Gaussian, the limits of integration can be replaced by the bounds of the overlap area between the two circ functions. Expressing the $d\Delta\bar{\rho}$ integral in polar coordinates and making the following vector substitutions,

$$\Delta\bar{\rho} \equiv r\cos\theta\hat{x} + r\sin\theta\hat{y} \quad \text{and} \quad \bar{\rho}_o \equiv x\hat{x} + y\hat{y} \quad , \quad \text{(B-14)}$$

the dot product yields

$$\bar{\rho}_o \cdot \Delta\bar{\rho} = rx\cos\theta + ry\sin\theta \quad . \quad \text{(B-15)}$$

However, with the modulated Gaussian being circularly symmetric, it is independent of the angle associated with $\Delta\bar{\rho}$. This makes it possible to choose a convenient direction of $\Delta\bar{\rho}$ in which to calculated the area of overlap. In this case we will consider a shift along the y axis, $\theta = 90°$. Expressing the $d\Delta\bar{\rho}$ integral in polar coordinates and making the above vector substitutions, integration of Eq. (B-13) yields

$$E\left[\tilde{P}_{sig}\right] \cong \frac{32T_0 P_{Trans} D_R^2 a^2}{\pi L^2} \int_0^1 dr \exp\left[-\left(\frac{1}{2}R^2 + a^2\right)r^2\right] r$$
$$\times \int_0^{\frac{1}{2}\sqrt{1-r^2}} dx \exp\left(-4a^2x^2\right) \quad . \quad \text{(B-16)}$$
$$\times \int_0^{\sqrt{\frac{1}{4}-x^2}-\frac{r}{2}} dy \exp\left(-4a^2y^2\right)\cos\left(\frac{2\pi D_R{}^2 ry}{\lambda L}\right)$$

Dividing the above expression by the expectation of the total power received $E[\tilde{P}]$, the coupling efficiency can be determined. If the average power is then given by,

$$E[\tilde{P}] \cong \frac{T_0 P_{Trans} A_R}{L^2} = \frac{T_0 P_{Trans} \pi D_R^2}{4L^2} \quad , \tag{B-17}$$

the F/R coupling efficiency for a resolved, diffuse target with a single mode returns becomes

$$\begin{aligned} \eta_{F/R,diffuse} = \frac{E[\tilde{P}_{sig}]}{E[\tilde{P}]} \cong \frac{128a^2}{\pi} \int_0^1 dr \exp\left[-\left(\frac{1}{2}R^2 + a^2\right)r^2\right] r \\ \times \int_0^{\frac{1}{2}\sqrt{1-r^2}} dx \exp\left(-4a^2x^2\right) \\ \times \int_0^{\sqrt{\frac{1}{4}-x^2}-\frac{r}{2}} dy \exp\left(-4a^2y^2\right) \cos\left(\frac{2\pi D_R{}^2 ry}{\lambda L}\right) \end{aligned} \tag{B-18}$$

This equation can be directly compared to Eq. (31) developed by Jacob[2] by rewriting the Erf function in integral from, changing the variables of integration to x,y coordinates, and letting $u = r^2$, we obtain

$$\begin{aligned} \eta_c = \frac{E[\tilde{P}_{sig}]}{E[\tilde{P}]} \cong \frac{128a^2}{\pi} \int_0^1 dr \exp\left[-\left(\frac{1}{2}R^2 + a^2\right)r^2\right] r \\ \times \int_0^{\frac{1}{2}\sqrt{1-r^2}} dx \exp\left(-4a^2x^2\right) \int_0^{\sqrt{\frac{1}{4}-x^2}-\frac{r}{2}} dy \exp\left(-4a^2y^2\right) \end{aligned} \tag{B-19}$$

Although both presentations of $\eta_{F/R,diffuse}$ contain mostly the same components, the dy integral itself in Eq. (B-18) has an extra cosine modulation not present in Jacob's original analysis. The effect of this added term can be seen in Figure B.1 where both the corrected model of Eq. (B-18) and Jacob's original model of Eq. (B-19) are displayed vs. the "a" parameter.

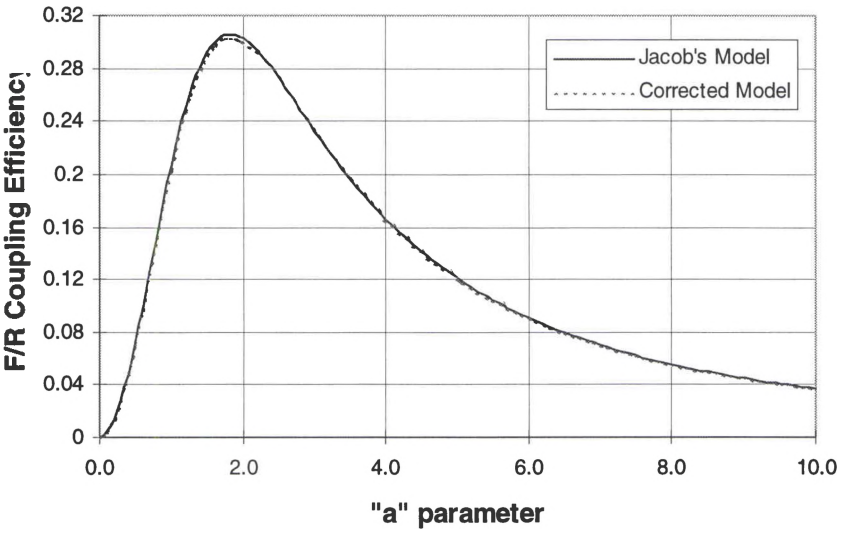

Figure B.1: F/R coupling efficiency vs. the "a" parameter for a resolved, circular target at 20 km with singlemode return. This figure displays the comparison between the earlier analysis developed by Jacob[2] and the general illumination model of Chapter III.

As we can see, even with the corrective cosine term, the only noticeable difference between the two developments is near the peak of the curve. Here the corrective term lowers the overall F/R coupling efficiency by 0.5%

Appendix C

Matlab Computer Simulations

C.1 Field Scaling

In this section we will examine the methodology involved in determining the specific scaling constants for both glint and diffuse targets associated with the computer simulations in Chapter VI. When simulating the fields at various points throughout the path of the general illumination ladar system, care must be taken to ensure that each field is sampled at the Nyquist rate so that aliasing is avoided. Generally this minimum sampling rate is twice the highest spatial frequency contained within the field profile. Once this sampling rate is determined in the spatial domain say for the modal field of the fiber, the total number of N_s samples or pixels can be easily calculated. The number of pixels then becomes the new width of the fiber mode and this field to be programmed into the simulation routine. Yet, fixing sampling ratio in one plane means that all other sampling rates, scaled appropriately in accordance with the Fourier transform of the reference field, must be the same throughout the system. This way, the transformed target field and the back propagated fiber field in the receiver plane correspond to the same dimensions.

For the remainder of this simulation, we will assume the sampling of the LP_{01} modal field of the fiber as our reference sampling rate and scale everything else accordingly. Thus a pixel spacing in the fiber plane of Δx_1 (m/pix) corresponds to a pixel spacing in the receiver plane Δx_2 (m/pix) of

$$\Delta x_2 = \frac{\lambda f_3}{\Delta x_1 K} \qquad \text{(C-1)}$$

and a pixel spacing in the target plane Δx_3 (m/pix) of

$$\Delta x_3 = \frac{\Delta x_1 L}{f_3} \qquad \text{(C-2)}$$

where K is the total number of pixels in the array, L is the range to the target, f_3 is the focal length of the coupling optics, and λ is the operating wavelength. With these ratios set, the widths and scaling constants for every field associated with the diffuse and glint targets can be converted to pixels and included within the simulation.

C.2 *Matlab* Simulation Routines

The remainder of Appendix C outlines the actual steps involved for calculating the F/R coupling efficiency with and without the Gerchberg-Saxton phasemask across the LCSLM. Specifically the *Matlab* routines are given for the glint/diffuse targets in Chapter VI and the slit target of Chapter VII.

1. Glint Target

```
fibermode=zeros(512,512);
rxaperture=zeros(512,512);
IllumBeam=zeros(512,512);
target=zeros(512,512);
fresnel=zeros(512,512);
im=sqrt(-1);
```

```
%******* Define the Various Fields *************

%--------------------------------------
% *** Aperture Width Calc. ***
%--------------------------------------

wf=4.77*10^(-6);                                    %(actual width of fiber)
focal=.384;                                         %(focal length of coupling optics)
Lambda=1.064*10^(-6);
L=20000;                                            %(range to target)

samp=27;                                            %( # of samples across the fiber)
sampfiber=wf/samp;                                  %(Δx1)
dap=Lambda*focal/(sampfiber*512);                   %(Δx2)
dap2=.1/dap;                                        %(width of aperture in pixels)

for i=256-dap2/2:256+dap2/2;
   for j=256-dap2/2:256+dap2/2;
     R=sqrt((i-256)^2+(j-256)^2);
     if (R<=dap2/2);
        rxaperture(i,j)=1;                          %(aperture function)
     end
   end
end

c1a=sum(sum(rxaperture));
rxaperture = rxaperture /c1a;                       %(aperture function normalized to unit power)

tmp(1:256,1:256) = rxaperture(1:256,1:256);
rxaperture(1:256,1:256) = rxaperture(257:512,257:512);
rxaperture(257:512,257:512) = tmp(1:256,1:256);

tmp(1:256,257:512) = rxaperture(1:256,257:512);
rxaperture(1:256,257:512) = rxaperture(257:512,1:256);
rxaperture(257:512,1:256) = tmp(1:256,257:512);


%--------------------------------------
% *** normalized fiber field ***
%--------------------------------------

for i=256-(samp):256+(samp);
   for j=256-(samp):256+(samp);
      fibermode(i,j)=exp(-((i-256)^2+(j-256)^2)/samp^2);   %(fiber mode)
   end
end

In=(abs(fibermode))^2;
In=sum(sum(In));

c1=sqrt(In);
fibermode = fibermode /c1;                          %(fiber mode normalized to unit power)


tmp(1:256,1:256) = fibermode(1:256,1:256);
```

```
fibermode(1:256,1:256) = fibermode(257:512,257:512);
fibermode(257:512,257:512) = tmp(1:256,1:256);

tmp(1:256,257:512) = fibermode(1:256,257:512);
fibermode(1:256,257:512) = fibermode(257:512,1:256);
fibermode(257:512,1:256) = tmp(1:256,257:512);

magfibermode =abs(fibermode);

%----------------------------------
% *** Illumination Beam ***
%----------------------------------

wo=.025;                                          %(actual width of transmitted beam)
sampobj=sampfiber*L/focal;                        %(Δx3)
wos=L*Lambda/(sampobj*wo*pi);
wos1=-2*im*pi*sampobj^2/(L*Lambda)+1/(wos)^2;

for i=256-(wos):256+(wos);
   for j=256-(wos):256+(wos);
      IllumBeam(i,j)=exp(-((i-256)^2+(j-256)^2)*wos1);
   end
end

Inobj=(abs(IllumBeam))^2;
Inobj=sum(sum(Inobj));

c2=sqrt(Inobj);
IllumBeam = IllumBeam /c2;                %(normalized transmitted beam in target plane)


%-----------------------------------------------------
% *** Multiply by the Target Reflectivity ***
%-----------------------------------------------------

r=.5/sampobj;                                     %(target radius in pixels)
for i=256-r:256+r;
   for j=256-r:256+r;
     R=sqrt((i-256)^2+(j-256)^2);
     if (R<=r);
        target(i,j)=1;
     end
   end
end

IllBtar= IllumBeam .* target;

tmp(1:256,1:256) = IllBtar(1:256,1:256);
IllBtar(1:256,1:256) = IllBtar(257:512,257:512);
IllBtar(257:512,257:512) = tmp(1:256,1:256);

tmp(1:256,257:512) = IllBtar(1:256,257:512);
IllBtar(1:256,257:512) = IllBtar(257:512,1:256);
IllBtar(257:512,1:256) = tmp(1:256,257:512);
```

```
% ******* Start Gerchberg-Saxton Algorithm*******

%-------------------------------------
% *** Transform of Object ***
%-------------------------------------

FTIllBtar = fft2(IllBtar);

%-----------------------------------------------------
% *** Field Passed Through the Aperture ***
%-----------------------------------------------------

for i=256-(dap2):256+(dap2);
   for j=256-(dap2):256+(dap2);
      fresnel(i,j)=exp(2*im*pi*dap^2/(Lambda*L)*((i-256)^2+(j-256)^2));
   end
end

obj = atan2(imag(FTIllBtar),real(FTIllBtar));
Fp = rxaperture .* (abs(FTIllBtar) .* exp(im*obj)) .* fresnel;

%-------------------------------------------
% *** Begin error reduction loop ***
%-------------------------------------------

gs_iterations=1;

for i=1:gs_iterations;
   f = ifft2(Fp);

   spacephase = atan2(imag(f),real(f));
   fprime = magfibermode .* exp(im*spacephase);
   Fprime = fft2(fprime);
   freqphase = atan2(imag(Fprime),real(Fprime));

   Fp = abs(Fp) .* exp(im*freqphase);
end

%-------------------------------------------
% *** Phase Mask Across Aperture ***
%-------------------------------------------

phasemask = (freqphase - obj);
a2=fftshift(phasemask .* rxaperture);


%*****Calculate Coupling Eff. W/ and WO/phasemask*********

%-----------------------------------------------------------------
% *** Field Passed Through the Aperture w/Phasemask***
%-----------------------------------------------------------------

FTfibermode = fft2(fibermode);
phase_FTfibermode  = atan2(imag(FTfibermode),real(FTfibermode));
```

```
fiber_aperture1 = rxaperture .* (abs(FTfibermode) .* exp(im* phase_FTfibermode));
fiber_aperture2 = rxaperture .* (abs(FTfibermode) .* exp(im*(phasemask+ phase_FTfibermode)));



%-----------------------------------------
% *** Inverse Trans. of Ap. Field ***
%-----------------------------------------

fiber_target1 = ifft2(fiber_aperture1);
fiber_target2 = ifft2(fiber_aperture2);

%-------------------------------------
% *** Coupling Efficiency ***
%-------------------------------------

c4=pi^3*(abs(wos1)*512)^2/(2*(Lambda*focal)^2);                    %(glint scaling constant)

Psig1=sum(sum(fiber_target1 .* IllBtar));
Psig2=sum(sum(fiber_target2 .* IllBtar));
FTtarfield=(abs(sum(sum(FTIllBtar))))^2;
coupeff1=c4*(abs(Psig 1))^2/(sum(sum(rxaperture .* FTtarfield)))    %(coup. eff. wo/phasemask)
coupeff2=c4*(abs(Psig 2))^2/(sum(sum(rxaperture .* FTtarfield)))    %(coup. eff. wo/phasemask)
```

2. Singlemode, Diffuse Target

The heart of this code is identical to the above code for the glint target. Therefore only the alterations for the section titled ***Coupling Efficiency*** will be shown here.

```
%-------------------------------------------------
% *** Put a Random Phase on Object ***
%-------------------------------------------------

c_diff=(4*wos*512)^2/(2*(pi^2*dap2*Lambda*focal)^2);                %(diffuse coup. eff. constant)


n=1024;                                                            %(# of random phase iterations)
for i=1:n
   objphase = rand(512,512)*2*pi;
   o = IllBtar .* exp(im*objphase);
   Psig1= sum(sum(fiber_target1 .*o));
   Psig2= sum(sum(fiber_target2 .* o));

   FTtarfield=(abs(sum(sum(FTIllBtar))))^2;
   coupeff1(1,i)=c_diff*(abs(Psig1))^2/(sum(sum(rxaperture .* FTtarfield)));
   coupeff2(1,i)=c_diff*(abs(Psig2))^2/(sum(sum(rxaperture .* FTtarfield)));
end
```

```
%-----------------------------------------------
% *** Diffuse Coupling Efficiency ***
%-----------------------------------------------

for i=1:n;
   coupeff_ave1(1,i)=(sum(coupeff1(1,1:i)))/i;
   coupeff_ave2(1,i)=(sum(coupeff2(1,1:i)))/i;
end


coupeff_ave1(1,n)                    %(coup. eff. wo/phasemask)
coupeff_ave2(1,n)                    %(coup. eff. wo/phasemask)
```

3. Slit Target

Again, only the alterations to the original glint target code will be shown.

```
%---------------------------------------
% *** Aperture Width Calc. ***
%---------------------------------------

wf=4.77*10^(-6);
focalback=.75;                       %(focal length of front transform lens)
focalfront=.75;                      %(focal length of back transform lens)

samp=5;
sampfiber=wf/samp;
dap=Lambda*focalback/(sampfiber*512);
dap2=.04/dap;

%-------------------------------------------------------
% *** Multiply by the Target Reflectivity ***
%-------------------------------------------------------

xslt=200*10^(-6);                    %(actual x width of the slit)
sampobj=sampfiber*focalfront/focalback;   %(Δx3)
rx=xslt/sampobj;                     %(x dimension of slit in pixels)
yslt=.003;                           %(actual y width of the slit)
yscale=yslt*4/xslt;                  %(y dimension slit scale)
ry=yslt/(sampobj*yscale);            %(y dimension of slit in pixels)

for i=257-(rx/2):257+(rx/2);
   for j=257-(ry/2):257+(ry/2);
      target(i,j)=1;
   end
end

%-----------------------------------
% *** Transform of Object ***
%-----------------------------------
```

```
FTIllBtar= fft2(target);

%-----------------------------------------------------
% *** Field Passed Through the Aperture ***
%-----------------------------------------------------

obj = atan2(imag(FTIllBtar),real(FTIllBtar));
Fp = rxaperture .* (abs(FTIllBtar) .* exp(im*obj));

%-------------------------------------------------------------
% *** Coupling Efficiency and Factor Increase ***
%-------------------------------------------------------------

c_slt = (512^2)/(yscale*rx*ry*(Lambda*focalback)^2);                    %(slit scaling factor)


Psig1=sum(sum(fiber_target1 .* target));
Psig2=sum(sum(fiber_target2 .* target));
FTtarfield=(abs(sum(sum(FTIllBtar))))^2;
coupeff1=100*c_slt*(*(abs(Psig 1))^2/(sum(sum(rxaperture .* FTtarfield)))    %(coup. eff. wo/phasemask)
coupeff2=100*c_slt*(*(abs(Psig 2))^2/(sum(sum(rxaperture .* FTtarfield)))    %(coup. eff. wo/phasemask)

delta_coupeff3 = coupeff2/coupeff1                                     %(factor increase in coupling)
```

References

1. M. S. Salisbury, "Sensitivity improvement of a 1 μm ladar system incorporating an optical fiber preamplifier," *Opt. Eng.* **32** 2671-2680 (1993).

2. D. K. Jacob, M. B. Martin, B. D. Duncan, "Heterodyne ladar system efficiency enhancement using single-mode optical fiber mixers," *Opt. Eng.* **34** (11) 3122-3129 (Nov. 1995).

3. 1996 SPIE Aerospace Conference, Ladar High Resolution Seminar.

4. W. H. Lee, "Method for converting a Gaussian beam into a uniform beam," *Opt. Comm.* **36** (6) 469-471 (Mar. 15, 1981).

5. A. W. Synder, "Excitation and scattering of modes on a dielectric of optical fiber," *IEEE Trans. Microwave Theory and Techniques* **MTT-17** (17), 1138-1144 (Dec. 1969).

6. J.C. Dainty, *Topics in Applied Physics, Laser Speckle and Related Phenomena*, Springer-Verlag, New York, (1984).

7. F.G. Stemler, *Introduction to Communication Systems, Third Edition*, Addison-Wesley, New York, (1990).

8. D. Marcuse, "Loss analysis of singlemode fiber splices," *Bell System Tech. J.* **56** (5), 703-718 (May-June 1977).

9. L. B. Jeunhomme, *Single-Mode Fiber Optics*, Marcel Dekker, Inc., New York, (1990).

10. J. A. Buck, *Fundamentals of Optical Fibers*, Wiley and Sons, New York, (1995).

11. F. L. Pedrotti, S.J.; L. S. Pedrotti, *Introduction to Optics, Second Edition* Prentice Hall, Englewood Cliffs, New Jersey (1993).

12. J. W. Goodman, *Introduction to Fourier Optics, Second Edition*, McGraw-Hill, New York, (1996).

13. J. H. Shapiro, "Target reflectivity theory for coherent laser radar," *App. Opt.* **12** (15), (Sept. 1982).

14. E. W. Swokowski, *Calculus With Analytic Geometry, Fourth Edition*, PWS-Kent, Boston, (1988).

15. M. J. Missy, "Analysis of and applications for a liquid crystal optical phased array," M. S. Thesis, University of Dayton, Dayton, OH, (1996).

16. J. A. Overbeck, M. S. Salisbury, M. M. Mark, E. A. Watson, "Required energy for a laser radar system incorporating a fiber amplifier or an avalanche photodiode," *App. Opt.* **34** (33) (Nov. 20 1995).

17. D. Gloge, "Weakly guiding fibers," *Appl. Opt.* **10**, 2252-2258, (1971).

18. J. R. Fienup, "Phase retrieval algorithms: a comparison," *App. Opt.* **21** (15), (Aug. 1982).

19. R. W. Gerchberg, W. O. Saxton, "A practical algorithm for the determination of phase from image and diffraction plane pictures," *Optik* **35,** 237-246, (1972).

20. C. W. Therrien, *Discrete Random Signals and Statistical Signal Processing*, Prentice Hall, New Jersey (1992).

21. A. V. Oppenheim, R. W. Schafer, *Discrete-Time Signal Processing*, Prentice Hall, New Jersey, (1989).

22. J. D. Gaskill, *Linear Systems, Fourier Transforms, and Optics*, Wiley and Sons, New York, (1978).

23. J. R. Taylor, *An Introduction to Error Analysis*, University Science Books, Mill Valley, Ca, (1982).